Aix-Marseille Université
Laboratoire d'Astrophysique de Marseille

Galaxy stellar mass assembly using photometric redshifts in the 2 deg^2 COSMOS field

Olivier ILBERT

Habilitation à diriger des recherches

Soutenue le 26 Janvier 2016
Devant le Jury composé de

V. Buat	Présidente
D. Elbaz	Rapporteur
G. Mamon	Rapporteur
R. Pelló	Rapporteur
J. Devriendt	Examinateur
O. Le Fèvre	Tuteur

Contents

Page

Contents **i**

1 Introduction **1**
1.1 Cosmological framework . . . 2
1.2 Overview of the current paradigm for the galaxy formation and evolution . 3
1.3 An observational and statistical approach . . . 7
1.4 Plan of this manuscript . . . 8

2 Photometric redshifts **11**
2.1 Introduction . . . 11
2.2 Template-fitting method of the code Le Phare . . . 16
2.2.1 The standard template-fitting method . . . 17
2.2.2 Sensitivity of the photo-z to the photometric absolute calibration . 18
2.2.3 The set of templates . . . 19
2.2.4 Dust extinction . . . 22
2.2.5 Emission lines . . . 25
2.2.6 Bayesian approach . . . 27
2.2.7 Convergence toward a unified template-fitting method ? . . . 28
2.3 The COSMOS Photometric redshifts . . . 30
2.3.1 The COSMOS coverage . . . 30
2.3.2 Two multi-color catalogues . . . 31
2.3.3 Photometric redshifts for galaxies . . . 32
2.3.4 Photometric redshifts for AGN . . . 40

3 Global star formation history **43**
3.1 Measuring the galaxy properties . . . 44
3.1.1 Stellar masses . . . 44
3.1.2 Star formation rate . . . 47
3.2 Star formation history from instantaneous tracers . . . 48
3.3 Star formation history derived from the stellar mass census . . . 52
3.3.1 Stellar mass density at $0.2 < z < 4$ from UltraVISTA in DR1 . . . 54
3.3.2 Infer the SFH from the stellar mass density . . . 55
3.4 Summary . . . 56

4 Evolution of the specific star formation rate at $0.2 < z < 4$ 59
4.1 Link with the cosmological accretion rate . . . 61
4.2 *s*SFR functions at $z < 1.4$ . . . 62
4.2.1 $\mathcal{M}_\star$ – *s*SFR scatter plot and selection effects . . . 62
4.2.2 *s*SFR functions . . . 64
4.2.3 Evolution of the *s*SFR at $0.2 < z < 1.4$ . . . 65
4.3 An indirect method to estimate the *s*SFR at $1.5 < z < 4$ . . . 67
4.3.1 Description of the method . . . 67
4.3.2 Pros and cons of the method . . . 67
4.3.3 The *s*SFR derived from the UltraVISTA Mass Functions . . . 68
4.4 Evolution of the *s*SFR . . . 68
4.5 Summary . . . 70

5 Quenching 73
5.1 Separate star-forming and quiescent galaxies . . . 74
5.2 Physical processes involved in quenching . . . 76
5.2.1 The AGN bright-mode feedback and the link with gas-rich mergers 76
5.2.2 The hot-halo mode and radio AGN feedback . . . 77
5.2.3 Mixing merger and hot-halo mode . . . 78
5.2.4 Quenching along the galaxy secular evolution . . . 78
5.2.5 Environmental effects . . . 79
5.3 Observational constraint from the evolution of the GSMF . . . 79
5.3.1 The evolution of the quiescent and star-forming galaxies . . . 81
5.3.2 Mass quenching and environment quenching . . . 82
5.3.3 Comparison with galaxy formation models . . . 87
5.4 Link with the morphology . . . 87
5.5 Summary . . . 92

6 Conclusions and perspectives 95
6.1 Building of the stellar populations across cosmic time . . . 95
6.2 Characterize the processes responsible for the quenching . . . 97
6.3 Photometric redshifts for precision cosmology . . . 99
6.3.1 Photometric redshifts for weak lensing tomography . . . 100
6.3.2 Future wide field imaging surveys . . . 101

Bibliography 105

Chapter 1

Introduction

Galaxies are among the biggest entities in our Universe. Their existence was demonstrated only one hundred years ago (Slipher 1913, Curtis 1917, Hubble 1929) while speculated by Thomas Wright in 1750. In 1920, Shapley and Curtis debated on the scale of the Universe, the former defending the idea that our Universe was limited to the Milky Way and that all nebulae were small objects inside our galaxy. One argument of Shapley was the incredible scale that the Universe would have if these nebulae were outside our Milky Way. In one hundred years, the study of the galaxies has make tremendous progresses. Indeed, the scales in our Universe are beyond our imagination: the light that we receive from some galaxies has traveled billions of years and we can detect the light emitted by galaxies when the Universe was less than one billion years old (7% of its current age). We can admire millions of distant galaxies dragged away by an expanding Universe and most of them are composed of billions of stars.

At a distance considered as our neighborhood by cosmologists, detailed information of a million of galaxies has now been gathered. In the last ten years, the Sloan Digital Sky Survey has completely blown out our knowledge of the galaxy spatial distribution in this local Universe by establishing a three dimensional map with a million of galaxies. The cosmic web is now incredibly well traced, showing long filaments linking galaxy clusters, and large void areas. And the galaxy properties of a significant fraction of them is studied in great detail: their morphology, their emissivity from the X-ray to the radio, their dust properties or their kinematic are well characterized.

One of the main objective of cosmology is to understand how this complex Universe has emerged along cosmic time. How such systems including hundred billions of stars could have ever formed? How did they acquire their morphology? What are the dominant processes explaining the differentiation of the galaxy properties along cosmic time? In this manuscript, we tackle these fundamental questions from an observational point-of-view.

1.1 Cosmological framework

The galaxies grow into an evolving Universe and they represent only a tiny component of this Universe. The galaxy evolution can not be studied without considering the cosmological framework. A "concordance model" has emerged in the last decade to describe the geometry of our Universe and its evolution. This model assumes the existence of cold dark matter and dark energy and that the general relativity is holding over large scales. In this cosmology, called ΛCDM, only $5 \pm 0.01\%$ of the Universe is composed of baryonic matter, $25.9 \pm 0.1\%$ of the Universe is composed of an unknown Cold Dark Matter (CDM), dark energy represents 69% of the mass-energy of the Universe (Planck collaboration, 2015). The existence of dark matter is put in evidence indirectly by the observations of lensing effects, galaxy rotation curves and velocity dispersions in massive clusters. The nature of this dark matter is unknown. The term "Cold Dark Matter" refers to massive non-interacting particles. This kind of particles is favored by the growth rate of the galaxy large-scale structures along cosmic time (e.g. Springel et al. 2006). The discovery that the expansion of the Universe is accelerating, obtained by measuring the supernovae standard candles (Riess et al. 1998, Perlmutter et al. 1999) leads the community to introduce the "dark energy". Such an unknown "dark energy" is supposed to produce a negative pressure explaining this accelerating expansion. Numerous projects aim to study the nature of the dark energy. The observations of the cosmic microwave background (CMB) by several generations of satellites (COBE, WMAP, Planck) bring crucial information on the composition of the Universe. The CMB is a relic of the radiations in the Universe at the time of decoupling between matter and radiation. Its observation shows that the matter was quasi uniformly distributed 380,000 years after the big bang. Still, small density fluctuations are detected at the level of 10^{-5} in the CMB maps.

But why the cosmological framework has any importance to study galaxy evolution ? In our current paradigm, the contrast of the primordial matter fluctuations detected in the CMB maps increases with time under the action of gravity. Above a given contrast, these fluctuations collapse into dark-matter (DM) halos. The baryonic matter within these halos can form stars and galaxies. Therefore, galaxies evolve into DM halos which can merge with other halos along cosmic time. This hierarchical build-up of the DM structures explains well the presence of clusters, voids and filaments into the Universe. This hierarchical build-up has also a direct impact on the galaxy properties. For instance, galaxies can merge together or become satellite galaxies into a massive halo. The amount of cold gas available to form new stars is also directly regulated by the growth rate of DM structures. Therefore, the galaxy growth is directly regulated by the growth of DM structure, which is driven itself by the content of the Universe. While the current paradigm of the hierarchical build-up of the structures in a ΛCDM cosmological framework seems now to be solidly established, some alternative models exist. For instance, a "warm matter" component is considered by various groups (e.g. Dayal et al. 2015), and possible deviation of the general relativity over large scales is studied (e.g. De La Torre et al. 2013). Given the unknown nature of the dark matter

and dark energy, we need to keep in mind that any theory of galaxy formation relies on a cosmological background which could be modified in the next decades.

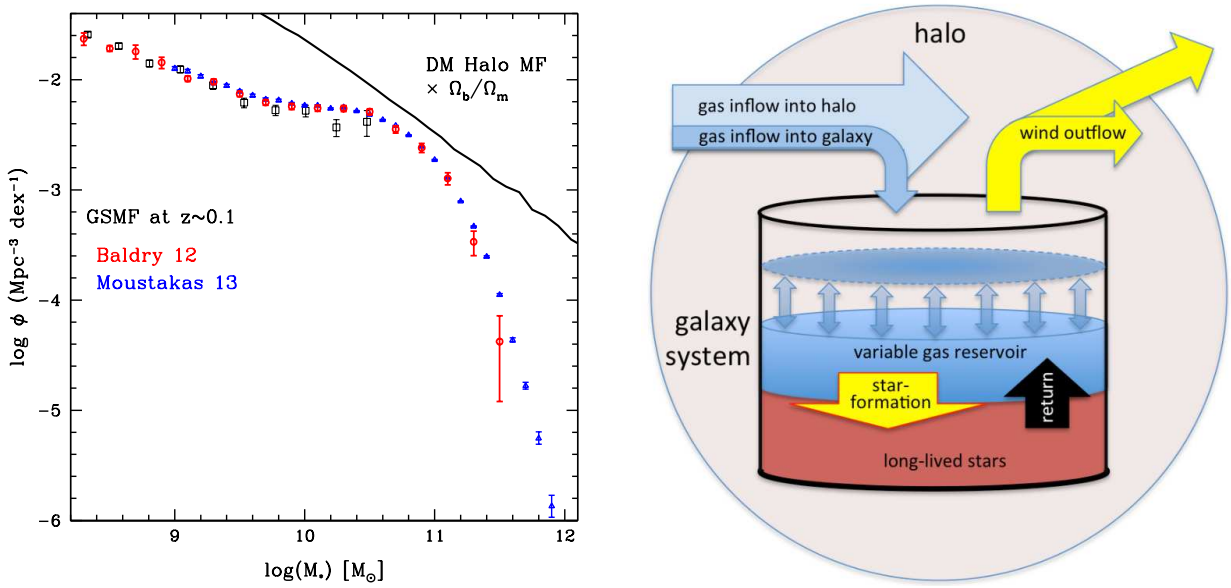

Figure 1.1: Left: comparison of the local DM halo mass function and the GSMF showing that the star formation needs to be completely suppressed in the most massive halos and reduced in low mass halos. AGN and SN feedbacks are possible candidates. Right: simplified galaxy+halo system as seen by Lilly et al. (2013) showing the gas inflow coming from the hierarchical growth of the DM halo, the gas which is converted into old stars by star formation processes, and gas outflows created by SN or AGN.

1.2 Overview of the current paradigm for the galaxy formation and evolution

Our main motivation in this manuscript is to understand how primordial galaxies with few thousands of stars evolve into huge massive systems with hundred billions of stars. In particular, we study the galaxy growth and the building of their stellar populations over time. In this section, we list the main mechanisms identified up to now. We summarize the current global picture established by the constant interplay between theory and observations, assuming that the cosmological framework is correct.

Let's start our story by the beginning, when the first stars turned on within DM halos. No direct observation of these primordial galaxies is possible with the current instrumentation. Hydrodynamical simulations provide a tool to predict their formation.

In these simulations, baryonic matter cools down and falls within the dark matter halo potential well. When the density of baryons is high enough, star formation could start in a rotating disk of gas. But this picture is highly simplified. A first burst of star formation into a halo does not necessarily imply that a primordial galaxy will appear. The mass of the first stars created depend on the halo mass (Johnson 2011). In halos less massive than $10^6 \mathcal{M}_\odot$, the first stars to be created were probably more massive than 100 $\mathcal{M}_\odot$ (pop III.1). Such stars should quickly explode in supernova and blow away most of the gas into the intergalactic medium, preventing new star formation for several million years. In halos more massive than $10^6 \mathcal{M}_\odot$, the presence of some molecules (e.g. H_2, HD) should allow the gas to cool sufficiently to form stars less massive than 50 $\mathcal{M}_\odot$. The energy of the subsequent supernovae should not be able to blow away all the gas. These halos could maintain the star formation for a long time. Therefore, the first galaxies would appear at $z > 10$ in halos more massive than $10^6 \mathcal{M}_\odot$. Still, the formation of these primordial galaxies will stay an unexplored territory for the observers, as long as new facilities like the James Web Space Telescope (JWST) or giant telescopes (like the Extremely Large Telescope or the Thirty Meter Telescope) do not exist.

Then, the primordial galaxies will grow along cosmic time. In this picture, the galaxies grow fueled by the baryonic gas present within the DM structures. The galaxy stellar mass assembly is intimately linked to the hierarchical growth of the DM halos. Since DM halos are growing along cosmic time under the action of gravity, the amount of available gas in a given halo is growing too. The amount of baryonic gas present into the halo is set by the baryonic fraction $f_b = \Omega_b/\Omega_m = 0.17$. In simple models in which galaxies reach a quasi-steady state (Bouché et al. 2010, Lilly et al. 2013), the evolution of the specific star formation rate (hereafter $s\mathrm{SFR} = \mathrm{SFR}/\mathcal{M}_\star$) is coupled with the evolution of the specific Dark Matter Increase Rate ($sMIR_{DM}$) defined as $\dot{M}_H/M_H$ with M_H the mass of the DM halos (Lilly et al. 2013). It is valid if the gas consumption timescale is short in comparison to other timescales in the galaxy system. Based on N-body simulations and extended Press-Schechter formalism, Neistein & Dekel (2008) showed that $sMIR_{DM}$ increases as $\propto (1+z)^m$, with m ranging between 2.2 and 2.5. It explains qualitatively the sSFR increase with redshift (Noeske et al. 2007a, Elbaz et al. 2007).

By taking a really naive approach in which all this baryonic gas is converted into stars, we should obtain a galaxy stellar mass function (GSMF) with the same shape as the DM halo mass function (HMF). In the top left panel of Fig.1.1, we compare the local GSMF (blue and red points from Moustakas et al. 2013 and Baldry et al. 2012) with the GSMF that we would obtain if the baryons present into the halos were converted into stars. From this comparison, it appears clearly that baryons are not converted at the same rate depending on the considered halo mass. For a halo with $\mathcal{M}_{\mathrm{DM}} \sim 2 \times 10^{11} \mathcal{M}_\odot$, only 10% of the baryons were converted into stars. The exponential cut-off of the GSMF at high mass shows that a galaxy reaches a maximum mass around one thousand billions of solar masses, even within the most massive halos.

The difference in shape between the HMF and the GSMF is explained by the complexity of the physical processes which regulate the star formation. The star formation rate (SFR) is not only regulated by the cosmological accretion rate. The physical processes governing the conversion of the gas into stars are extremely complex and inefficient. Only a small fraction of the gas is converted into stellar populations. Numerous physical processes break partially the link between the DM halo mass and the stellar mass growth. In this dynamic cycle of baryons, several major aspects need to be considered:

- **The feeding of the galaxy in cold gas**: new gas is continuously inflowing in the halo because of the hierarchical growth of the DM structures. The gas need to be cold and its density should reach a threshold around $\Sigma > 10 \mathcal{M}_{\odot} pc^{-2}$ to trigger star formation. The SFR of the galaxy is directly proportional to the mass of cold gas (m_{gas}) present into the galaxy reservoir, following the Kennicutt-Schmidt relation $\mathrm{SFR} = \eta \times m_{gas}^{\kappa}$ (Kennicutt 1998). But only a small fraction of gas present in the halo can cool radiatively and penetrate the galaxy. Different cooling modes exist in the literature. The baryonic gas, initially heated at the virial temperature of the DM halo, will cool down by radiating photons (Silk 1977). The cold gas could also flow through DM filaments and cross the halo to directly feed the central galaxy, which is called "cold accretion" (Dekel et al. 2009). This "cold accretion" mode could be dominant at $z > 2$, boosting the star formation in the early Universe. But observational evidences of cold accretion are still limited (e.g. Cresci et al. 2009).

- **The star formation efficiency**: the internal conditions within a galaxy impact the efficiency in converting gas into stars. A large fraction of disk galaxies appear clumpy at $z \sim 2$ (e.g. Föester-Screiber et al. 2009) resulting from local instabilities. These instabilities could enhance the star formation efficiency (e.g. Bournaud et al. 2007). While such processes are probably not relevant in the local Universe, we do not know their impact at $z > 2$. The presence of a bulge or a bar could also modify the star formation efficiency. For instance, the presence of a bulge could stabilize the disk against fragmentation and lower the star formation efficiency (Martig et al. 2009). With the possibility of estimating the molecular gas mass, several studies have investigated the time depletion timescale (M_{gas}/SFR) as a function of redshift, stellar mass, SFR (e.g. Genzel et al. 2015). Saintonge et al. (2012) have shown in the local Universe that the presence of a bulge or a bar could impact the time depletion timescale.

- **AGN and SN feedbacks:** Energetic feedbacks from supernovae (SN) and active central nucleus (AGN) regulate the star formation activity. AGN feedback is believed to suppress the star formation in the most massive galaxies (e.g. Croton et al. 2006, Hopkins et al. 2008) while SN feedback slow down the star formation in low mass halos (e.g. Torrey et al. 2014). The energy released by AGN and SN could create gas outflows reaching hundreds of $\mathcal{M}_{\odot}$/yr (e.g. Lehnert et al. 1996). While such outflows are observed in several powerful star forming galaxies, the outflow rate depends on the galaxy and halo properties (e.g. Martin et al. 2012). In

some models, the mass loss in the system through outflows is directly proportional to the SFR with $\Psi = \lambda \times \mathrm{SFR}$ and λ the mass loading factor. The dependency of the mass loading factor on the halo mass is still debated, but λ could be inversely proportional to the halo mass (Lu et al. 2013, Lilly et al. 2013). In the primordial Universe, feedback of extremely massive PopIII stars could have a devastating impact on the formation of the first stellar populations (Bromm et al. 2011) and delayed the formation of the first galaxies. Massive black holes are already identified at $z > 6$ showing that they could also impact the galaxy formation in the primordial Universe. One crucial observable to constrain the efficiency of the SN feedback is the slope of the GSMF. Without SN feedback, the expected slope of the GSMF would be too steep (Fig.1 of Silk & Mamon 2013). The inclusion of the SN feedback is one way to reduce the SFR into the small mass halos because the gas could be ejected from the halos which have a shallower potential well. While SN can explain the difference at the low mass end, their energy is not sufficient to expel the gas in the deep potential well of massive halos.

- **Hot halo mode:** hydrodynamical simulations predict the formation of a virial shock in dark matter halos with $M_H > 10^{12} \mathcal{M}_{\odot}$. These massive halos can be maintained "hot" with the radiation of an AGN or extreme star-formation feedback (e.g. Croton et al. 2006, Cattaneo et al. 2006, Wang et al. 2008). Therefore, the central galaxy will not be fed anymore in cold gas. It will switch off the star formation in massive galaxies and convert them into quiescent systems. Such quenching is currently the best explanation for the high mass cut-off in the GSMF.

- **Mergers between galaxies:** mergers and interactions between galaxies will modify the star formation history by creating stochastic bursts of star formation, and eject some material within the intergalactic medium. Mergers will modify the mass distribution of the galaxies along time, by merging several galaxies into one. The major merger rate is well measured out to $z \sim 2$ (e.g. López-Sanjuan et al., 2012) and some first measurement out to $z < 4$ (Tasca et al. 2014). The merger rate could depend on the mass as shown at $z < 1$ (de Ravel et al. 2009). The tight relation between SFR and stellar mass with a 0.2-0.3 dex scatter (Elbaz et al. 2007, Daddi et al. 2007) puts a constraint on the maximum amount of stochasticity in the star formation history induced by major mergers (e.g. Rodiguiero et al. 2010). But we do not know how tight is the mass-SFR relation at $z > 3$. Minor mergers are also expected to impact significantly the mass assembly and size evolution. López-Sanjuan et al. (2012) showed that half of the size evolution and 25% of the mass growth in massive early type galaxies is explained by minor mergers at $z < 1$.

This list of physical processes is not exhaustive and the relative importance of these different processes has still to be determined. Such a list reveals the complexity of the galaxy formation and evolution, which could be better constrained with more observations.

1.3 An observational and statistical approach

"On appelle histoire naturelle la connaissance des choses, qui sont produites dans l'Univers, et que les hommes peuvent découvrir par les sens." Herman Boerhaave (1668-1738)

Powerful telescopes demultipliate our capacities to explore the Universe with the sense of sight. It is crucial to realize that we can not observe the galaxy evolution directly. The timescale associated to the evolution of one galaxy is too slow for any observer to catch its evolution in act. For instance, the timescale associated to one rotation of a spiral galaxy is one million times longer than the lifetime of an astronomer. Even by observing the merger between two galaxies with the current instrumentation at ten years of time interval, we would not observe any change in the galaxy positions.

Hopefully, one property of the Universe makes possible to study the galaxy evolution as an "observational" science. Because of the limited speed of light, the light emitted by a galaxy could travel billions of years before reaching us. We obtain some glimpses of an evolving Universe at various epochs and various locations, and we try to connect the dots with a coherent story. Still, we do not observe the same object at various epochs, but we can adopt a statistical approach to compare the galaxy properties of a "self-similar" galaxy population at different epochs.

If we were able to identify a galaxy property invariant over time, our work would be easier: for instance, if all the spiral galaxies were conserving the same rotational velocity along time, we could build several samples of galaxies at a given rotational velocity and see how the other properties evolve (e.g. the SFR or their stellar mass). Unfortunately, most of the galaxy properties are modified along cosmic time. For instance, a bar could develop and the number of arms could be modified. Some galaxies could even appear/disappear. It is not straightforward to link a galaxy population at a given epoch to the same population at later time. For instance, the most powerful star forming galaxies at $z \sim 4$ creating thousands of solar masses per year could become the most massive quiescent galaxies at $z \sim 1$ forming less than few solar masses per year. These two populations are well observed at $z \sim 4$ (SMGs) and $z \sim 1$ (massive ellipticals at $z \sim 1$), but it is extremely challenging to demonstrate the link between the two populations and be sure that one evolves into another (Toft et al. 2014). This is a fundamental difficulty that we will face along this manuscript. The general approach that we take as a community to solve this problem is a continuous interaction between observers and theorists. Observers generate detailed statistics on the galaxy properties at several epochs. Theorists establish models of galaxy formation and evolution which rely on known physical laws. Then, predictions of the models could be matched against observations. With a continuous interaction between these two communities, we establish a coherent story of the galaxy formation and evolution.

In this manuscript, our approach is to produce a statistical analysis extracted from large and representative galaxy samples. Incredible progresses in instrumental develop-

ment demultipliated our ability to conduct surveys at $z > 1$ in the last decade: the advent of wide-field cameras (i.e., those capable of covering 1 deg^2 or more at once), the construction of high-multiplex spectrographs on 8-m class telescopes, or the sensitivity of new CCD in near-infrared (hereafter NIR). Such samples have enabled the construction of very large ($> 10^5$) samples of galaxies covering $> 80\%$ of the age of the universe with accurate redshifts measured from the spectra. Our ability to sample the galaxy spectral energy distributions (hereafter SED) at numerous wavelength using imaging data offer an alternative/complementary route to estimate the galaxy redshifts, with a method called "photometric redshifts". Samples with several millions of galaxies are already assembled with such method (e.g. Coupon et al. 2015, Moutard et al. 2015) and billions of galaxies could be assembled in the next decade.

The results presented here are based on the data of the Cosmological Evolution Survey (COSMOS). The COSMOS survey covers a field of 2 deg^2 and is one of the best available fields to study the coevolution of galaxies, AGN and cosmic large scale structures. The 2 deg^2 field samples scales of 30-90 Mpc at $z = 0.2 - 4$ including 2 million galaxies (Scoville et al. 2007). An important feature of COSMOS is the development of complete, very sensitive, multi-wavelength datasets extending from hard X-ray to radio. In particular, a very deep coverage in medium band has been conducted with the Subaru telescope allowing an unprecedented precision of the photometric redshifts. This field is covered with high-resolution imaging with the Hubble Space Telescope (HST) (Koekemoer et al. 2007) which are crucial to study the evolution of the galaxy structure but also to perform weak lensing analysis (Massey et al. 2007). Hundred of studies related to galaxy evolution have been performed with the COSMOS data.

We concentrate in this manuscript on the galaxy stellar mass assembly. We produce simple and fundamental measurements based on the COSMOS data, which are powerful observables to characterize the relative importance of the various physical processes governing the galaxy growth.

1.4 Plan of this manuscript

The scientific analysis that I present in this manuscript are mainly based on the photometric redshifts of the COSMOS survey. In chapter 2, I will present the "photometric redshift" method that we used to obtain the galaxy distances. In particular, I will focus on the one implemented in the code *Le Phare* that we develop (Arnouts & Ilbert). I will describe the COSMOS survey and the quality of the photometric redshifts that we obtained in this field for two millions of sources, reaching a precision of 1% for the bright sources (Ilbert et al. 2009, 2013).

In chapter 3, we measure at which rate the galaxies create new stellar populations. Using direct tracers of the instantaneous SFR, we can derive the SFR Density (SFRD, $\mathcal{M}_\odot$/yr/Mpc^3) which characterizes the stellar mass formed per year in a given comoving volume. Since the first two seminal papers of Madau et al. (1996) and Lilly et al. (1996),

it has become an industry to measure the evolution of the cosmic SFRD to obtain the global star formation history. Using radio and infrared data, COSMOS brought new measurements out to $z = 4$ and I will summarize them. The Galaxy Stellar Mass Function (hereafter GSMF) and the its integrated value - the stellar mass density[1] - quantifies the stellar mass accumulated along cosmic time. By measuring the stellar mass density out to $z = 4$ in the COSMOS field, I provided a complementary probe of the cosmic star formation history. I will show that this result is consistent with the ones obtained with direct SFR tracers, producing a coherent picture of the global star formation history.

In chapter 4, I will measure the evolution of the specific SFR (sSFR defined as $\mathrm{SFR}/\mathcal{M}_\star$) with time. The sSFR characterizes the growth rate of a galaxy, i.e. the stellar mass instantaneously created over the one accumulated along its history. Such characterization appears as fundamental in the last years since it could be related to the underlying growth of the dark matter halos. I used two techniques to measure the sSFR evolution, complementary to what is done usually in the literature. Then, I will show that our estimate corresponds to what is expected from the cosmological accretion rate.

But not all the galaxies are following a single mainstream evolution. Galaxy evolution must take different paths in order to create the diversity of galaxy populations that we observe in the local Universe. One of the population which obviously took a different path is the elliptical population. This population in the local Universe is also associated with a much lower SFR. These galaxies are called "red sequence" galaxies, or "quiescent" galaxies. While the massive galaxies in the local Universe are dominated by this population, we do not expect them to be present in the primordial Universe. In chapter 5, we will bring some constraints on when this population acquired such specific properties along cosmic time. We will discuss possible physical processes which could explain why they differentiated from the bulk of the population along cosmic time.

Finally, I will conclude and present the perspective to study the stellar mass assembly and the star formation history in the next decade. I will present the exciting instrumentation becoming available in the next decade to study the galaxy evolution. The James Webb Space Telescope (JWST) and the extremely large telescope (ELT) will allow us tremendous progresses in the search for primordial galaxies. The Euclid mission will be essential to link the stellar mass and dark matter halo growth. Atacama Large Millimeter/submillimeter Array (ALMA) and the Square Kilometer Array (SKA) will be powerful telescopes to study the star-formation and link it to the gas content. Finally, I will show that the "photometric redshifts" method becomes a central tool to probe the cosmological parameters. This method is central for many current/future projects aiming to constrain the nature of dark energy using weak lensing tomography.

[1] GSMF: distribution of the galaxies according to their stellar mass in a given comoving volume. *Stellarmassdensity*: total stellar mass per volume unit for a given population

Along this manuscript, we use the standard cosmology ($\Omega_m = 0.3$, $\Omega_\Lambda = 0.7$ with $H_0 = 70$ km s^{-1} Mpc^{-1}). Magnitudes are given in the *AB* system (Oke 1974). The stellar masses are given in units of solar masses ($\mathcal{M}_\odot$) for a Chabrier (2003) IMF.

Chapter 2

Photometric redshifts

2.1 Introduction

Galaxy distances

A deep image of the sky into a blank field is the most basic observable one could obtain to study a population of galaxies. The galaxy positions and the apparent fluxes are the primary information extracted from such an image. While some statistical analysis can be performed, like galaxy number counts (Ellis 1997) or angular clustering (Maddox et al. 1990), the interpretation of these measurements remains really limited: all the modern surveys are looking for a crucial ingredient which is the galaxy distances.

Galaxy distances are deduced from the measurement of the "redshift". The expansion of the Universe stretches the electromagnetic spectral energy distribution (hereafter SED) toward longer wavelengths by a factor $1 + z$ with z being the redshift. Based on a model of the expansion of the Universe, one could relate the proper distance of a galaxy with its redshift following the equation:

$$d_p = a(t_0) \int_0^z \frac{c}{H_0 \sqrt{(\Omega_\Lambda + \Omega_m(1+z)^3 + (1-\Omega_m-\Omega_\Lambda)(1+z)^2)}} dz. \tag{2.1}$$

with c the speed of light, H_0 the Hubble constant, $a(t_0)$ the scale factor at t_0, Ω_Λ the effective mass density of dark energy and Ω_m the mass density measured from cosmological experiments (e.g. WMAP or Plank).

The observational difficulty consists in measuring the redshift of a large population of galaxies. Such a measurement consists in identifying some well known features into the galaxy SED and to measure by how much these features have been redshifted. For instance, there is a well known [OII] line doublet at 3726-3729Å or the Hα line at 6563Å from the Balmer series. In addition to the emission/absorption lines, the continuum of the galaxy SED includes also some well known features. For instance, there is a clear break into the galaxy continuum below 4000Å, explained by the absorption of photons more energetic than the Balmer limit at 3646Å and the combination of numerous

absorption lines around 4000Å by ionized metals in stellar atmospheres. A second break occurs below 1216Å explained by the absorption of light below the Lyman limit at 912Å and the absorption by the intergalactic medium along the line of sight below 1216Å. Therefore, one objective of modern surveys is to isolate such features, by tracking well known combinations of emission/absorption lines or breaks into the spectra continuum. Therefore the modern redshift surveys need to sample the galaxy SEDs.

Spectroscopic redshifts

The first method to sample the galaxy SED is to get the galaxy spectrum. When a galaxy spectra is available, the redshift measurement is based on absorption/emission lines, like the Hα or the [OII] lines. With such sharp features, you can measure precise and robust redshifts. For instance, VVDS (R=230) and DEEP2 (R=6000) get a precision around 10^{-3} and 10^{-4} on the redshift measurement, respectively (e.g. Le Fèvre et al. 2005, Newman et al. 2013). When several lines can be identified into the spectra, the confidence level in the redshift measurement is better than 97% (low risk of mismatch between two different redshifts). Moreover, several physical parameters could be measured on the spectra, depending on their quality (e.g. metallicity).

But this method is expensive in terms of telescope time. Despite the new generation of multi-object spectrographs which appeared in the last 10 years on 8-m class telescopes (VIMOS on VLT or DEIMOS on Keck), it is still extremely challenging to get spectra for more than a few percent of the sources detected on the primary image. For instance, the VVDS deep survey (Le Fèvre et al. 2005) which is one of the largest and deepest surveys up to date gather only 15%/7%/4% of the total number of galaxies in the CFHTLS/D1 field at $i^+ < 24/25/26$, respectively. More than 600hr have been dedicated to the spectroscopic follow-up of sources into the COSMOS field with 8-m class telescope (e.g. Lilly et al. 2009). With such an impressive effort, half of the sources have been targeted at $i^+ < 22.5$, but this number drops at 25%/12%/6% of the total number of galaxies in the COSMOS field at $i^+ < 24/25/26$. Even for a local survey as the SDSS, one million of spectra have been gathered over the 100 millions of sources detected on the SDSS images. While deep ground-based images reach easily a depth of $i \sim 26$ with the current instrumentation, it is extremely challenging to get a significant number of spectra at $i \sim 25$. A total exposure time of 40hr with VIMOS is necessary to gather a representative sample of 400 galaxies at $i^+ < 25$ (Le Fèvre et al. 2015) .

An additional difficulty is the restricted wavelength coverage of the spectra. For instance, the DEEP2 spectra typically cover the wavelength range 6500Å-9100Å. A robust spectroscopic redshift measurement is possible when the [OII] doublet falls into the spectra, which requires a preselection of the galaxy populations at $0.7 < z < 1.4$ based on their observed colors (Davis et al. 2003). This color preselection, applied in numerous current spectroscopic surveys (e.g. VIPERS, zCOSMOS faint), makes difficult the analysis of the results since we need to assess the representativity of the selected population. The VVDS spectra cover a larger wavelength range 5500Å-9500Å. The

chance to get several emission lines into the spectra (e.g. [OIII] and [OII]) is high with such a coverage. Therefore, no preselection in redshift has been done in this survey. The VVDS sample is the most representative spectroscopic sample of the $0.3 < z < 1.5$ Universe today. But the low resolution of the spectra does not allow to deblend the [OII] line doublet, which makes the redshift measurement less robust (15% of the galaxies with a flag 2 in the VVDS sample are misidentified). Moreover, our ability to measure a redshift depends on the redshift itself (e.g. Ilbert et al. 2005, Le Fèvre et al. 2013). Complex correction scheme still need to be applied when we derive global statistical properties. Since the [OII] line is redshifted in NIR for galaxies at $z > 1.5$, complex strategies need to be implemented to study the $z > 1.5$ Universe, using NIR spectrograph or blue grisms.

Photometric redshifts

Redshifts can also be estimated using multi-color imaging. By imaging the same field in different filters, we can get a sparse sampling of the SED at several wavelengths. This sparse sampling is sufficient to constrain the continuum shape and isolate broad features like the Lyman break of the Balmer break. This principle was first applied by Baum in 1957. He measured the photometric redshifts of elliptical galaxies at $z \sim 0.4$ based on color-color diagrams. A modern version of the photometric redshift method has been published by Puschell et al. (1982) who applied a first template-fitting procedure to radio galaxies. The principle of the template fitting-method is to take a set of reference SEDs (called templates), predict the colors expected for these templates along a grid of redshift, and then find the expected colors matching well the observed ones. This template-fitting method has been extensively tested on the *Hubble Deep field North* and *South* (HDF-N and HDF-S) between 1996 and 2004. Because of the faint magnitudes of the HDF sources (reaching $i_{AB} \sim 28$), photometric redshifts were necessary. Thanks to the quality of the Hubble telescope images in several bands combined with a significant sample of spectroscopic redshifts (~ 150), the HDF has been a perfect test bench for the photometric redshift method applied to the high redshift Universe. A new step has been made possible in the last decade with the apparition of extremely efficient multi-object spectrographs. Since 2003, the SDSS has been collecting hundred thousands of galaxy spectra at $z < 0.3$ and QSO out to z$\sim$ 6. Such a large spectroscopic sample has opened new opportunity for the photometric redshift estimate. Since 2003, several papers are published every year on the SDSS, testing new empirical methods to derive the photometric redshifts, like neural network (e.g. Firth et al. 2003, Collister & Lahav, 2004), "support vector machines" (Wadadekar, 2005) or "random forests" methods (e.g. Carliles et al. 2010). All these methods require a large and representative training set as the SDSS. In 2005-2006, thousands of spectroscopic redshifts of faint galaxies $I < 24$ became available with the VVDS (Le Fèvre et al. 2005, Le Fèvre et al. 2013) and DEEP2 (Davis et al. 2003). Such spectroscopic surveys have enable to test and assess the quality of the photometric redshifts over a large range of redshift/magnitude/type (Ilbert et al.

2006). Nowadays, the number of spectroscopic redshifts available out to $z \sim 1.5$ reaches 100000. Still, empirical methods like neural networks have not been proved efficient yet at intermediate/high redshift. In the last decade, template-fitting methods have continuously evolved, by improving some physical recipes but also by calibrating some part of the template-fitting method using the spectroscopic information. Since part of my work was dedicated to such studies, I will focus on this aspect of the photometric redshift method in the section 2.2.

Pro and con of using photometric redshifts

Obviously, photometric redshifts have their pros and cons. The first advantage of the photometric redshifts is that we can derive a distance measurement from any source of the imaging survey. Each source which is detected in several bands of the image can have a photo-z. Therefore, we can gather extremely large samples of galaxies (e.g. 5 millions of galaxies in the CFHTLS Wide, Coupon et al. 2009), for sources as faint as $i^+ \sim 26$ which is a common limit for modern deep imaging surveys (CFHTLS Deep, COSMOS, CDFS, SXDS). In principle, we do not have to worry about incompleteness in the redshift survey and we cover a large wavelength range including NIR in most of the current deep fields (e.g. the CFHTLS Deep fields in Bielby et al. 2012, all the Spitzer surveys like S-COSMOS in Sanders et al. 2007 or SERVS in Mauduit et al. 2012). The price to pay is the precision of the redshift measurement. Since the measurement is mainly based on the continuum and not on sharp features of the SED like emission lines, the precision is lower than any result obtained even with low resolution spectroscopy. Typically, the precision of the photo-z is 3-5% using broad band data, but the precision reaches 0.5% using medium band imaging data. It is still a factor 10 worse than the precision obtained with low resolution spectra. Some scientific analysis are difficult to carry on with photometric redshifts, especially studies focusing on the galaxy environment and clustering. But for many scientific analysis, such a precision is perfectly acceptable (e.g. luminosity or mass function). Typical photo-z with a precision of $\sigma_{\Delta z/(1+z_s)} \sim 0.02 - 0.04$ ($\Delta z = z_s - z_p$) are widely used to study the evolution of galaxy stellar masses and luminosities (e.g. Fontana et al. 2000, Wolf et al. 2003, Gabasch et al. 2004, Caputi et al. 2007, Arnouts et al. 2007), for angular clustering analysis (e.g. Heinis et al. 2007, McCracken et al. 2008, McCracken et al. 2015), to study the relation between galaxy properties and environment (e.g. Capak et al. 2007), to trace large-scale structures (Mazure et al. 2007, Scoville et al. 2013) and to identify clusters at high redshift (Wang & Steinhardt 1998). The robustness of a photo-z sample is probably not so far from the one of a spectroscopic sample. For instance, we find less than 1% of catastrophic failures in the photometric redshifts at $i < 22.5$ in the COSMOS field (Ilbert et al. 2009) which is comparable to the best spec-z samples. At fainter magnitudes, the fraction of catastrophic failures increases in photo-z samples and can reach few percents (e.g. 4% at $i^+ < 24$ in CFHTLS, Ilbert et al. 2006). But the fraction of spec-z which are not measured or misidentified reaches 20% in a pure magnitude limited sample $i^+ < 24$ (le Fèvre et al. 2005).

The photometric redshift method suffers from a severe limitation: while the robust spec-z are well identified (several lines identified on the spectra produced a spec-z which is > 99% reliable), the photo-z methods have not reached the maturity to statistically isolate the sources that we can trust at > 99%. Most of the photo-z codes produce a Probability Distribution Function (PDF) associated to the photo-z. In principle, we could use these PDFs to isolate the most robust photo-z. But numerous hypothesis are done on the underlying galaxy populations, for template-fitting method (e.g. the set of template) and for empirical methods (the representativity of the training set). There is always the possibility that some hypothesis are not valid for specific redshift/magnitude/color ranges. The photo-z codes have not yet demonstrate their ability to keep only the photo-z that we can trust at 99%. And when we will achieve it, we will face the same problem as for the spec-z sample, i.e. the need to correct for a complex incompleteness. Therefore, one major difficulty in the photo-z samples is to assess their reliability. This step requires deep and representative spectroscopic samples.

Photometric redshifts into the community

In the last two decades, the photometric redshift method became a common tool to measure the galaxy distances. As shown in Fig.2.1, the number of papers including the words "photometric redshift" in their abstracts (source: ADS) increased from 40 per year in 1995-1999 to 280 per year since 2010. A general increase of the total number of publications per year explains part of this trend. In Fig.2.1, we show the fraction of papers including the word "photometric redshift" in their abstracts normalized by the number of papers including the words "redshift" and "galaxy". There is a continuous increase of the fraction of extra-galactic studies using the photometric redshift method. This increase could be explained by several factors:

- an increased sensitivity of the CCD leading to a continuous growth of available multi-color dataset. A spectroscopic follow-up of these surveys is too expensive in term of telescope time;
- a better confidence into the photo-z method, thanks to the multiple studies on the HDF fields and recent works tested against thousands of spec-z;
- the release of public photo-z codes like Hyperz (Bolzonella et al. 2000), Le Phare (Arnouts et al. 2002, Ilbert et al. 2006), BPZ (Benítez 2000), EAZY (Brammer et al. 2008).

While the fraction of papers using the photo-z method reaches only 10% today, our reference sample contains papers published in the local Universe for which photo-z are not crucial (because of the representative spectroscopic coverage performed by the SDSS), papers based on simulations, and papers which do not necessarily indicate the use of "photometric redshift" in their abstracts. We also note that the use of the photo-z becomes more and more popular into the papers related to cosmology. Indeed, the photo-z is a

central ingredient to perform weak lensing tomography. For the future wide surveys aiming to constrain the nature of dark energy and using weak lensing tomography (like DES, HSC, Euclid, LSST), we will need to measure photometric redshifts for hundred millions of galaxies.

While photometric redshifts and spectroscopic redshifts are often opposed, there is a strong synergy between these two methods in deep surveys: 1) photo-z are needed to test the representativity of the spec-z samples and even to select the spectroscopic targets; 2) spec-z are crucial to test the reliability of the photo-z sample and could be used to improve the photo-z. Therefore, all the modern surveys have a strategy to gather both photometric redshifts and spectroscopic redshifts.

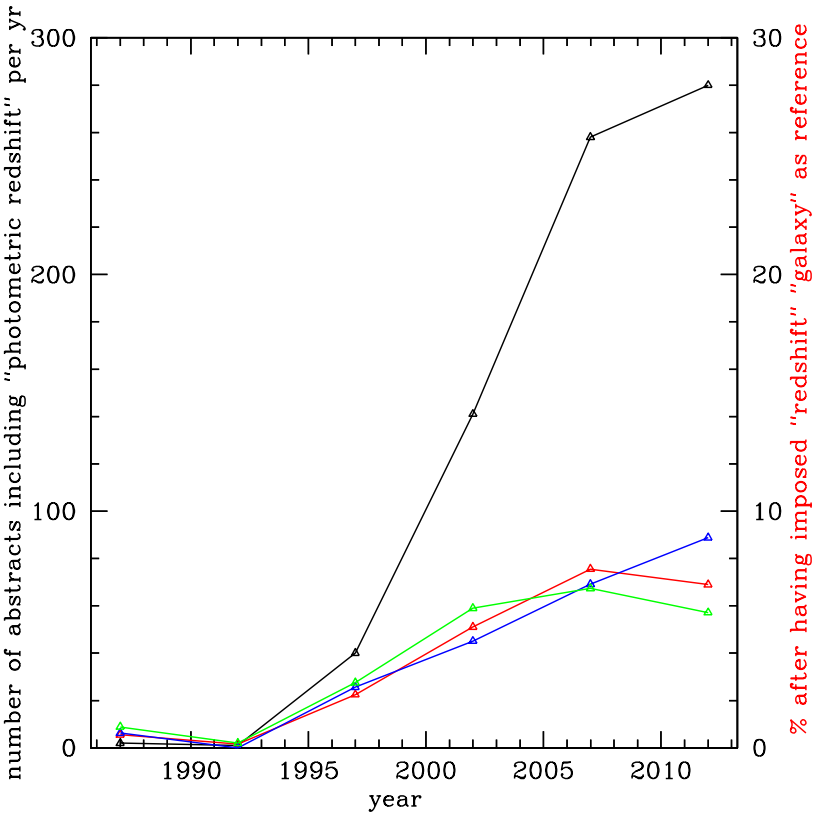

Figure 2.1: Number of abstracts including the word "photometric redshift" per year (source ADS/NASA). The red curve is the fraction of abstracts (in %) including the words galaxy-redshift-photometric redshift over the ones including galaxy-redshift. We add the word "cosmology" for the blue curve and "evolution" for the green curve".

2.2 Template-fitting method of the code Le Phare

Numerous codes are based on this template-fitting procedure. In Dahlen et al. (2013), more than 13 codes based on template-fitting have been applied to the same dataset.

One of the first codes to be released is the well known "Hyperz" code (Bolzonella et al. 2000). In this chapter, I will use our own code *Le Phare*[1] (Arnouts & Ilbert) to compute photometric redshifts. The standard χ^2 method for this code is described in Arnouts et al. (1999, 2002). We continuously improved this code (e.g. Ilbert et al. 2006, Ilbert et al. 2009). I will describe the main features of this code.

2.2.1 The standard template-fitting method

The basis of the template-fitting method is to compare the colors expected for a set of reference SEDs (called templates) at various redshifts and the observed colors of a galaxy. The redshift providing the best match between the observed colors and the expected ones is called "photometric redshift".

A crucial ingredient in the template-fitting method is the definition of the set of templates. There are a lot of possibilities, ranging from the use of stellar population synthesis models to generate simulated SEDs, to the use of real observed spectra. The choice of the templates will be discussed in Section 2.2.3. Because of the dust present into the studied galaxies, an additional attenuation could be applied to the templates, as discussed in section 2.2.4. Emission lines could also be included into the templates as discussed in section 2.2.5.

Then, each template is redshifted along a grid of redshift (the redshift step should be lower than the expected photo-z precision) and convolved with the filter transmission curves (including instrument efficiency). The opacity of the inter-galactic medium (Madau 1995) is also taken into account. With such a procedure, the expected colors are predicted for a large variety of galaxy SEDs, at different redshifts. Finally, we obtain the photometric redshift by comparing the observed fluxes and the ones predicted for the set of templates using the merit function χ^2, defined as:

$$\chi^2(z,T) = \sum_{f=1}^{N_f} \left(\frac{F^f_{\rm obs} - A \times F^f_{\rm pred}(z,T)}{\sigma^f_{\rm obs}} \right)^2 , \tag{2.2}$$

where $F^f_{\rm pred}(T,z)$ is the flux predicted for a template T at redshift z. $F^f_{\rm obs}$ is the observed flux and $\sigma^f_{\rm obs}$ the associated error. The index f refers to the considered filter and N_f is the number of filters. The normalization factor A is computed as

$$A = \sum_{f=1}^{N_f} \left(\frac{F^f_{\rm obs} F^f_{\rm pred}}{\sigma^f_{\rm obs}} \right) / \sum_{f=1}^{N_f} \left(\frac{F^f_{\rm pred} F^f_{\rm pred}}{\sigma^f_{\rm obs}} \right) \tag{2.3}$$

following Arnouts et al. (1999). A probability is associated to each χ^2 value: $P(z,T) = exp(-\frac{\chi^2(z,T)}{2})$. We derive the marginalized probability distribution of the redshift by sum-

[1] www.lam.oamp.fr/arnouts/LE_PHARE.html

ming all the probabilities obtained at a given redshift:

$$P_{marginalized}(z) = \sum_{\text{allmodels}} exp(-\frac{\chi^2(z,T,A)}{2}).$$

There are several ways of extracting the photometric redshift value from the PDF:

- the photometric redshift could be considered as the median of the PDF;
- the photometric redshift could correspond to the lowest χ^2 value.

The peak of the marginalized probability distribution does not necessarily correspond to the redshift at the minimum χ^2.

2.2.2 Sensitivity of the photo-z to the photometric absolute calibration

In 2004, we applied the standard χ^2 method described in section 2.2.1 on the BVRI imaging data taken on the VVDS-02h field with the CFH12K camera (McCracken et al. 2003). For the first time, we were able to test the photometric redshifts with few thousands of spectroscopic redshifts from the VVDS survey (Le Fèvre et al. 2005). A clear bias was visible into the photo-z for bright galaxies $I_{AB} < 22$ at $zs < 0.5$. In this redshift range, the Balmer break is well encompassed between the BVRI filters. Calibration of the zero-points was suspected to be the origin of such a bias. Indeed, the χ^2 template-fitting method is meaningful only if the $color - z$ relation predicted from the templates is a good representation of the observed $color - z$ relation. Uncertainties in the absolute calibration of the images could lead to systematic differences between the predicted and observed $color - z$ relations.

Therefore, we developed a new method of zero-point calibration using the VVDS spectroscopic sample (Ilbert, 2004, PhD and Ilbert et al. 2006). For the calibration purpose, we limit ourselves to the spectroscopic sample and we set the redshift to the spec-z value (the redshift is not anymore a free parameter in the fit). We minimize the merit function:

$$\psi^2 = \sum_{i=1}^{i=Ngal} \left(\sum_{f=1}^{N_f} \left(\frac{A_i \times F^f_{\text{pred,i}} \times 10^{-0.4 s^f} - F^f_{\text{obs,i}})}{\sigma^f_{\text{obs,i}}} \right)^2 \right)$$

where s^f are the free parameters that we want to obtain. The s^f values correspond to the offsets (in mag) that allow the best match between the observed and predicted magnitudes. For random, normally distributed uncertainties in the flux measurements, the average deviation s^f should be zero. Instead, we observe some systematic differences which could reach 0.1 magnitude. We then proceed to correct the predicted apparent magnitudes for these systematic differences. s^f is the estimated correction that we apply to the apparent magnitudes in a given filter f. If we repeat a second time the procedure of template-fitting

after having adjusted the zero-points, the best-fit templates may change. Therefore, we applied this method iteratively. We stopped when the process converged. We implement this procedure in an automatic way inside the code *Le_Phare*. This method could be applied automatically for any survey having a significant spectroscopic redshift sample. A special warning is necessary: such offsets could also be explained by an inaccurate knowledge of the filter transmission curves, by the use of an incomplete or inaccurate set of templates or dust attenuation.

This method has proven to be successful in removing the obvious redshift bias present into the CFH12K photometric redshift catalogue (Ilbert, 2004, PhD). We showed in Ilbert et al. (2006) that the standard method (no calibration of the zero-points) was also producing unexpected bias using the CFHTLS data in the VVDS F02h field. We were able to reduce the bias by applying the same calibration method. We emphasize that the offsets s_f were below 0.1 mag in all bands. Despite the small values of these offsets, bias of $\Delta z \sim 0.1$ were observed in the photo-z (Fig.3 of Ilbert et al. 2006). By analyzing the CFHLens data (same raw data than the CFHTLS but reprocessed by Erben et al. 2013), Hildebrandt et al. (2012) showed that they do not need anymore the calibration of the zero-points. They interpret this success by the Point Spread Function (PFS) homogeneization performed in all filters. In other words, they conclude that the PSF variation band-to-band was explaining that the observed colors were inconsistent with the predicted ones. Therefore, a calibration of the zero-points would be not necessary with a careful treatment of the PSF variations. But in the meantime, a new reduction of the CFHTLS data (version T007) has obtained a different absolute calibration which could differ by more than 0.1 mag compared to the previous release (Moutard et al., 2015). Since the T007 calibration is supposed to be more accurate (Regnault et al. 2009), it shows that even with a careful reduction, a significant variation of the zero-points is possible. Moreover, we demonstrate in the COSMOS field that even with PSF homogenised images and 30 bands, we need to calibrate the zero-points. The same conclusion was reached by the PHAT2 experiment (Hildebrandt et al. 2010): the codes producing the most accurate photo-z on PSF homogenized catalogue (GOODS-N field) were calibrating their zero-points. A recent paper by Dahlen et al. (2013) on the CANDELS field reaches the same conclusion, using HST images and a photometric catalogue obtained using the TFIT algorithm (Laidler et al. 2007) specially dedicated to produce colors not affected by PSF variations. Therefore, while the calibration of the zero-points should be avoided if possible (because we would identify why the predicted and observed colors are inconsistent), numerous surveys showed that this procedure is necessary to remove the possible biases in the photo-z. It demonstrate the need for a synergy between photometric and spectroscopic surveys.

2.2.3 The set of templates

Synthetic templates

Synthetic templates can be created using Stellar Population Synthesis (SPS) models. These models predict the evolution of a galaxy SED along cosmic time, depending on the considered star-formation history and metallicity. Numerous codes can be used to produce such templates (e.g. Silva et al. 1998, Bruzual & Charlot 2003, Fioc & Rocca-Volmerange 1996, Maraston 2005, Conroy 2012). These models have the advantage to be physically motivated. Therefore, physical information on the galaxy could be extracted from the fit (e.g. the stellar mass, the SFR or the star formation history). Complex star formation histories including multiple bursts of star formation could be considered when the set of templates is created (Pacifici et al. 2015). These models can include dust recipes (Charlot & Fall 2000, Silva et al. 1998). Some codes like GRASIL (Silva et al. 1998) allow a complex treatment of dust but they multiply the amount of possible SEDs which could be created.

By considering a large range of possible star formation histories, metallicities, or dust mixture, the representativity of the set of template increases. But at the same time, the risk of degeneracy in the color-redshift space increases: a same color could be produced by two different templates at two different redshifts. In most of the template-fitting codes, each template as an equi-probability to be selected (flat prior). By including rare star-formation histories or extreme metallicities in the set of templates, we create new degeneracies in color-z space and we increase the risk of catastrophic failures for the bulk of the galaxy population. Therefore, people are effectively applying a prior in most of the template-fitting codes: a limited number of star-formation histories or metallicities is considered. For instance, the standard library of Hyperz includes 8 possible star formation histories (exponentially declining SFR) and one possible metallicity. The difficulty is to decide the most appropriated set of template, depending on the balance between the representativity and the risk of catastrophic failures.

In Ilbert et al. (2009), we introduce a new set of templates generated by Polletta et al. (2007) with the code GRASIL (Silva et al. 1998). Polletta et al. selected their templates for fitting the VVDS sources (Le Fèvre et al. 2005) from the UV-optical (CFHTLS: McCracken et al. 2007) to the mid-IR (SWIRE: Lonsdale et al. 2003). The 9 galaxy templates of Polletta et al. (2007) include 3 SEDs of elliptical galaxies and 6 templates of spiral galaxies (S0, Sa, Sb, Sc, Sd, Sdm). We found that the blue observed colors seen in the spectroscopic sample were not fully reproduced by the Polletta et al. (2007) templates. We therefore generated 12 additional templates using Bruzual & Charlot (2003) models with ages ranging from 0.03 Gyr to 3 Gyr. We extend the BC03 templates beyond $3\mu m$ rest-frame using the Sdm template of Polletta et al. (2007). The full library of template SEDs, 9 from Polletta et al. (2007) and 12 from Bruzual & Charlot (2003). But this set of templates was chosen arbitrarily and empirically to provide good photometric redshifts into the COSMOS field. Even if these templates have been successfully used in other fields (CANDELS, Dahlen et al. 2013 and GOODS-N, Hildebrandt et al. 2010), nothing guaranties that we found an optimal balance between the representativity of the set of templates and the risk of catastrophic failures.

In the future, we should develop a new procedure which would automatically define the best set of templates depending on the wavelength coverage available. Finally, Brammer et al. (2009) used another solution. They pick up the 6 most common SEDs into a semi-analytical model. These 6 templates are their basis. Then, they allow any combination of these 6 templates to fit their data.

Empirical templates

Empirical templates are extracted from real spectra. The most famous set of templates is a combination of four observed spectra (Ell, Sbc, Scd, Irr) from Coleman, Wu and Weedman (CWW; 1980) and few starburst spectra from Kinney (1996). These set of templates is often limited to these six local templates. Since these spectra are taken in the optical, they need to be extrapolated to the ultraviolet ($\lambda < 2000$Å) and near-infrared wavelengths using the BC03 synthetic models (Bruzual & Charlot 2003). This set of local template has been extensively used successfully in the HDF and numerous other surveys (e.g. Sawicki 1997, Fernández-Soto et al. 1999, Arnouts 1999, Brodwin et al. 2006). Their small number significantly reduces the possible degeneracies between predicted colors and redshift (Benítez 2000). These six templates are often linearly interpolated to improve the sampling of the redshift-color space and therefore the accuracy of the redshift measurement.

Optimized templates

Several studies have defined a procedure to modify an existing set of template (empirical or theoretical) in order to obtain a lower bias in their photo-z. The only objective of the optimized templates is to provide accurate photo-z, and their physical meaning could be lost during the optimization. We developed a simple method in Ilbert et al. (2006) in order to optimize our set of templates. We started with the common CWW empirical templates. We optimized our templates using 2867 VVDS spectroscopic redshifts of galaxies. Since the apparent magnitude measured in the filter λ_{eff} provides the rest-frame flux at $\lambda_{eff}/(1+z_i)$ for a galaxy with a spectroscopic redshift z_i, we were able to reconstruct the rest-frame flux over a continuous range of rest-frame wavelengths for a given galaxy population. Such a method is the same used in Coupon et al. (2015) with the COSMOS templates. More sophisticated methods have been developed. For instance, Budavári et al. (2000) used a PCA reconstruction of a set of template. Some template-fitting codes are even reconstructing their SEDs automatically depending on the considered redshift, as ZEBRA (Feldmann et al. 2006).

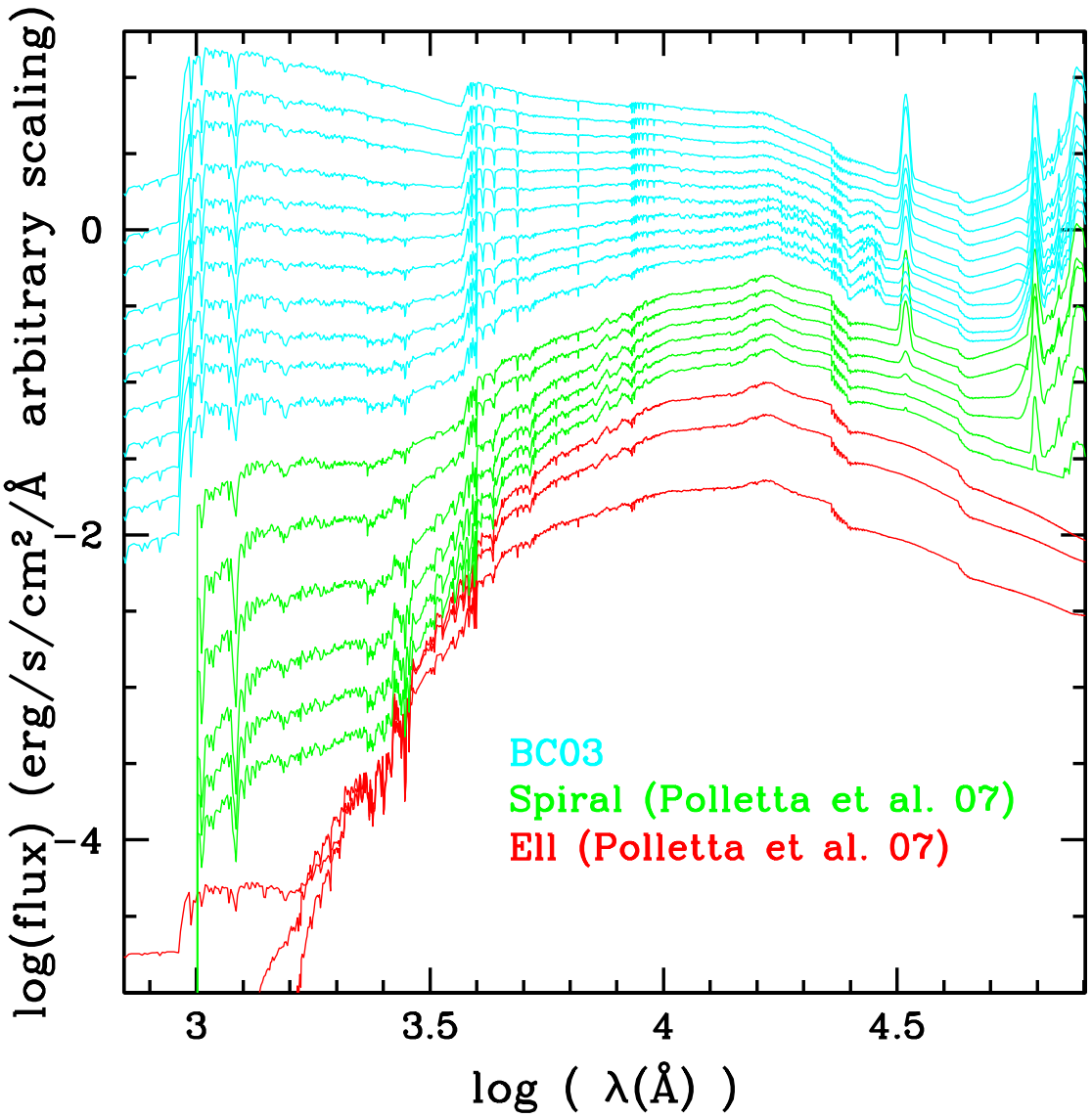

Figure 2.2: SED templates from Ilbert et al. (2009). The flux scale is arbitrary. The top 12 SEDs (cyan) are generated with Bruzual & Charlot (2003). The spiral (green) and elliptical (red) SEDs are from Polletta et al. (2007).

2.2.4 Dust extinction

The dust present into the interstellar medium will absorb and scatter the light emitted by the stellar populations of a considered galaxy. The dust extinction reddens the intrinsic shape of the spectra: $f_{obs} = f_{intrinsic} 10^{-0.4E(B-V)\times k(\lambda)}$ with f_{obs} the observed flux, $f_{intrinsic}$ the intrinsic flux emitted by the stellar populations, $E(B-V)$ is the color excess in $B-V$ and $k(\lambda)$ is the reddening curve (k decreases with λ). For a common galaxy, the $U-R$ color

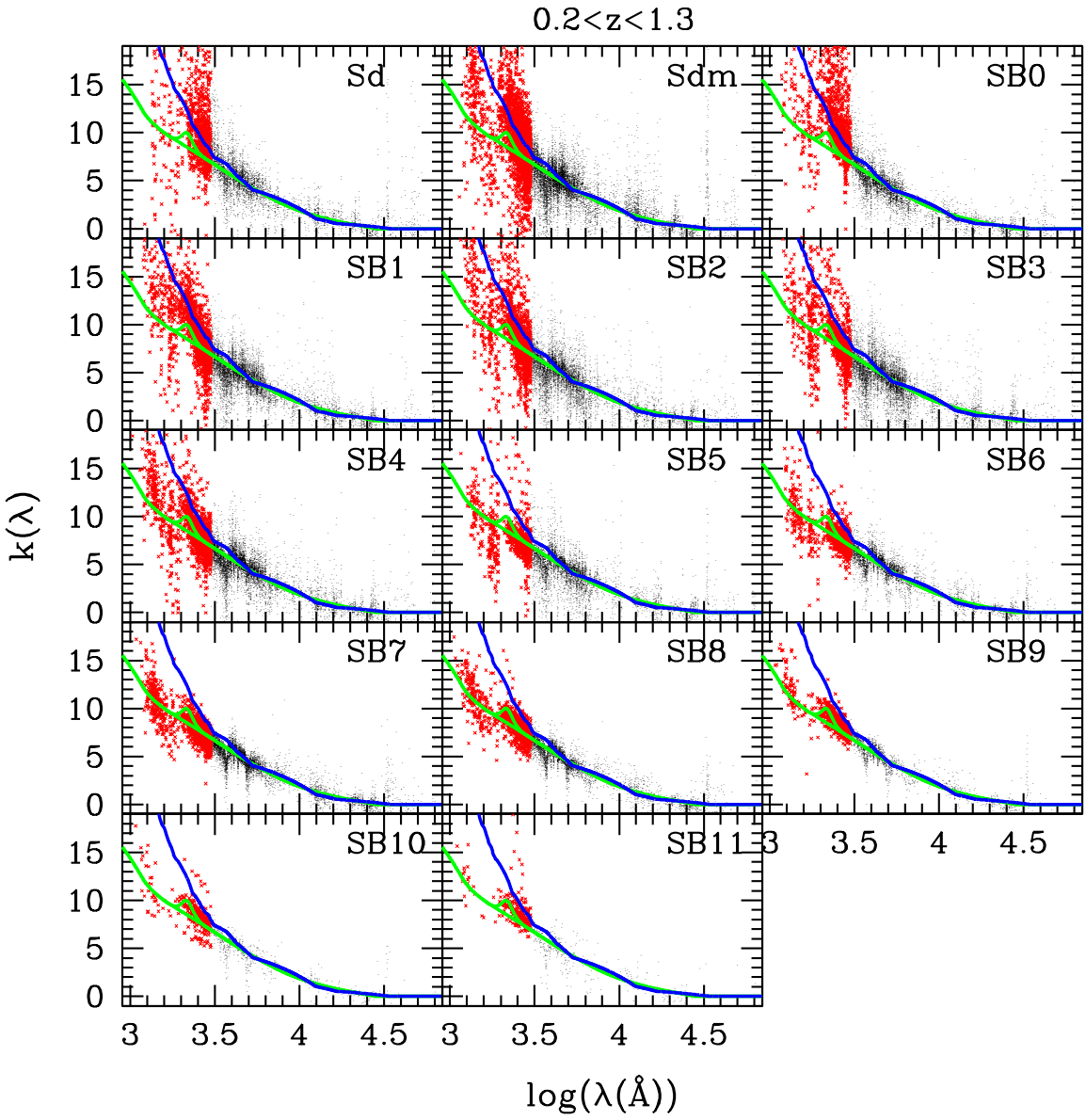

Figure 2.3: Attenuation by dust as a function of λ. The points are the extinction $A_i/(E_i(B-V))$ estimated from the galaxies with a spec-z (see §3.4). The red points at $\lambda < 3000$Å are not used to estimate $E_i(B-V)$. The Prevot et al. (1984) and Calzetti et al. (2000) extinction curves are shown with the blue and green solid lines, respectively. The Prevot et al. (1984) extinction law is rescaled to the same A_V as the Calzetti law by applying a factor 4.05/2.72. The extinction curve derived by Prevot et al. (1984) is used for the galaxies redder than SB3 and the Calzetti et al. (2000) extinction law for the galaxies bluer than SB3.

will be reddened by 0.5 mag while it reaches 3 mag for ULIRGs (Ultra Luminous Infrared galaxies). Therefore, we need to model carefully the impact of dust reddening on the galaxy SED. Having a good modeling of the dust extinction is particularly important to get accurate photo-z at $z > 1.5$: deep surveys concentrate a large wheel of multi-color data in optical, which traces the UV rest-frame part of the SEDs at $z > 1.5$. For instance, 23/30 filters cover a wavelength range bluer than the Balmer break at $z > 1.5$ in the COSMOS field.

In several template-fitting codes, the dust reddening is added as a free parameter (it is the case in Hyperz, *Le_Phare* but not in EAZY and BPZ). $E(B-V)$ can take any value between 0 and a maximum value which is often taken around 0.5, depending on the considered galaxy population[2]. Numerous reddening curves exist in the literature and we do not know a priory which reddening curve is more suitable for a given galaxy. The Calzetti et al. (2000) reddening curve derived for local starburst galaxies is one of the most commonly used. This is the default reddening curve in Hyperz. Ilbert et al. (2006) adopted the dust reddening curve measured in the Small Magellanic Cloud (Prevot et al. 1984). However, considerable changes in the reddening curve are expected from galaxy to galaxy. Maraston et al. (2006) considered as a free parameter the different reddening curves (e.g. Milky Way, large and small Magellanic clouds and Calzetti). But combining simultaneously all the reddening curves multiplies the risk of degeneracies in the color redshift-space which makes this method difficult to apply for large surveys.

In Ilbert et al. (2009) and as shown in Fig.2.3, we use an empirical approach to decide which reddening curves should be used, depending on the considered template. Using the large spectroscopic sample, we set the redshift to the spectroscopic redshift value. Then, we determine the best fit-template and the appropriate color excess $E(B-V)^{\rm best}$. Since the reddening curves do not differ strongly at $\lambda > 3000$Å, we fit the templates using only the passbands with $\lambda > 3000(1+z)$Å. With this procedure, the $E(B-V)^{\rm best}$ value does not depend significantly on the adopted reddening curve. Since the reddening curves differ strongly at $\lambda < 3000$Å, we use the rest-frame observed SEDs at $\lambda_{\rm rest-frame} < 3000$Å to discriminate between the different reddening curves. We found that the Small Magellanic Cloud reddening curve (Prevot et al. 1994) was well suited for galaxies redder than the starburst template SB3 (the red half part of our templates). For galaxies bluer than SB3, the Calzetti et al. (2000) reddening curve is found to be more appropriate. A broad absorption excess at 2175Å (UV bump) seems necessary to explain the UV flux in some starburst galaxies. The presence of this UV bump can be seen in a theoretical modeling of the Calzetti law (Fischera et al. 2004) and in the K20 sample of high redshift galaxies at $1 < z < 2.5$ (Noll et al. 2007). We allow an additional bump at 2175Å for the Calzetti reddening law if it produces a smaller χ^2. Using a similar set of medium band data in the CDFS field, Buat et al. (2011) found that the presence of a UV bump was necessary to explain the galaxy SEDs of an infrared selected population.

[2]In the case of photo-z computed for IR sources or to investigate possible contaminants in $z > 6$ samples, the value of $E(B-V)$ should be pushed at 1.5.

Surprisingly, the template-fitting code EAZY is able to produce accurate photometric redshifts without adding extinction as a free parameter. They include extinguished galaxies in their set of templates. Since they measure the photo-z by allowing any linear combination of their templates, extinction is probably included depending on the relative importance of this template.

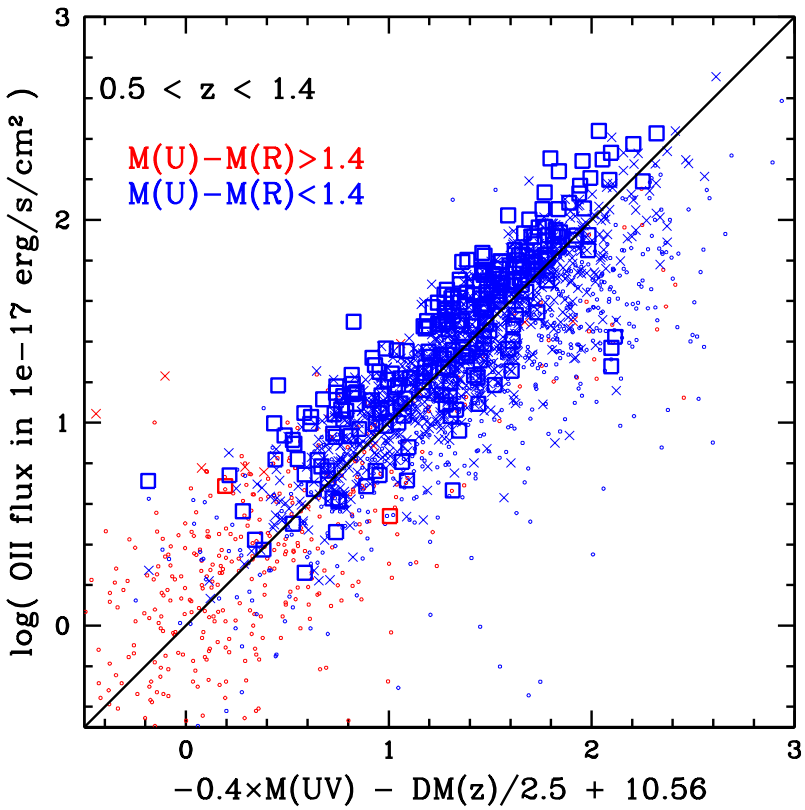

Figure 2.4: Relation between the [OII] flux and the absolute magnitudes in UV (2300Å). The solid line corresponds to the relation obtained by applying the Kennicutt (1998) relations between SFR_{OII} and SFR_{UV} as used here to include emission line fluxes in the photo-z fitting and the points are observed emission line fluxes from VVDS (Lamareille et al. 2009). The UV luminosities and [OII] fluxes are corrected for dust extinction.

2.2.5 Emission lines

In the last few years, several analysis showed that it is essential to include the emission lines within the templates, in order to compute photometric redshifts using medium band data (Ilbert et al. 2009, Cardamone et al. 2010) and to the derive the properties of primordial galaxies at $z > 5$ using a template-fitting method (Schaerer et al. 2009, de Barros et al. 2012).

Figure 2 of Ilbert et al. (2009) shows the observed colors versus the spectroscopic redshifts. When the color involves a medium band, we detect some peaks in the observed colors (top right panel). The observed variations in color over a really small redshift range are well explained by the contribution of emission lines like Hα, [OIII], and [OII]. Therefore, it is crucial to include emission lines within the templates when we compute photo-z with medium band data.

In Ilbert et al. (2009), we adopt a simple procedure. We estimate the [OII] emission line flux from the UV luminosity of the rescaled template, using the Kennicutt (1998) relations. In the template fitting, a UV rest-frame luminosity corrected for dust extinction can be computed at every step of the redshift/template/extinction grid (the rescaling factor A is taken into account in the UV luminosity). The UV luminosity (at 2300Å) is then related to the SFR using the relation $\mathrm{SFR}\,(\mathcal{M}_\odot\ yr^{-1}) = 1.4\times10^{-28}L_\nu\,(erg\ s^{-1}Hz^{-1})$ from Kennicutt (1998). This SFR can then be translated to an [OII] emission line flux corrected for dust extinction using the relation $\mathrm{SFR}\,(\mathcal{M}_\odot\ yr^{-1}) = (1.4\pm0.4)\times10^{-41}L_{[\mathrm{OII}]}\,(erg\ s^{-1})$ (Kennicutt 1998). This translates to :

$$log(F_{[\mathrm{OII}]}) = -0.4\times M_{\mathrm{UV}} + 10.56 - \frac{DM(z)}{2.5} \tag{2.4}$$

where DM is the distance modulus, $F_{[\mathrm{OII}]}$ is expressed in units of $10^{-17}\,erg\ s^{-1}cm^{-2}$ and M_{UV} is the dust corrected UV(2300Å) absolute magnitude. Using the VIMOS data, we have checked that our relation is in broad agreement with the [OII] line fluxes from VVDS (Lamareille et al. 2009), as shown in Fig.2.4. While our relation predicts an [OII] flux systematically lower by a factor 1.3 in comparison to the observed [OII] flux, this factor could be easily explained by our assumption that the continuum color excess is the same as the nebular color excess (while some papers points out a possible factor 0.44, as in Calzetti et al. 2000).

With our procedure, we can predict for each galaxy the [OII] flux at every redshift/template/extinction combination. For the other emission lines, we adopt intrinsic ratios of [OIII/OII] = 0.36; [Hβ/OII] = 0.61; [Hα/OII] = 1.77 and [Lyα/OII] = 2 (McCall et al. 1985, Moustakas et al. 2006, Mouhcine et al. 2005, Kennicutt 1998). When we apply an additional extinction to the template, we modify these ratios accordingly. Then, we sum the emission line fluxes to the template continuum before integrating through the filter transmission curves. Because of the large uncertainties present in our method, we allow the emission line fluxes to vary within a factor 2 during the χ^2 fitting procedure.

We applied this method successfully to the COSMOS survey. By adding the emission lines to our set of templates, we improved the precision of our photo-z by a factor 2. Without the emission lines, our photo-z precision was limited at 2%. We were able to reach a precision of 0.8% using this method. The same method was adopted by Cardamone et al. (2010) when they computed the photo-z with EAZY on the CDFS field.

We also used our analytical relation to associate predicted emission lines fluxes to any galaxy in the COSMOS photo-z catalogue. While the predicted fluxes is a rough estimate, such a catalogue was useful to predict the number of sources in future large spectroscopic surveys (Jouvel et al. 2009, 2013, Schlegel et al. 2011).

2.2.6 Bayesian approach

External knowledge could be introduced in the photo-z measurement. When the wavelength coverage does not bring enough information to break some degeneracies of the color-z space, external information could help in breaking the degeneracies. For instance, the photo-z estimate relies on galaxy colors. Therefore, a galaxy with an apparent magnitude of $I_{AB} = 20$ could have a color similar to a galaxy at $z \sim 4$. But such a bright apparent magnitude is very unlikely for a galaxy at high redshift. This kind of information could be introduced in the template fitting method using a Bayesian formalism.

In the CFHTLS survey, the only bands available are u, g, r, i, z. Lyman break galaxies at $z \sim 3$ and elliptical galaxies at $z \sim 0.1$ with a strong Balmer break will produce the same colors in $u - g$. Therefore, there is a degeneracy in the color-redshift space and the PDF of such population has often two peaks (one at $z \sim 0.1$ and another at $z \sim 3$). Such a degeneracy could be solved by adding new NIR data, or by introducing a prior.

We did such work for the CFHTLS following exactly the same approach as Benítez (2000). The Bayesian approach allows us to introduce a relevant *a priory* information in the PDF. We introduced the redshift distribution as a prior:

$$p(z, T|i'_{AB}) = p(T|i'_{AB})p(z|T, i'_{AB}) \tag{2.5}$$

with $p(z|T, i'_{AB})$ is the redshift distribution for galaxies with spectral type T and magnitude i'_{AB}. $p(z|T, i'_{AB})$ is parametrized as:

$$p(z|T, i'_{AB}) \propto z^{\alpha_t} exp\left(-\left[\frac{z}{z_{0t} + k_{mt}(i'_{AB} - 20)}\right]^{\alpha_t}\right), \tag{2.6}$$

where α_t, z_{0t}, k_{mt} are free parameters and t denotes the type dependency. $p(T|i'_{AB})$ is the spectral type distribution, parametrised as:

$$p(T|i'_{AB}) = f_t e^{-k_t(i'_{AB}-20)}. \tag{2.7}$$

where f_t is the fraction of each type at $i'_{AB} = 20$ and k_t is a free parameter. Since the VVDS spectroscopic sample is a simple I- selected sample and because the VVDS targets are randomly selected, it is appropriate to use the VVDS spectroscopic sample to compute this prior. Therefore, we fit the values of the free parameters using the VVDS redshift distribution. The parameters used for the prior are listed in the Table.2 of Ilbert et al. (2006) and included in *Le_Phare* . Such a prior has been successful to reduce the fraction of catastrophic failures from 5.5% to 3.8% in the CFHTLS-D1 field for a $I_{AB} < 24$ population in Ilbert et al. (2006).

While the redshift distribution is often introduced as a prior, other external knowledge could be introduced. For instance, Mobasher et al. (2007) introduced a prior on the luminosity function. More recently, new codes are tested including prior on the mass-SFR relation (Tanaka et al. 2015). However, such a priory knowledge limits the science which can be carry on later. For instance, if the luminosity function is included as a prior, such a photo-z sample should not be used to estimate the luminosity function later.

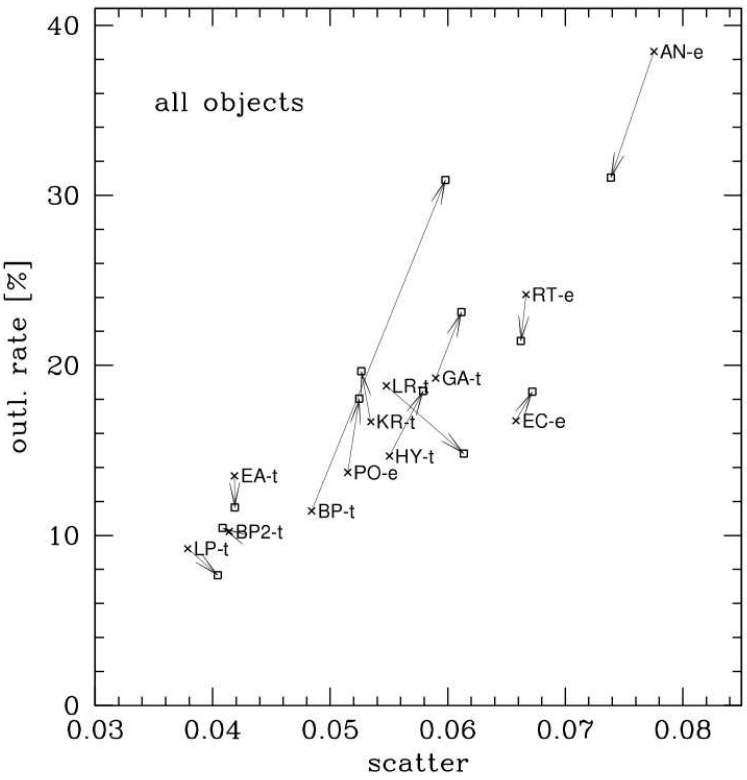

Figure 2.5: Comparison between the results of various codes used in the PHAT experiment (Hildebrandt et al. 2012). The codes indicated as "-e" and "-t" correspond to empirical and template-fitting codes, respectively. The code *Le_Phare* is indicated as LP-t and the configuration is exactly the same as in Ilbert et al. (2009).

2.2.7 Convergence toward a unified template-fitting method ?

Numerous template-fitting codes are now available to compute the photometric redshifts: HyperZ (Bolzonella et al. 2000), BPZ (Benítez 2000), ZEBRA (Feldmann et al. 2006), EAZY (Brammer et al. 2008), *Le_Phare* (Arnouts et al. 2002, Ilbert et al. 2006). While not public, numerous other codes exist and are also widely used: e.g. Rainbow (Barro et al. 2011), GOODZ (Dahlen et al. 2010) zphot (Giallongo et al. 1998), or ImpZ (Babbedge et al. 2004). This list is far from being exhaustive and new codes are developed in preparation of future surveys (new photo-z codes are currently developed for the PanSTARRs survey, the Hyper Suprime-Cam survey or the Euclid mission). Because of the number of codes, it is important to assess if some procedures (e.g. calibration of the zero-points) are necessary to produce better results. Even if the codes are still different, we need to understand if we should converge toward one unified version of the template-fitting code, or a list of the best "practices" in the photo-z computation depending on the scientific objectives and the properties of the considered dataset.

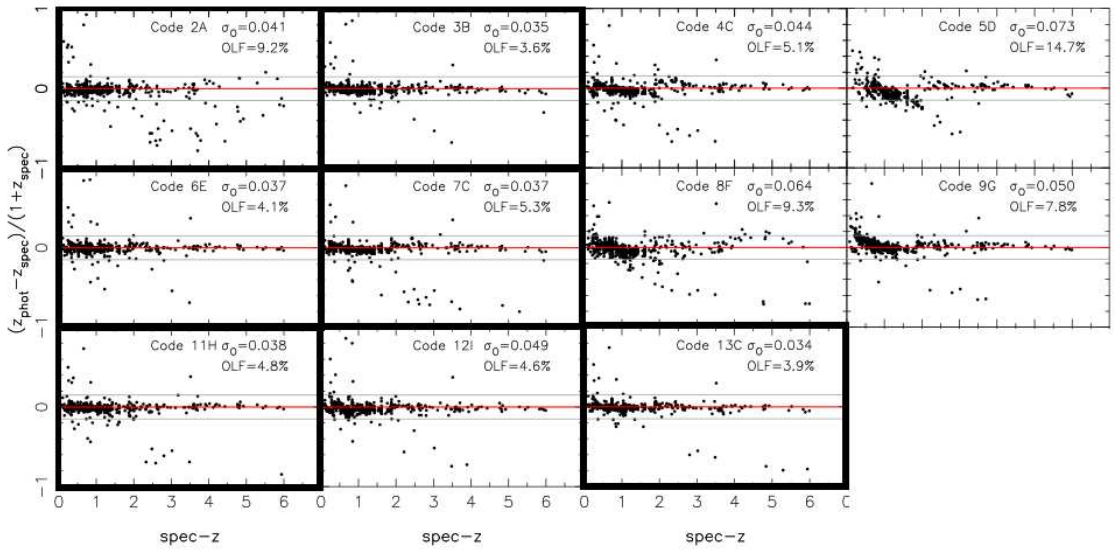

Figure 2.6: Comparison between the results of various codes used in the CANDELS experiment (Dahlen et al. 2013). The *Le_Phare* code corresponds to the number 11 and has been run by M. Salvato using exactly the same configuration as in Ilbert et al. (2009).

The PHAT experiment was designed in 2007 during a workshop in Vancouver "Weak lensing and Photometric Redshifts". It was decided that a blind comparison between various codes on the same dataset will be experimented. We use the imaging dataset obtained on GOODS-North and the photometric catalogue was prepared by Capak et al. (2004). Only a subsample of spec-z were provided to the community and the organizers kept half of the spec-z to check blindly the quality of the photo-z. Twelve persons ran their codes on the GOODS-N catalogue and the results were analyzed by Hildebrandt et al. (2010). The main result from Hildebrandt et al. (2010) is shown in Fig.2.5. All the codes indicated as "-e" are empirical codes using a training sample to estimate the photo-z. All the codes indicated as "-t" are template-fitting based codes. A clear result from the PHAT experiment is that template-fitting codes perform much better than empirical methods in the high-z Universe. While this conclusion could change if large and representative training set were obtained in deep surveys, the use of template-fitting method is still favored to study the intermediate and high redshift Universe (but see Sánchez et al. 2014 for the Dark Energy Survey). The situation is inverted in the local Universe when the SDSS spectroscopic sample is available for the training.

The same experiment was repeated by the CANDELS team. The photometric catalogue was generated with the TFIT method (Laidler et al. 2007) on the GOODS-S field. Again, only a fraction of the spectroscopic redshifts were distributed to the participants. In this case, only template-fitting methods have been compared by Dahlen et al. (2013). The results are shown in Fig.2.6. The codes using some calibration of the zero-points are indicated with black rectangles. It appears clearly that a calibration of the zero-points is

necessary to limit possible biases. It appears even more clearly when the run 4C and 13C are compared: photo-z are computed with EAZY following a similar procedure, but code 4C is not calibrating the zero-points.

So, best practice are diffusing through the template-fitting codes. One of the conclusions of Dahlen et al. (2013) is that "codes producing the lowest scatter and outlier fraction utilize a training sample to optimize photometric redshifts by adding zero-point offsets, template adjusting, or adding extra smoothing errors.". It seems also clear now that the code including emission lines in their templates perform better, in particular at $z > 4$ (Schaerer D. & de Barros S., 2012) and when medium bands are used (Ilbert et al. 2009). Still, important discrepencies are still present between the various codes: 1) BPZ and EAZY do not allow additional dust attenuation to their templates while Le Phare and Hyperz do; 2) all these codes use a different set of templates and no concensus has been reached (e.g. large BC03 library for Hyperz or few templates extracted from a SAM which can be combined in EAZY).

2.3 The COSMOS Photometric redshifts

This section is mainly focused on the COSMOS photometric redshifts which are currently the most precise and accurate photo-z over such a large redshift range $0.2 < z < 6$. We extensively used these photo-z to study the galaxy evolution. For instance, we studied the stellar mass assembly (e.g. Drory et al. 2009, Ilbert et al. 2010, Ilbert et al. 2013), the evolution of infrared galaxies (e.g. Le Floc'h et al. 2009, Kartaltepe et al. 2010, Béthermin et al. 2012, Heinis et al. 2013, Gruppioni et al. 2013), the evolution of the sSFR with radio data (Karim et al. 2011), the AGN evolution (e.g. Donley et al.2012), the large-scale structure (Scoville et al. 2013), the groups (George et al. 2011), the evolution of the mass-to-light ratio (Leauthaud et al. 2012) or the merger rate (López-Sanjuan et al. 2012). The scientific analysis described in this manuscript (chapters 3, 4, 5) are based on these photometric redshifts. The precision of these photo-z relies on an incredible dataset, with deep-broad and medium-bands imaging from the Subaru Telescope, deep ground-based NIR data from the UltraVISTA survey, and IRAC data. While this survey is almost unique in term of multi-λ coverage (the only other field with a similar coverage is GOOD-S, Cardamone et al. 2010), it is the only survey which can propose this coverage for 600,000 galaxies at $i' < 26$ over 2 deg^2. Moreover, it is the only field in which we can test the photo-z with such a rich spectroscopic sample.

2.3.1 The COSMOS coverage

Ultraviolet: Very deep u^* band data were obtained at the 3.6m Canada-France Hawaii Telescope (CFHT) using the Megacam camera (Boulade et al. 2003). The u^* band data were processed at the TERAPIX data reduction center[3]. The u^* band data cover the

[3]terapix.iap.fr

entire COSMOS field and reach a depth of $u^* \sim 26.5$ mag for a point source detected at 5σ. The u^* band images are also used as priors in the measurement of FUV (1500Å) and NUV (2300Å) fluxes in order to ensure a proper deblending of sources in the GALEX images (Zamojski et al. 2007). GALEX fluxes are then extracted using the EM-algorithm (Guillaume et al. 2006). They reach a depth of $FUV \sim 26$ mag and $NUV \sim 25.7$ mag.
Optical: The COSMOS-20 survey (Taniguchi et al. 2015) entailed 30 nights of observation at the Subaru 8.2m telescope using the Suprime-Cam instrument. The observations are complete in 20 bands: 6 broad bands (B_J, V_J, g^+, r^+, i^+, z^+), 12 medium bands ($IA427$, $IA464$, $IA484$, $IA505$, $IA527$, $IA574$, $IA624$, $IA679$, $IA709$, $IA738$, $IA767$, $IA827$) and 2 narrow bands ($NB711$, $NB816$). We restricted our study to the area covered by the deep optical Subaru image (2-deg^2, $149.4114 < \alpha < 150.8269$ and $1.4987 < \delta < 2.9127$) in order to assure a robust photo-z estimate.
2009 near-infrared coverage: In 2009, the full 2-deg^2 COSMOS field was covered with deep J, H and K band data obtained using the WFCAM and WIRCAM wide-field infrared cameras on UKIRT and CFHT, respectively. The NIR data reduction is detailed in McCracken et al. (2010). The data reach $J \sim 23.7$ mag and $K \sim 23.7$ mag for a point source detected at 5σ.
2012 near-infrared coverage with UltraVISTA: In 2012, the COSMOS field was covered with deep NIR data obtained with the VIRCAM camera (Emerson & Sutherland 2010) on the VISTA telescope as part of the UltraVISTA project. All four UltraVISTA bands are used: Y, J, H, K_s; the depths for the UltraVISTA DR1 are given in Table 1 of McCracken et al. (2012) and the imaging cover 1.5 deg^2.
2007 mid-infrared coverage with S-COSMOS: deep IRAC data were taken during the *Spitzer* cycle 2 S-COSMOS survey (Sanders et al. 2007). A total of 166 hr were dedicated to cover the full 2-deg^2 with the IRAC camera in 4 bands: 3.6μm, 4.5μm, 5.6μm and 8.0μm. Source detection is based on the $3.6\mu m$ image and the fluxes were measured in the four IRAC bands using the "dual mode" configuration of SExtractor. The IRAC catalogue is 50% complete at $1\mu Jy$ at $3.6\mu m$ ($m_{3.6\mu m} \sim 23.9$ mag). Data reduction and catalogue extraction is described in Ilbert et al. (2010). We also got a new proposal accepted to increase the depth of our dataset. The SPLASH survey (PI: P. Capak) is an ongoing survey of 1250h with IRAC to cover the full COSMOS field. The survey will reach a magnitude limit of $0.3\mu Jy$, which is three times deeper than the S-COSMOS data.

2.3.2 Two multi-color catalogues

The i-band selected catalogue v2.0 from Capak et al. (2007)

All the imaging data were combined to generate a master photometry catalogue (Capak et al. 2007). The first catalogue was created by Capak et al. (2007) and this catalogue has continuously improved by adding new dataset. We are currently using the version v2.0 of this catalogue including the medium-band data from Subaru and the UltraVISTA data which were not existing in 2007. Still, the method to generate the catalogue remains

the same. Photometry was performed using SExtractor in dual mode (Bertin & Arnouts 1996). Source detection was run on the deepest image ($i^+ \sim 26.2$ for a point source detected at 5σ). For the UV-NIR data, the Point Spread Function (PSF) varies from 0.5" to 1.5" from the K to the $u*$ images. In order to obtain accurate colors, all the images were degraded to the same PSF of 1.5" following the method described in Capak et al. (2007). The final photometric catalogue contains PSF matched photometry for all the bands from the u^* to the K band, measured over an aperture of 3" diameter at the position of the i^+ band detection.

For the FUV and NUV *GALEX* data, the catalogue is provided in total flux obtained by a PSF fitting procedure (Zamojski et al. 2007). The IRAC fluxes were measured in a circular aperture of radius 1.9" and converted to a total flux using aperture corrections. We rescaled all the optical aperture magnitudes with a common factor ($auto\_offset = i^+_{AUTO} - i^+_{APER}$ from the Capak et al. 2007 catalogue), in order to make it coherent with the total fluxes available for GALEX and IRAC.

Finally, all magnitudes are corrected for galactic extinction estimated for each object individually, using dust map images from Schlegel et al. (1998). Poor image quality areas (e.g. field boundary, saturated stars, satellite tracks and image defects) are masked. Photo-z are computed only in the non-masked regions with a total covered area of 1.73-deg^2. 126 071, 293 627 and 607 617 sources are detected at $i^+ < 24$, $i^+ < 25$ and $i^+ < 26$. This catalogue is available at the following link *irsa.ipac.caltech.edu/data/COSMOS/*.

The NIR-selected catalogue from McCracken et al. (2012)

In 2012, we also used a complementary photometric catalogue produced by McCracken et al. (2012). In this catalogue, the detection image is the chi-squared sum of the (non-convolved) UltraVISTA DR1 $YJHK_s$ images, following the techniques outlined in Szalay et al. (1999). This catalogue counts 339384 sources with 220000 galaxies at $K_s < 24$ over clean areas. This ensures that all sources detected in at least one VISTA band are included in the final catalog. We use this catalogue in order to create mass limited samples at $z > 1$ since numerous sources may not be detected in optical (and then these sources will be missed in the Capak et al. catalogue). The method to generate this catalogue is almost the same as Capak et al. (2007). The main difference is that the images were degraded to the same PSF of 1.1", rather than 1.5" (because we decided to drop the g^+ band from our analysis).

This catalogue is available at the following link *http://terapix.iap.fr/article.php?id_article=844*.

2.3.3 Photometric redshifts for galaxies

Method

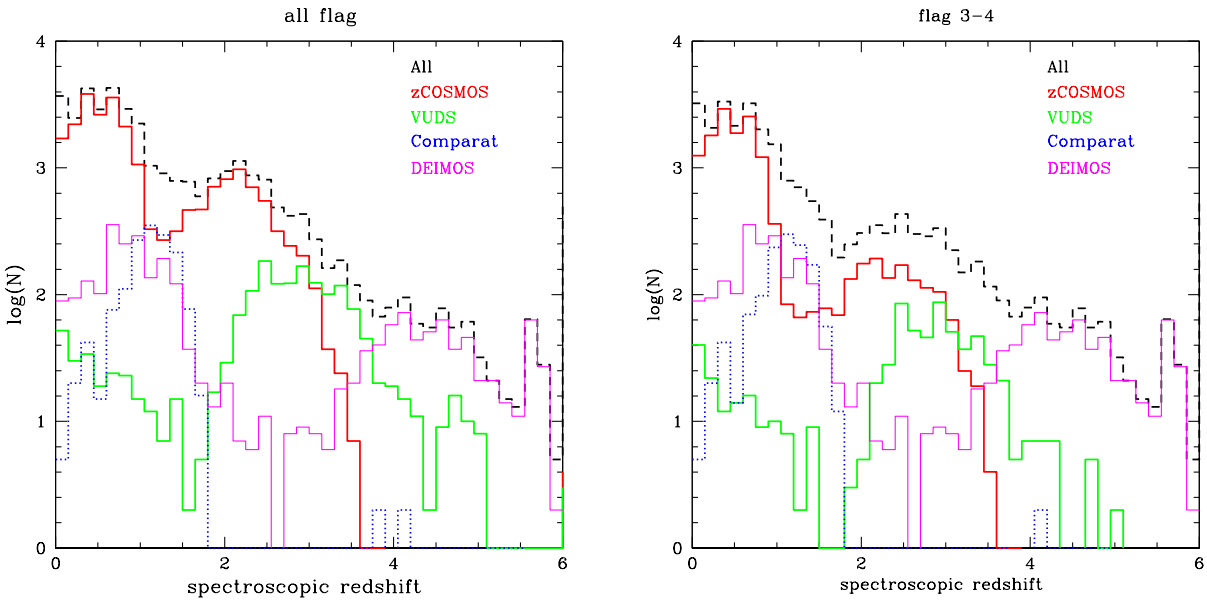

Figure 2.7: Spectroscopic redshift distributions for various samples taken on the COSMOS field. The left panel includes all flags while the right panel includes only the most secured redshift ($> 97\%$ confidence level).

The photometric redshifts are derived using "Le Phare" (Arnouts et al. 2002, Ilbert et al. 2006) with a χ^2 template-fitting method (see Section 2.2.1). Ilbert et al. (2009) used 31 templates including elliptical and spiral galaxies from the Polletta et al. (2006) library and 12 templates of young and blue star-forming galaxies generated with BC03 (see section 2.2.3). As explained in section 2.2.4, extinction is added as a free parameter (E(B-V)<0.5) and several extinction laws are considered (Calzetti et al. 2000, Prevot 1984 and a modified version of the Calzetti laws including a bump at 2175Å). Emission lines are added to the templates using an empirical relation between the UV light and the emission line fluxes (see section 2.2.5). Finally, we calibrate automatically the zero-points following the method described in section 2.2.2 using zCosmos spectroscopic redshifts.

Using a spectroscopic sample of quiescent galaxies, Onodera et al. (2012) showed that the estimate of the photo-z for the quiescent galaxies in the i^+-selected photo-z catalogue v2.0 were underestimated at $1.5 < z < 2$. In Ilbert et al. (2013), i.e. for the K_s selected catalogue, we improve the photo-z for this specific population by adding two new BC03 templates assuming an exponentially declining SFR with a short timescale $\tau = 0.3Gyr$.

Spectroscopic redshifts

The COSMOS survey benefits of an extensive spectroscopic follow-up. These spectroscopic samples are a key ingredient to provide well tested and robust photo-z. We list below the various surveys:

A representative bright sample at $z < 1.2$: the zCOSMOS bright survey (Lilly et al. 2007) include 20700 galaxies selected at $i^+ \leq 22.5$. zCOSMOS-bright galaxies were observed using the red grism of VIMOS covering a wavelength range $5500\text{Å} < \lambda < 9000\text{Å}$ at a resolution of 600 (MR grism).

A sample of bright star-forming at $0.7 < z < 1.5$: we used 1503 FORS2/VLT redshifts at $0.6 < z < 1.8$ (Comparat et al., 2015). This sample has been selected in color and target emission lines galaxies with really short exposures (20 min) with FORS2 at VLT.

A sample of bright star-forming at $1.4 < z < 1.8$: 138 FMOS/Subaru redshifts at $1.4 < z < 1.8$ (Silverman et al., 2015).

A large sample of faint star-forming at $1.5 < z < 2.5$: zCOSMOS-faint includes approximately 9500 galaxies color-selected to lie in the redshift range $1.5 \lesssim z \lesssim 3$ (Lilly et al., in preparation). Galaxies are selected by color based either on the *BzK* criterion (Daddi et al. 2004) or the *UGR* "BM" and "BX" criterion of Steidel et al. (2004), and the magnitude cut was $B_J < 24 - 25$ (depending on the color cut). Observations were carried out with the blue grism of VIMOS ($3600\text{Å} < \lambda < 6800\text{Å}$) at a resolution of 200.

A large sample of faint star-forming at $2.7 < z < 4$: we got 1638 redshifts with the VIMOS Ultra Deep Survey (VUDS, Le Fèvre et al. 2015). The VUDS survey targets $z > 2.7$ galaxies, being as inclusive as possible. Observations were done using both the blue and red grism of VIMOS with a total exposure times of 40h per spectra. In this chapter, we use a VUDS preliminary sample.

A sample of faint star-forming at $0.2 < z < 6$: we also got 2553 spectroscopic redshifts with DEIMOS at Keck II. This sample combines several selected sub-populations of blue star-forming and infrared galaxies at $0.5 < z < 6$ (Kartaltepe et al., in preparation) and really high redshift sources (Capak et al., in preparation). The DEIMOS spectra cover a wavelength range $4000\text{Å} < \lambda < 9000\text{Å}$ at a resolution of 600.

A faint sample of quiescent galaxies at $1.5 < z < 2.6$: 18 faint quiescent galaxies at $z < 1.9$ obtained with MOIRCS/Subaru (Onodera et al. 2012) and 16 faint quiescent galaxies at $1.85 < z < 2.6$ obtained with the WFC3 grism observations from the 3D-HST survey (Krogager et al., 2013).

Comparison between photo-z and spec-z

We first assess the quality of the photo-z by comparison with the spec-z. This comparison is necessary to characterize the quality of the photo-z, and possible biases in the photo-z estimate. Such a comparison is limited to the most secure spectroscopic redshifts, i.e. the spec-z with a confidence level > 97%. Therefore, the uncertainties in the spec-z are neglected and the spec-z are used as a reference to assess the quality of the photo-z. We emphasize that the photo-z are tested only in the magnitude/redshift/type range surveyed by the spectroscopic sample. Therefore, it is important to gather a spectroscopic sample as representative as possible.

We estimate the precision of the photo-z using the normalized median absolute deviation (NMAD: Hoaglin et al. 1983) defined as $1.48 \times \text{median}(|z_p - z_s|/(1 + z_s))$. The

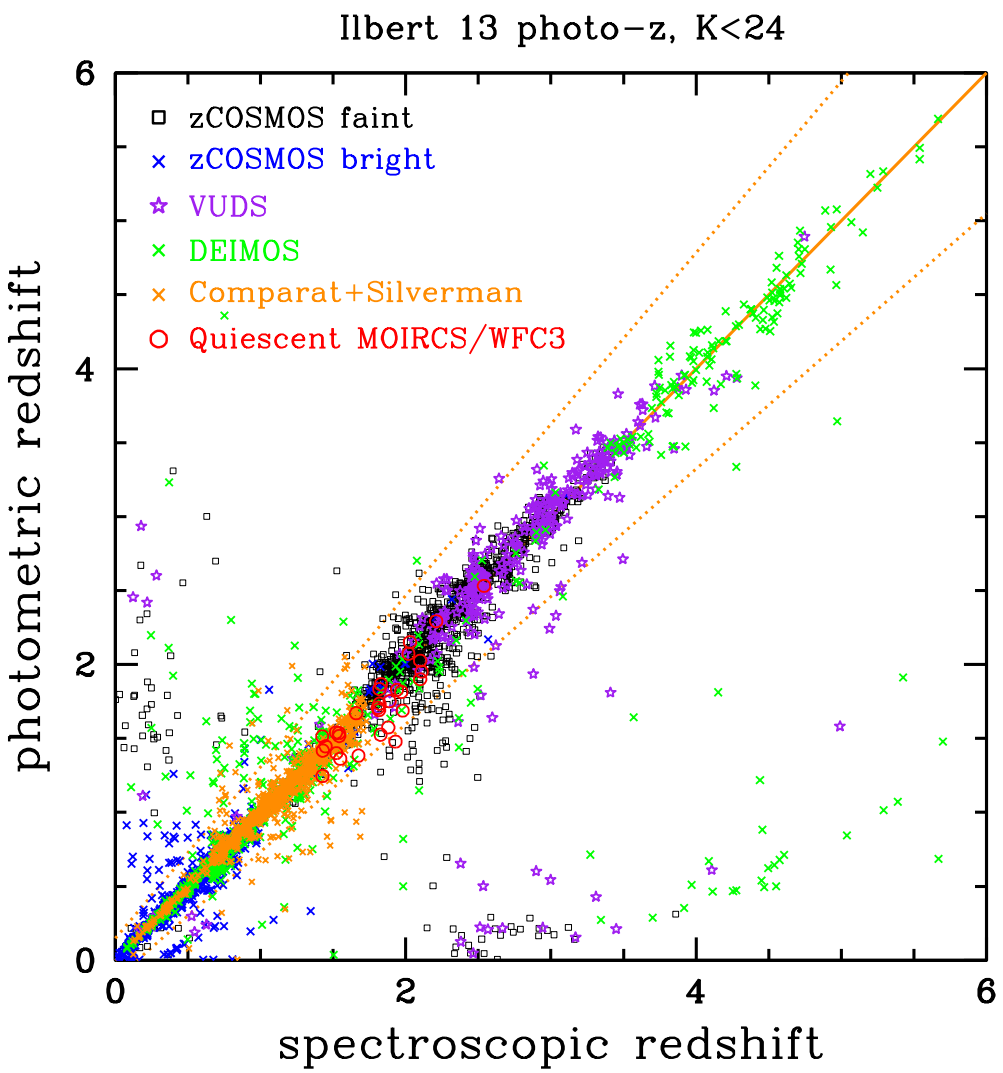

Figure 2.8: Comparison between z_p and z_s for a $K < 24$ selected sample. These photo-z are based on the NIR selected catalogue by McCracken et al. (2012). The dotted and dashed lines are for $z_p = z_s \pm 0.15(1 + z_s)$ and $z_p = z_s \pm 0.05(1 + z_s)$, respectively.

NMAD is directly comparable to other papers which directly quote the $rms/(1 + z)$. This dispersion estimate is robust with respect to catastrophic errors, i.e. objects with $|z_p - z_s|/(1 + z_s) > 0.15$. The percentage of catastrophic errors is denoted by η.

Figure 2.8 shows the comparison between z_p and z_s for the K_s-selected sample from Ilbert et al. (2013), which is the UltraVISTA based catalogue. Table 2.2 list the precision and the fraction of catastrophic failures as a function of the considered spectroscopic sample. The median redshift and magnitude for each sample are also given. For the zCosmos bright sample at $i^+ < 22.5$ (blue points), the precision and the fraction of catastrophic failures stay below 1%. For the zCOSMOS faint and VUDS samples, which cover the

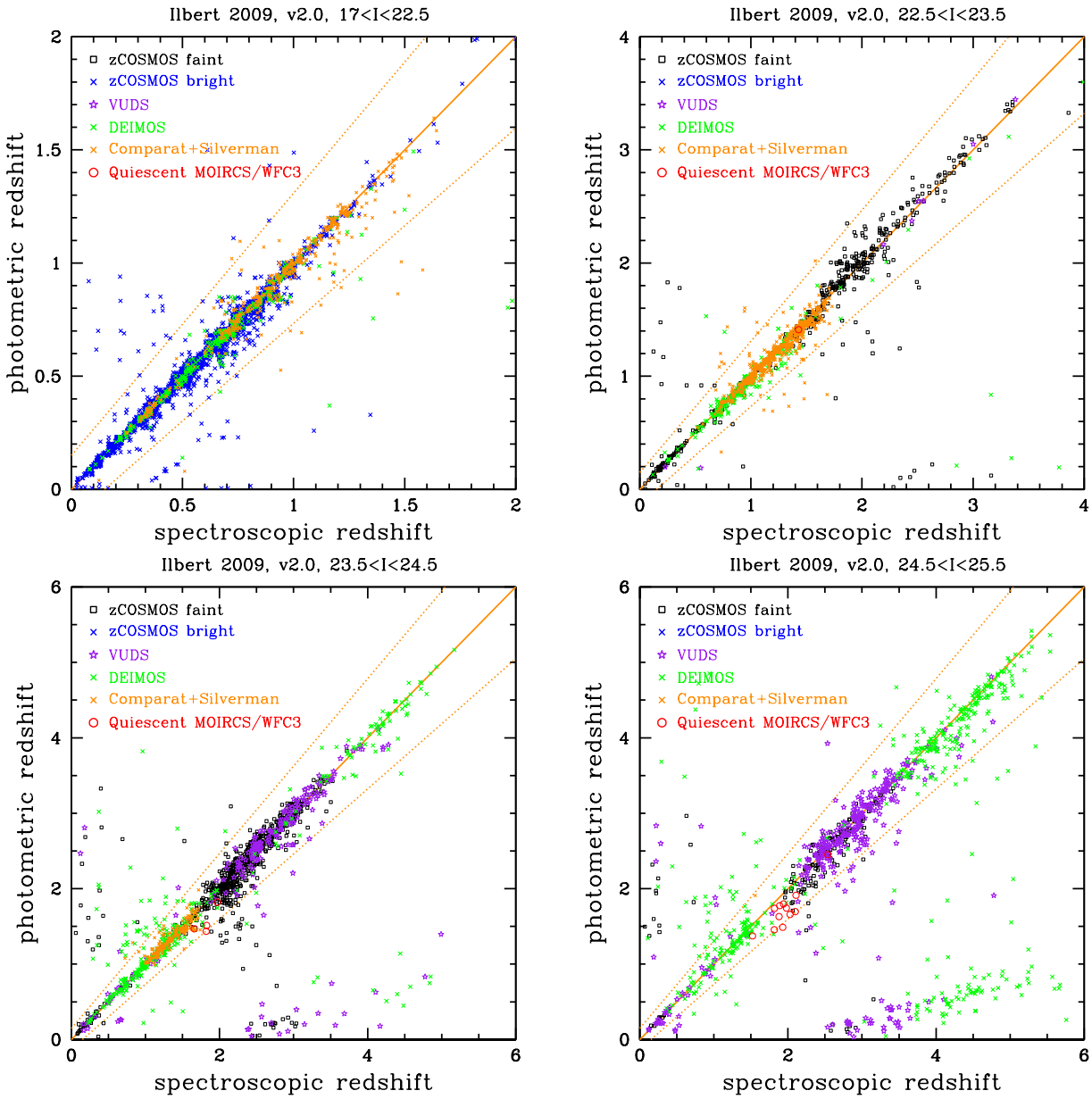

Figure 2.9: Comparison between z_p and z_s as a function of the apparent magnitude for the photo-z based on updated i^+-selected catalogue from Capak et al. (2007). We do not impose any selection criteria in NIR.

$1.7 < z < 3.5$ redshift range, we got a fraction of catastrophic failure below 10% and a precision around $0.03 - 0.04(1 + z)$.

Figure 2.9 shows the comparison between z_p and z_s for the i^+-selected sample from Ilbert et al. (2009) updated at the version 2.0 (including the UltraVISTA data). Each panel corresponds to a different apparent magnitude bin, going from an $i^+ \sim 22$ to an

spectroscopic survey	Nb spec-z $K_s < 24$	z_{med}	I_{med}	$\sigma_{\Delta z/(1+z)}$	$\eta(\%)$
zCOSMOS bright	9389	0.50	21.4	0.0080	0.5
Kartaltepe 2013	548	0.73	22.0	0.0105	3.3
Comparat 2013	1105	1.14	22.7	0.0133	2.9
Capak 2013	631	1.15	23.5	0.0213	9.5
Onodera 2012	17	1.55	23.9	0.0446	0.0
Silverman 2013	97	1.58	23.2	0.0265	2.1
Krogager 2013	13	2.02	24.8	0.0708	7.7
zCOSMOS faint	1392	2.15	23.6	0.0297	7.6
VUDS	327	2.75	24.3	0.0360	9.8

Table 2.2: Characteristics of the spectroscopic redshift samples and photometric redshift precision. Only the most secure spectroscopic redshifts at $K_s < 24$ are considered. The photo-z are the ones from Ilbert et al. (2013) based on the NIR selected catalogue of McCracken et al. (2012). The median redshift and magnitude are provided for each sample.

spectroscopic survey	Nb spec-z $i^+ < 25$	z_{med}	I_{med}	$\sigma_{\Delta z/(1+z)}$	$\eta(\%)$
zCOSMOS bright	8616	0.52	21.5	0.0081	0.5
Kartaltepe 2013	526	0.74	22.2	0.0116	3.6
Comparat 2013	1160	1.16	22.8	0.0147	2.3
Capak 2013	922	1.25	23.9	0.0223	11.2
Onodera 2012	15	1.65	24.5	0.0938	0.0
Silverman 2013	97	1.58	23.2	0.0265	2.1
Krogager 2013	11	1.98	25.0	0.0904	9.1
zCOSMOS faint	1522	2.15	23.8	0.0261	6.6
VUDS	459	2.75	24.5	0.0388	16.1

Table 2.3: Same as Table 2.2 for a sample selected at $i^+ < 25$. The photo-z are an updated version from Ilbert et al. (2009) based on the i^+-selected catalogue v2.0 from Capak et al. (2007). The sources are not necessarily detected in NIR.

$i^+ \sim 25$ sample. Table 2.3 list the precision and the fraction of catastrophic failures as a function of the considered spectroscopic sample and Table 2.4 provides the statistics for the full sample split per apparent magnitude bin. As expected, the precision and the fraction of failure is degraded going to fainter samples. For a galaxy having an apparent magnitude at $i^+ \sim 25$, the precision is still reaching $0.05(1+z)$ but the fraction of failure

spectroscopic survey	Nb spec-z	z_{med}	I_{med}	$\sigma_{\Delta z/(1+z)}$	$\eta(\%)$
$17.0 < i^+ < 22.5$	9489	0.53	21.5	0.0083	0.6
$22.5 < i^+ < 23.5$	1585	1.19	23.0	0.0173	3.5
$23.5 < i^+ < 24.5$	1581	2.15	24.0	0.0291	8.6
$24.5 < i^+ < 25.5$	963	2.90	24.9	0.0471	21.5
$25.5 < i^+ < 27.0$	274	4.11	26.0	0.4033	62.0

Table 2.4: Same as Table 2.2. All the spectroscopic samples are combined and split per apparent magnitude bin. The photo-z are an updated version from Ilbert et al. (2009) based on the i^+-selected catalogue v2.0 from Capak et al. (2007).

reaches 20%.

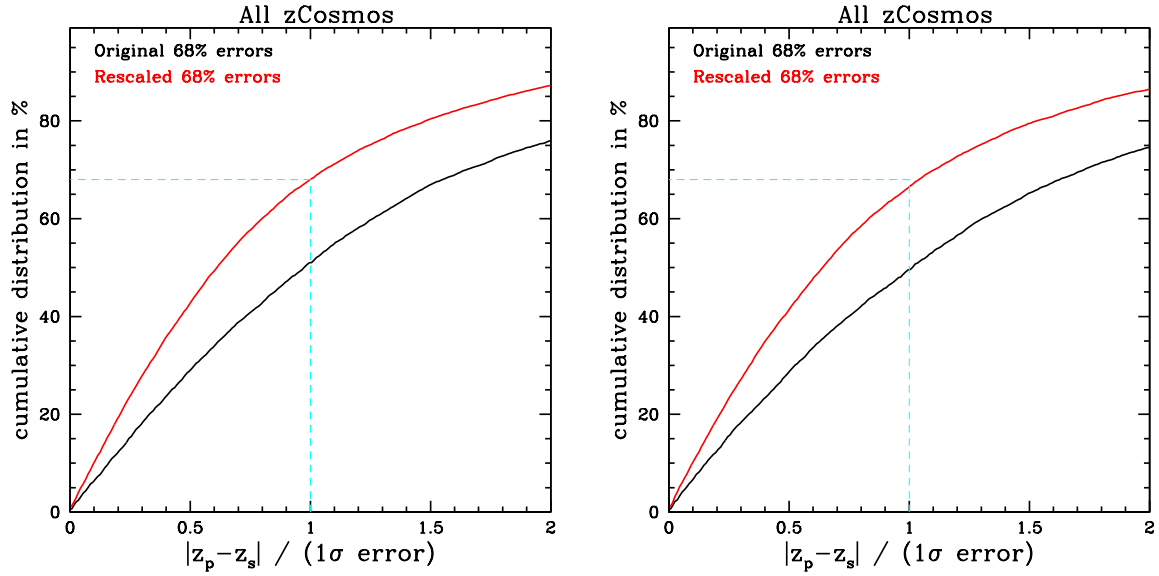

Figure 2.10: Cumulative distribution of the ratio $|z_p - z_s|/(1\sigma$ error) for the i^+-selected sample (left) and the K_s-selected sample (right).

Accuracy derived from the photo-z Probability Distribution Function

The evaluation of the photo-z quality from the comparison with spec-z is limited to specific ranges of magnitude and redshift. We use the 1σ uncertainty derived from the photo-z Probability Distribution Function (PDF) to extend our analysis over the full magnitude/redshift space.

The reliability of the 1σ uncertainty needs to be validated. Figure 2.10 shows the cumulative distribution of the difference $z_p - z_s$ normalized by the 1σ photo-z error in the

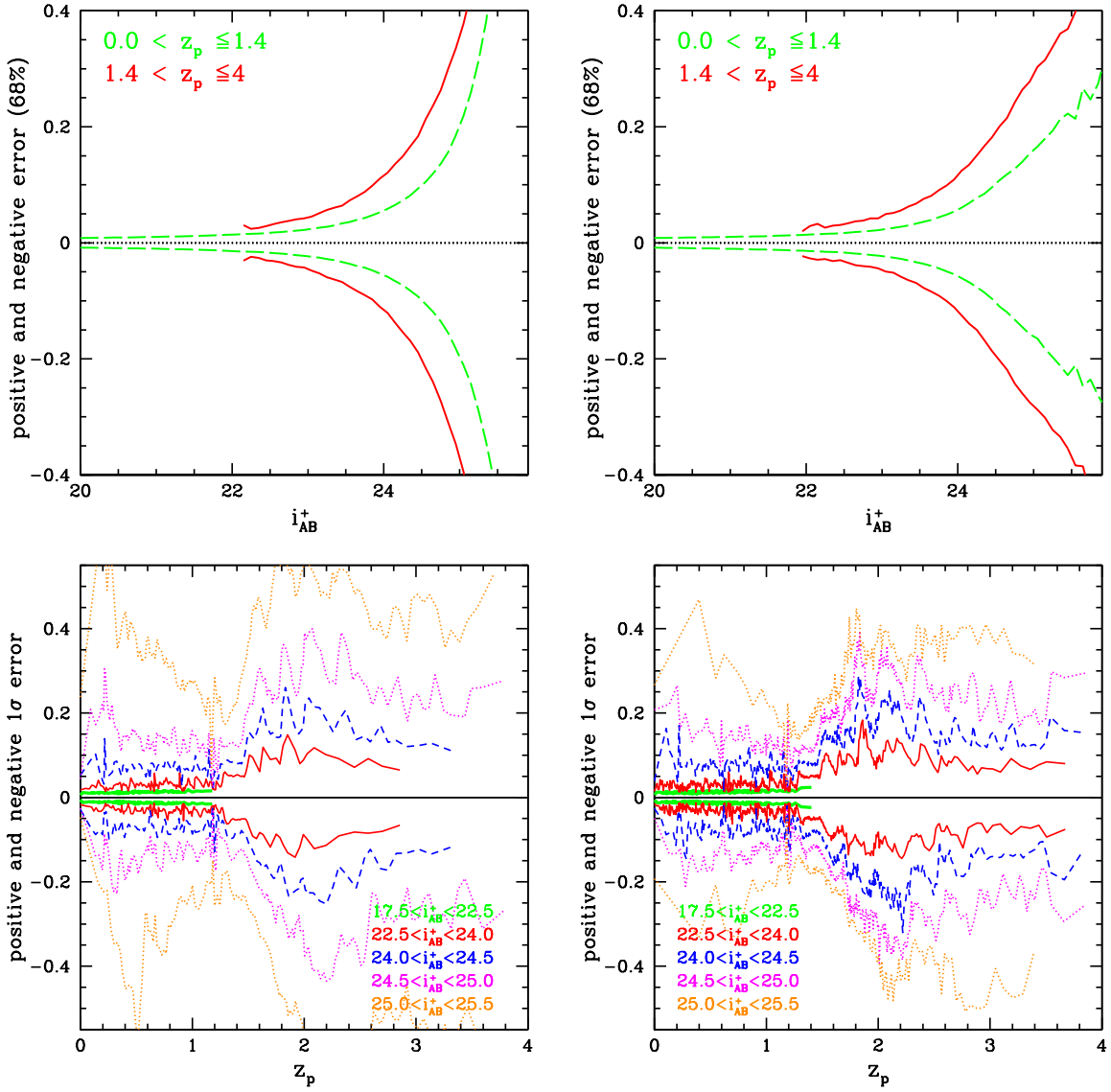

Figure 2.11: *Top panels*: 1σ uncertainty for the z_p estimate as a function of magnitude for the i-band selected sample on the left (Capak et al. 2007, Ilbert et al. 2009) and the NIR selected sample on the right (McCracken et al. 2012, Ilbert et al. 2013). *Bottom panels*: 1σ uncertainty for the z_p estimate as a function of redshift in different apparent magnitude bin.

zCOSMOS sample. The ratio $|z_p - z_s|/(1\sigma\ error)$ is lower than 1 if the measured offset $z_p - z_s$ is lower than the 1σ uncertainty, which should be the case for 68% of our galaxy sample. We find that the 1σ uncertainties are underestimated (black line). We need to multiply the errors by a factor f depending on the apparent magnitude in order to obtain

the right uncertainties on the photo-z. We use $f = 0.25 * i^+ - 3.8$ if $i^+ > 20$ (and 1.2 if $i^+ < 20$).

Figure 2.11 shows the 1σ negative and positive errors as a function of magnitude in the top panels and as a function of redshift in the bottom panels. Three clear conclusions emerge:

- the precision is inevitably degraded for fainter galaxies at all redshifts (top panels of Fig.2.11);
- photo-z have significantly higher uncertainties at $z \gtrsim 1.4$;
- the uncertainties are lower for the K_s-selected sample, in particular at $z \sim 2$ for faint galaxies in optical.

For the i^+-selected sample, the 1σ errors do not depend significantly on the redshift at $z < 1.4$, with $\sigma_{\Delta z} \lesssim 0.02$ at $i^+ < 24$ (note that we dropped out the division of σ by $(1+z)$ in this analysis). But the precision is significantly degraded between $i^+ = 25$ ($\sigma_{\Delta z} \lesssim 0.2$ and $i^+ = 25.5$ ($\sigma_{\Delta z} \lesssim 0.4$). To first order, the photo-z are precise when the λ position of the Balmer and/or Lyman breaks is well constrained. The Balmer break is observed at $\lambda < 9000$Å as long as $z < 1.4$ which corresponds to the best wavelength sampling with the medium bands.

The precision is degraded at $z > 1.4$, since the Balmer break is redshifted out of the medium band coverage. When a detection in K_s band is imposed ($K_s < 24$ in the right figure), the precision at $z \sim 2$ is improved, even for the extremely faint optical sample $i^+ > 25$.

2.3.4 Photometric redshifts for AGN

In Salvato, Hasinger, Ilbert et al. (2009) and Salvato, Ilbert, Hasinger et al. (2011), we developed new methods to estimate the photometric redshifts of X-ray selected sources.

In Salvato et al. (2009), the X-ray sources were selected using the XMM coverage of the COSMOS field. The optical and X-ray cross-identification was performed using a likelihood method described in Brusua et al. (2007). Over 1542 XMM-COSMOS sources, we identified 1032 sources best fit by a template with an AGN contribution. The reliability of the photometric redshifts is evaluated using a subsample of 442 sources with measured spectroscopic redshifts. For this population, we reach a precision of $\sigma_{\Delta z/(1+z_s)} = 0.011$, almost equivalent of our result for the galaxies, but with a larger outlier fraction of 6.3%.

In Salvato et al. (2011), we released a new catalogue including 1692 Chandra-detected sources and 1735 XMM-detected sources in the COSMOS field (869 sources are common to both surveys). The Chandra survey covers the central 0.9 deg^2 in the COSMOS field, three time deeper than XMM-COSMOS.

Several factors explain that we can reach such a precision in the photo-z for X-ray sources:

- *the number of bands*. Table 4 of Salvato et al. (2009) shows that it is crucial to use medium bands data to reach such a precision: without the medium band data, the precision is degraded at 0.06 and the fraction of outliers reaches 20%. The medium band coverage provides a sampling of the broad emission lines allowing us to well constrain the positions of spectral features.

- *correction for variability* is an important step which reduces by two the fraction of catastrophic failures. Multi-epoch observations have been used to correct for variability. We applied a correction for variability by rescaling the optical photometry to a common epoch.

- *the method* has also been improved. A new set of SEDs was developed by combining the SEDs of normal galaxies from Ilbert et al. (2009) with AGN contribution at various level. The new set of templates include 18 hybrids SEDs which mimic different contributions of AGNs and of their host galaxies. Also, depending on the X-ray luminosity of the source and its morphology, a choice is done on the template library which is the best suitable (AGN and hybrid templates or galaxies template from I09).

To conclude, we developed a method which allows us to obtain 1% accurate photometric redshifts for the galaxies in the COSMOS field thanks to the medium band data. We produced two catalogues: one i^+-selected catalogue (Ilbert et al. 2009) and one NIR selected catalogue (Ilbert et al. 2013). The results of this manuscript are based on these catalogues. However, the dataset of COSMOS is continuously evolving. In particular, new IRAC data are currently obtained with the SPLASH survey (PI: P. Capak). We also observed this field with extremely deep optical data taken with the Hyper SuprimeCam camera (HSC, PI: G. Hasinger). Therefore, we are continuously updating our photometric and photo-z catalogues. C. Laigle (PhD student at IAP supervised by H.J. McCracken) is currently preparing a new version of this catalogue which should be a reference for the following years. Still, the photo-z method used for the new catalogue will be the same as the one described in this chapter.

Chapter 3

Global star formation history

As described in the introduction, numerous physical processes enter into the regulation of the star formation. These physical processes act on different timescales, mass ranges and environments. Observational constraints are necessary to establish the relative importance of the numerous physical processes impacting the star formation. We provide such observables in the chapters 3, 4, 5. In this chapter, we establish the global star formation history (SFH) from $z \sim 0.1$ to $z \sim 4$ using statistical measurements performed in the COSMOS field.

Measuring the cosmic SFRD is one of the most basic and important measurement in observational cosmology. Since the first two seminal papers of Madau et al. (1996) and Lilly et al. (1996), it has become an industry to trace the evolution of the cosmic SFR Density [1] (see Table 4 of Behroozi et al. 2013 for a recent list of papers). The SFRD as a function of redshift characterizes how the averaged instantaneous SFR evolves along the age of the Universe. Almost all the cosmological models, semi-analytical or hydrodynamical, use this observable as a reference for their validation (e.g. Somerville et al. 2008, Lu et al. 2011, Bower et al. 2012, Behroozi et al. 2013, Torrey et al. 2014, Henriques et al. 2015). Indeed, being able to reproduce this observable is a necessary step to demonstrate that the simulation implements correctly the various physical processes, from the growth of the DM structures to the efficiency in converting the gas into stars.

Still, such a measurement is far from being straightforward. Such a study relies on the ability to measure an accurate SFR which is challenging. Several tracers allow us to estimate the SFR of a galaxy and I will list the most relevant ones in a first section. Such a study relies also on our capacity to measure the SFR for representative sample of galaxies, in order to establish the SFRD. I will shortly review some recent results that we obtained using UV, IR and radio tracers. While numerous results are continuously published, I will restrict myself to the ones in which I contributed, often based on the COSMOS data presented earlier.

[1] SFRD - stellar mass created per year and per comoving volume unit

A complementary approach to study the global star formation history has emerged in the last 10 years. By measuring the stellar mass density [2] - noted ρ_* - we can estimate the total mass of stars created along cosmic time for a given galaxy population. The evolution of the SFRD and of the stellar mass density provides two complementary probes of the SFH: one instantaneous and one integrated picture. We produce an estimate of the SFH, that we discuss in section 3.3 based on our analysis of the UltraVISTA stellar mass density (Ilbert et al. 2013). Still, our estimate relies on our capacity to estimate the stellar mass using galaxy SED modeling. I will explain this technique and its limits.

3.1 Measuring the galaxy properties

3.1.1 Stellar masses

In the last 10 years, stellar population synthesis (SPS) models have been extensively used to convert luminosity into stellar mass (e.g. Bell et al. 2003, Fontana et al. 2004). The starting point of these models is a Simple Stellar Population (SSP) describing the emissivity of one stellar population across time (given an initial mass function, a metallicity). Then, by assuming a given star formation history, composite models are created by combining the SSPs. One difficulty in these models is to implement the isochrone libraries which determine the evolution of a single stellar population (Conroy 2013). Moreover, depending on the models, several layers of complexity are added, like the treatment of the dust attenuation (Silva et al. 1998) or the inclusion of nebular emission lines (Schaerer et al. 2012). In practice, the user generates his own library of models with different assumptions on the SFH, metallicity, etc. These modelized SEDs are normalized at one solar mass and are fit over the multi-color data through a template-fitting procedure. The recent reviews of Walcher et al. (2011) and Conroy (2013) described these various aspects.

In this work, we use the SED templates generated with the stellar population synthesis package developed by Bruzual & Charlot (2003). We assume a universal IMF from Chabrier (2003) and an exponentially declining star formation history $\mathrm{SFR} \propto e^{-t/\tau}$ (τ in the range 0.1 Gyr to 30 Gyr). The SEDs are generated for a grid of 51 ages (in the range 0.1 Gyr to 14.5 Gyr). Dust extinction is applied to the templates using the Calzetti et al. (2000) law and $E(B-V)$ in the range $[0-0.5]$. We use models with three different metallicities (solar and sub-solar).

The resulting stellar masses are highly model dependent. In Ilbert et al. (2010), we quantify how the various hypothesis on the model affect our results. In Fig.3.1, this comparison is updated using the UltraVISTA data in the COSMOS field. I use two spectroscopic samples: the zCOSMOS bright (left panels) and faint (right panels) spectroscopic samples, selected at $i^+_{AB} < 22.5$ and at $z \sim 2$, respectively (Lilly et al. 2009, see section 2.3.3).

[2] total stellar mass per comoving volume unit

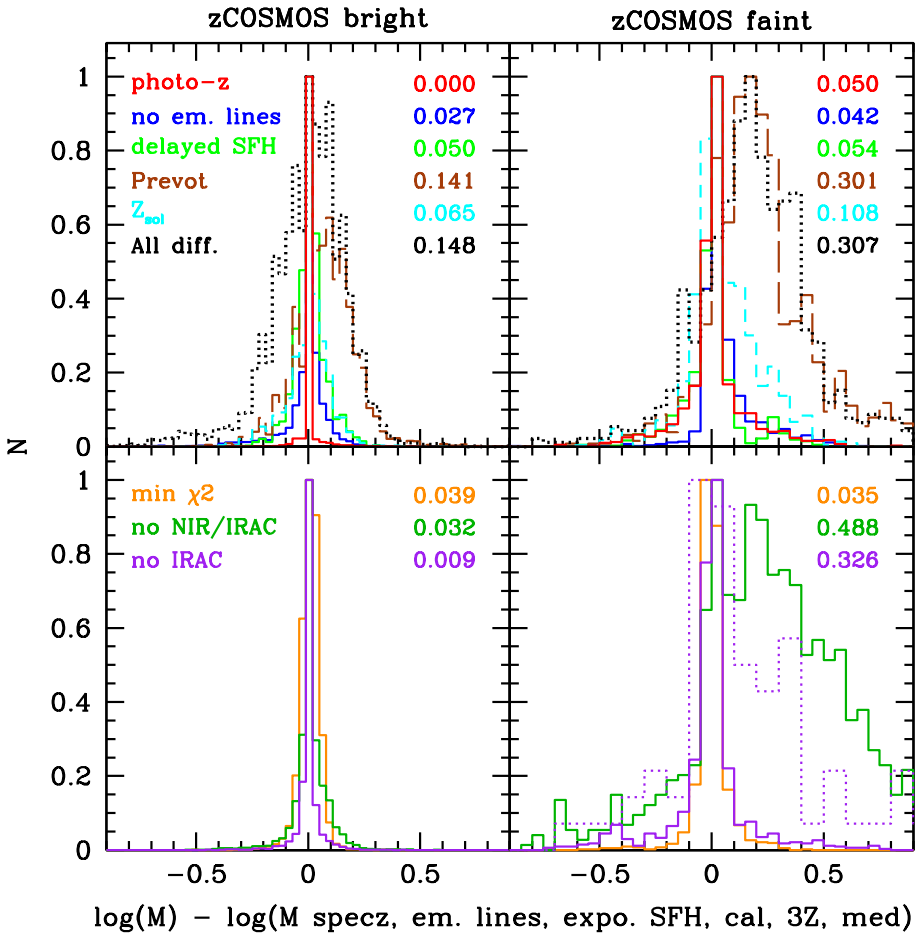

Figure 3.1: Comparison between the stellar masses computed by varying some hypothesis in the modeled BC03 templates and the reference stellar masses (computed using spectroscopic redshifts with all bands, including emission lines in the templates, assuming an exponentially declining SFH, assuming the Calzetti extinction law, 3 metallicities, and using the median of the PDF to get the mass). The left and right panels correspond to the tests done on the zCOSMOS bright ($i_{AB} < 22.5$) and faint samples ($z \sim 2$), respectively. For each test, we change only one ingredient compared to the reference mass: photo-z rather than spec-z (red), no emission lines (blue), delayed SFH rather than exponentially declining (green), use the Prevot extinction law rather than the Calzetti one (brown), use only the solar metallicity rather then 3 metallicities (cyan). We also test the worse case scenario in which all assumptions are different: photo-z, no emission lines, delayed SFH, the Prevot extinction law, one solar metallicities, minimum χ^2 (black). In the bottom panel, we show the impact of removing the IRAC bands (purple, dotted at $z > 4$) and the UltraVISTA+IRAC bands (dark green). The orange line compared the masses obtained with the median of the PDF and the minimum χ^2. We indicate the median difference in the top right part of each panel.

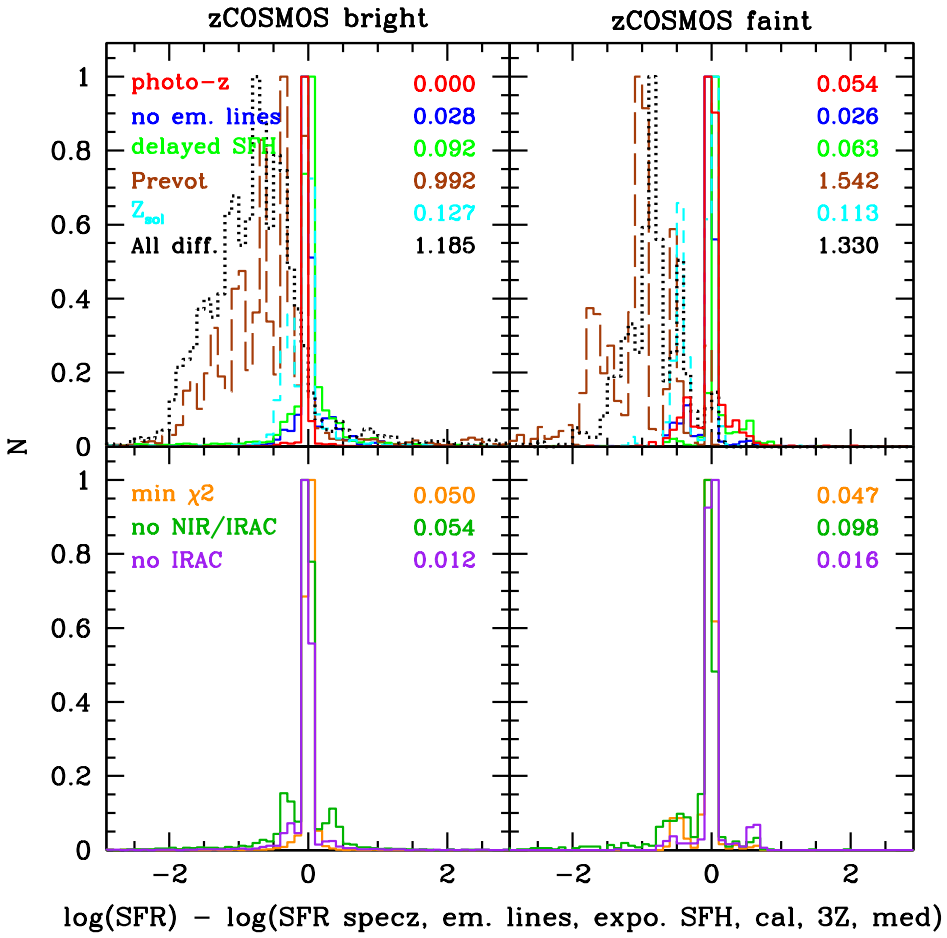

Figure 3.2: Same as Figure 3.1 but testing the SFR rather than the stellar mass.

Impact of photo-z uncertainties out to $z \sim 4$

The red histogram of Fig.3.1 shows the difference between the stellar masses computed with photometric and spectroscopic redshifts. At $z < 1$, the uncertainties on the photo-z do not affect the stellar mass estimate. At $z \sim 2$, the dispersion reaches ~ 0.05 dex. If we simply use the masses measured at the minimum χ^2 rather than the median of the PDF, we create an uncertainty at the same level. In the COSMOS case, the photo-z are not the dominant source of uncertainties.

Impact of different assumptions in the modeled SEDs

We tested the impact of several assumptions in the model: using only the solar metallicity rather than three (cyan), using delayed SFHs rather than exponentially declining ones (green), removing the emission lines from the templates (blue), assuming a SMC extinction curves (Prevot) rather than the Calzetti one. While changing the various

assumptions has a low impact on the zCOSMOS bright sample ($z < 1.2$, $i_{AB} < 22.5$), we introduce uncertainties reaching a factor 2 at $z \sim 2$. The choice of the extinction law is the largest source of uncertainty in the stellar mass estimate. We did not test here the choice of SPS model. Several papers (e.g. Pozzetti et al. 2007, Ilbert et al. 2010) show that using Maraston (2005) or Charlot & Bruzual (2007) rather than BC03 create systematic differences of 0.13-0.15 dex because of the different treatment of the TP-AGB stars.

Impact of the available bands

It is usually considered as crucial to sample the rest-frame optical part of the galaxy SEDs in order to obtain accurate stellar masses. We test this claim by removing the NIR and IRAC bands when we measure the stellar masses. The impact on zCOSMOS bright is limited since the z^+-band is still sampling a rest-frame range at $\lambda > 4000$Å. But when no NIR/IRAC data are available at $z \sim 2$, we see that the dispersion reaches 0.7 dex with significant biases reaching 0.3 dex. Removing IRAC only has a limited impact at $z \sim 2$, while we find that IRAC is crucial at $z > 4$ (dotted purple line in the bottom right panel).

3.1.2 Star formation rate

The most direct method to estimate the global SFH is to sum the instantaneous SFR of all the galaxies in a given comoving volume. Several tracers could measure the SFR of a galaxy, each of them having strengths and weaknesses:

- **the UV tracer.** The massive O-B stars dominate the UV emissivity. Because these stars are short-lived (from few to 100 millions years), the UV-light is a good tracer of the SFR. UV rest-frame light is straightforward to observe at $z > 1$ with the current instrumentation since this light is redshifted in optical or NIR. But a large fraction of the emitted UV light ($> 90\%$ for the most actively star-forming galaxies) is absorbed by dust. The amount of light absorbed by dust depends on the galaxy geometry, the past SFH, the orientation of the galaxy, etc. Correcting the UV light from the dust attenuation is extremely complex and subject to high uncertainties. Several methods based on the UV slope of the continuum (β-slope from Meurer et al. 1999) exist but they introduce uncertainties much larger than 0.2 dex in the SFR estimate.

- **SED-fitting with optical data.** We can use stellar population synthesis (SPS) models created by assuming different SFH, as described in section 3.1.1. This method is really unstable at $z > 1$ (more than 0.3 dex of dispersion, possible biases) and is highly impacted by the assumptions done in the SED modeling. In Fig.3.2, we perform exactly the same tests as for the stellar mass. The estimate of the SFR using SED fitting is much more unstable than the estimate of the stellar mass. In particular, if we use the SMC extinction law rather than the Calzetti one, we create an offset by more than a factor 10, even at low redshift.

- **the NRK method (Arnouts et al. 2013).** An empirical estimate of the SFR has been established using the M(NUV), M(R) and M(K) absolute magnitudes. The relation has been calibrated in the COSMOS field using the MIPS $24\mu m$ fluxes as a reference for the SFR. For the moment, such a relation has been established only at $z < 1.2$. Such a method produces a SFR which is accurate at 0.1-0.2 dex but subject to some bias below a sSFR of $10^{-10} yr^{-1}$.

- **the infrared tracer.** Part of the infrared emission results from the UV light emitted by the massive stars, absorbed and reprocessed by the dust. The peak of the IR emissivity occurs around $\lambda \sim 100\mu m$ rest-frame, depending on the dust temperature. By adding the UV and the IR light, we obtain an accurate estimate of the SFR. By having Herschel data covering a wavelength range from 100 to $500\mu m$, the SFR is estimated with an uncertainty lower than 0.1 dex. Unfortunately, the IR light can be measured only for galaxies forming more than $100\mathcal{M}_{\odot}/yr$ at $z > 2$ even with the deepest Herschel data (Fig.4 of Elbaz et al. 2011).

- **the radio tracer.** The radio emission is explained by synchrotron radiations triggered by supernovae. This emission is not affected by dust along the line of sight. However, the emission could come from the AGN component of the galaxies. Only a small fraction of sources are directly detected into the radio maps. Therefore, such studies using radio data require to use stacking methods.

- **the nebular emission lines.** The Hα emission line (656.3nm) is considered as one of the best SFR tracers, emitted by HII regions ionized by young and massive stars (Tresse et al. 2002). But the Hα line is redshifted into the NIR at $z > 1$. Such a method required large samples of spectra taken in NIR which is difficult with current instrumentation. At $z > 3$, one needs to rely on [OII] emission line (372.7nm) which is not a good tracer of the SFR since the relation between [OII] and the SFR depends on the metallicity and is more sensitive to dust extinction.

This list of SFR tracers is not exhaustive. For instance, SN or Gamma-ray bursts can be used as SFR tracers (Robertson & Ellis 2013). An extensive literature describes how to convert the galaxy emissivity into SFR, as the review of Kennicutt (1998) (see Kennicutt & Evans 2012 for an updated review).

3.2 Star formation history from instantaneous tracers

Since the first seminal papers (Lilly et al. 1996, Madau et al. 1996), the SFRD evolution has been re-investigated using numerous SFR tracers and on a large redshift range. Recently, Madau & Dickinson (2014) compiled numerous SFRD results from UV to IR.

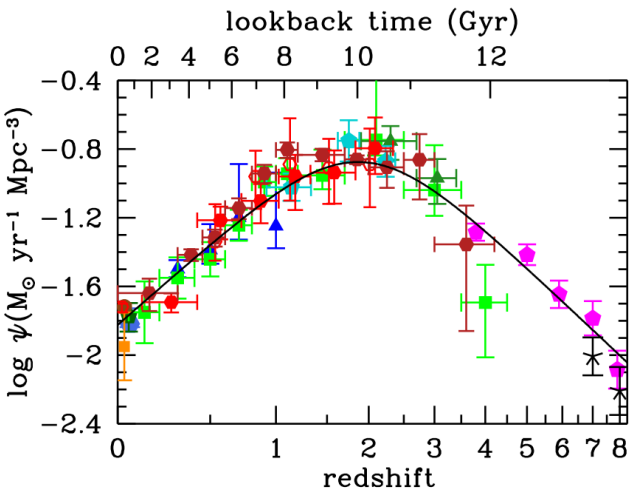

Figure 3.3: Figure 9 from Madau & Dickinson (2014) showing a recent SFRD compilation. The red and dark red symbols correspond to the IR measurements from Gruppioni et al. (2013) and Magnelli et al. (2013), respectively. The blue triangles, the green squares and the magenta pentagons correspond to the UV measurements from Schiminovich et al. (2005), Cucciati et al. (2012), and Bouwens et al. (2012), respectively.

They confirm the "bell" shape of the SFH with a peak around $z \sim 2$. Madau & Dickinson (2014) find the following parametrisation of the SFH, as shown in Fig.3.3:

$$\Phi(z) = 0.015 \frac{(1+z)^{2.7}}{1+[(1+z)/2.9]^{5.6}} \mathcal{M}_{\odot} yr^{-1} Mpc^{-3} \tag{3.1}$$

By comparing the famous SFRD compilation by Hopkins et al. (2006) with the most recent ones by Behroozi et al. (2013) and Madau & Dickinson (2014), it is clear that the SFH obtained by compiling previous results from the literature have changed significantly at $1.5 < z < 6$ in the last 10 years, as shown in Fig.3.4 (right panel). The position of the SFRD peak has shifted toward lower value and the maximum value of the SFRD has been divided by a factor 2 between the compilations of Hopkins et al. (2006) and Madau & Dickinson (2014).

Figure 3.4 shows recent SFRD measurements using UV tracers corrected for dust extinction (Cucciati et al. 2012), IR tracers (Gruppioni et al. 2013), and radio tracers (Karim et al. 2011). Both the radio and the IR analysis are based on the same parent sample from Ilbert et al. (2010), i.e., a $m_{3.6\mu m} < 24$ selected sample associated with the COSMOS photo-z described in chapter 2. Gruppioni et al. (2013) is based on IR tracers of the SFR, combining the far-IR data sets from the PACS Evolutionary Probe (PEP) Survey (at 70, 100 and 160μm) and from the Herschel Multi-tiered Extragalactic Survey data (at 250, 350 and 500μm). The COSMOS data are combined with other deep surveys to derive the IR luminosity functions out to $z = 4$. The analysis by Karim et al. (2011) is also based on the same 3.6μm selected sample: the sources are split per stellar mass bin

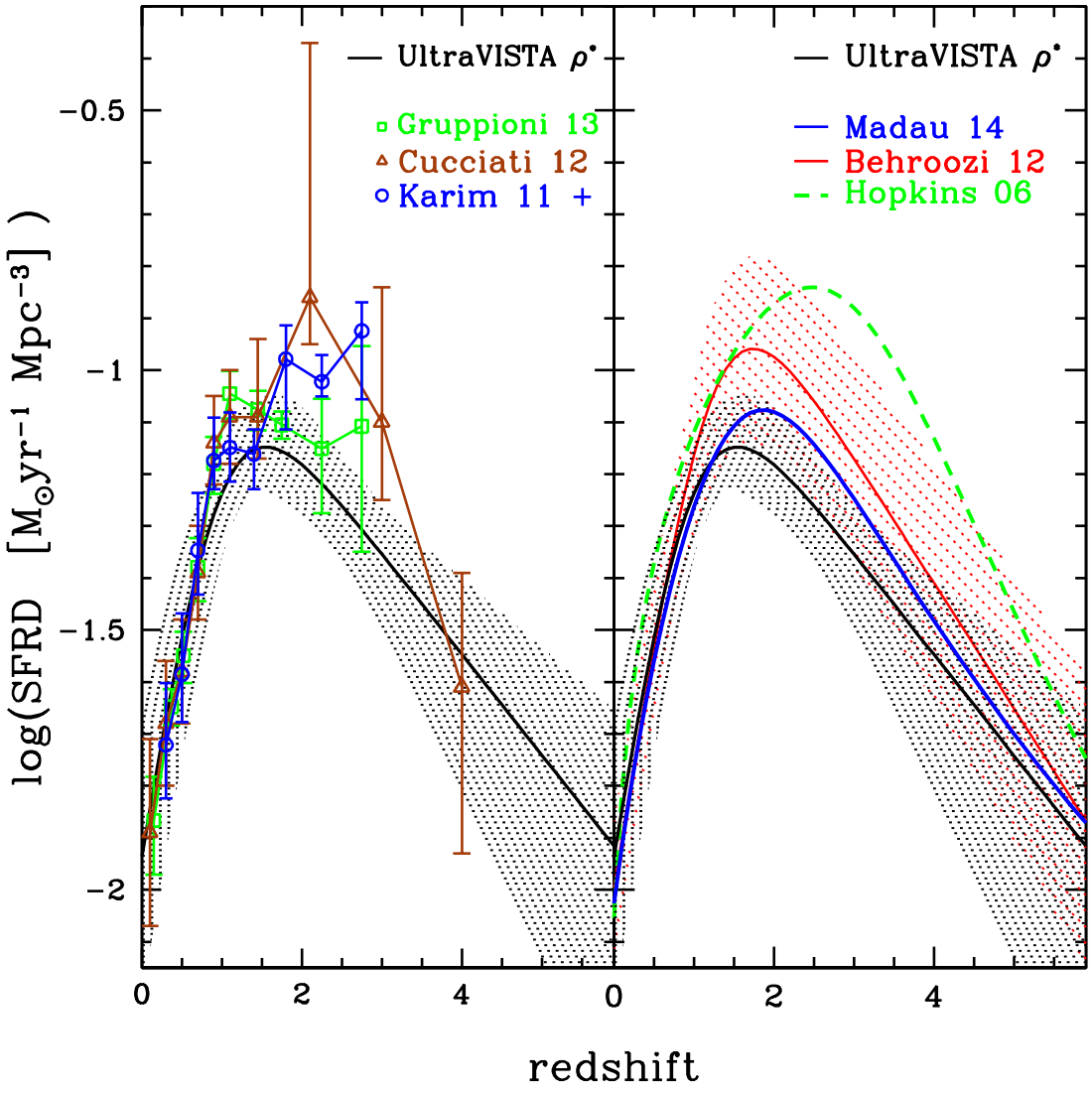

Figure 3.4: **Left:** a comparison between the star formation history inferred from the UltraVISTA mass density (black solid line and dashed area corresponding to 1σ errors) and direct measurements of the SFRD from UV (Cucciati et al. 2012, brown triangles), IR (Gruppioni et al. 2013, green squares) and radio (Karim et al. 2011 using updated GSMF, blue circles). **Right:** comparison between the SFH derived from the UltraVISTA mass density and SFRD compilation by Hopkins et al. (2006) (green dashed lines), by Behroozi et al. (2013) (red solid line with dashed lines for the associated uncertainties) and by Madau & Dickinson (2014) (blue solid lines).

and are stacked in the radio map to produce the median SFR at a given mass. The total SFRD is obtained by combining the GSMF (Ilbert et al. 2010) and the $\mathcal{M}_\star$-SFR relation at a given mass.

These studies confirm early results from Lilly et al. (1996) and Madau et al. (1996) showing a continuous increase in the SFRD from the local Universe up to $z \sim 1.5$. As shown in Fig.3.4, the agreement between the various tracers is impressive at $z < 1$ and we find an evolution by a factor $\sim 6-7$ between $z \sim 0.1$ and $z \sim 1.5$. However, we are far from converging to a precise measurement of the SFRD at the peak of the star formation activity. Depending on the tracer, the SFRD varies by 0.3 dex at $1.5 < z < 3$. While the SFRD based on the IR tracer shows a continuous decrease between $z = 1$ to $z = 3$, the radio SFRD shows on the contrary a continuous increase. However, both analysis have their pros and cons. The IR analysis is limited to bright IR sources (ULIRG at $z > 2$, even in the GOOD-S field). Therefore, Gruppioni et al. (2013) cannot constrain the slope of the IR LF, and even the value of Φ^* could be affected since we cannot sample galaxies fainter than L^*. Therefore, this estimate relies on the extrapolation for faint galaxies. Numerous uncertainties could affect the radio measurement by Karim et al. (2011): the stacking procedure; the contribution of the AGN; the difficulty to convert the radio emissivity into SFR, the knowledge of the GSMF, ...

In Figure 3.4, I also added the analysis of Cucciati et al. (2012) using the UV as SFR tracer. The study is based on the spectroscopic redshifts of the VVDS deep ($I < 24$) and Ultra-Deep ($i^* < 24.75$) surveys. But even with the deepest spectroscopic sample up to date, the slope of the Schechter function is extremely challenging to constrain at $z > 1.5$. The steep value of the slope used by Cucciati et al. (2012) at $1.7 < z < 2.5$ explained the high value of the SFRD at $z \sim 2$. However, this slope was not directly measured and α was set based on previous studies. Moreover, the UV light is corrected for dust using the SED-fitting procedure which could be affected by large uncertainties.

While these analysis represent the state of art in SFRD measurements, we see variations reaching 0.3 dex at $z > 1.5$. We can not determine which study is the most robust. Therefore, we conclude that uncertainties at the order of 0.3 dex are still present at the peak of the SFRD.

The situation at $z > 3-4$ is even more complex. The compilation of SFRD changed significantly between Hopkins et al. (2006) and Madau & Dickinson (2014) because of the new SFRD estimates at $3 < z < 7-8$. Indeed, a large number of studies in the last few years have secured their LBG candidates at $z > 3$ thanks to the deep NIR images obtained with the WFC3/HST camera. These new data have allowed a better treatment of the dust attenuation using the β slope (e.g. Bouwens et al. 2012). A common impression in the community is that the SFRD measurements at $z > 3$ are converging. Still, we need to remember that all the studies are based on a UV tracer, and that the selection of the targets are often based on the same imaging data with similar selection criteria. The contribution of the low SFR galaxies is extremely difficult to constrain, even at $z \sim 4$. Moreover the correction of the dust attenuation with the β slope could introduce large uncertainties. Unfortunately, it is not yet possible to measure SFRD at $z > 3-4$ with robust IR or emission lines tracers for a representative sample of star-forming galaxies. Correcting the UV light from dust absorption is extremely challenging and uncertain, in particular for massive star-forming systems (Heinis et al. 2013). The impact of dust

extinction could be lower at $z > 4$, as shown in Cucciati et al (2010) and Bouwens et al. (2012). However, extreme star-forming galaxies with most of their light emitted in IR are still discovered at $z > 5$ (e.g. Capak et al. 2011), showing that a population of powerful IR galaxies is already present in the young Universe.

3.3 Star formation history derived from the stellar mass census

In this section, we use the evolution of the galaxy stellar mass density ρ_* along cosmic time to characterize the SFH out to $z = 4$. Since the mass density ρ_* characterizes the stellar mass already created, its evolution provides an integrated view of the SFH which is complementary to the use of instantaneous SFR tracer.

Our study is based on the UltraVISTA NIR selected catalogue and the associated photometric redshifts described in section 2.3. We built mass selected samples with 220,000 galaxies selected at $K_s < 24$ over 1.52 deg^2. The measurement of the stellar masses relies on SED fitting and we analyzed the robustness of such a method in section 3.1.1. After having show the GSMF in section 3.3.1, we will follow the method of Wilkins et al. (2008) to trace the SFH in section 3.3.2.

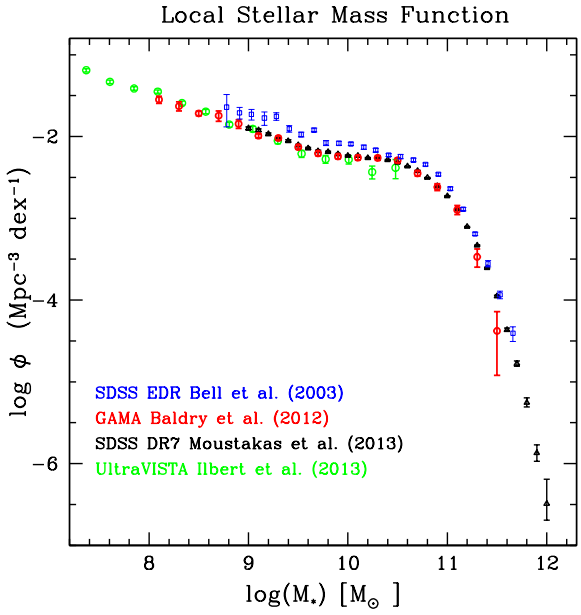

Figure 3.5: Local stellar mass function, including the local one from UltraVISTA (in green).

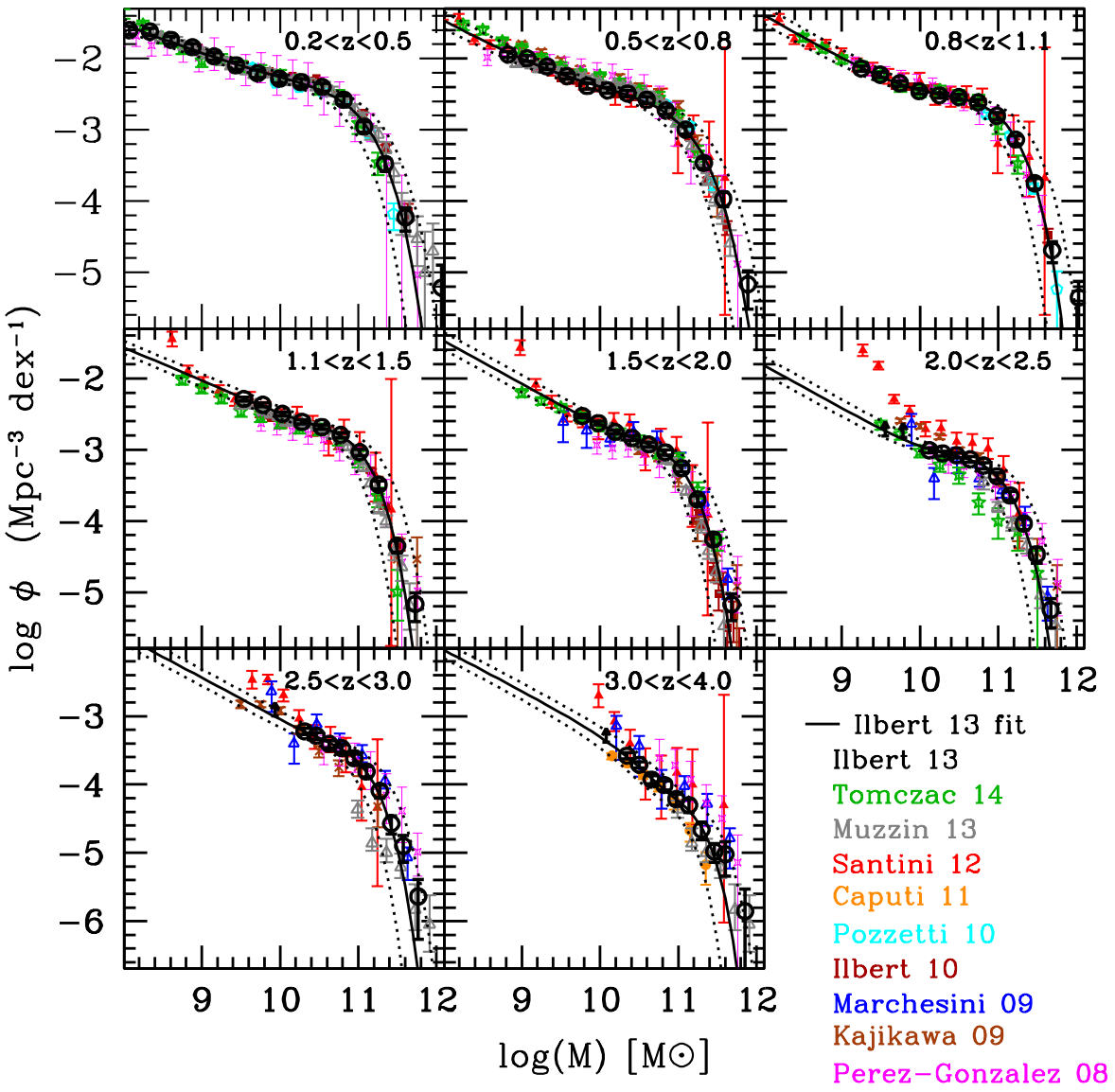

Figure 3.6: UltraVISTA global stellar mass functions (open black circles and solid lines) compared with several measurements from the literature published since 2008 (labeled in the bottom right). Each panel corresponds to a redshift bin. The literature GSMF measurements are converted to the same cosmology and IMF as used in this study (H_0 = 70 km s^{-1} Mpc^{-1} and Chabrier 2003 IMF).

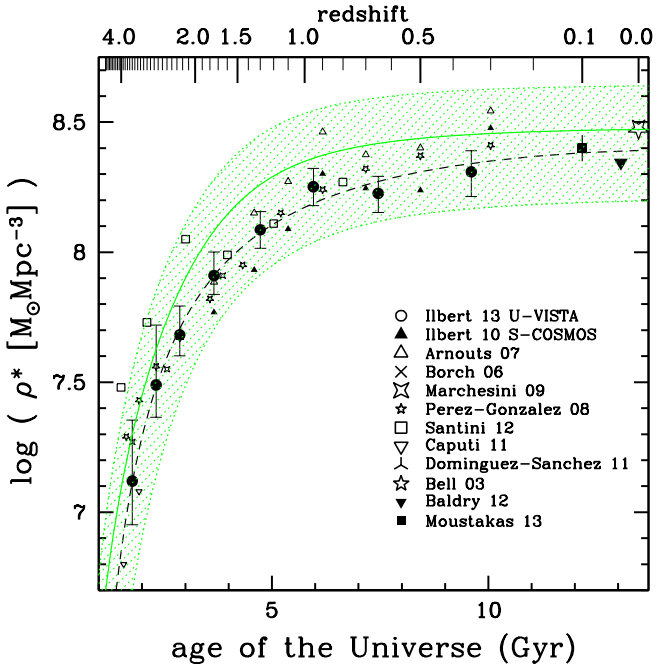

Figure 3.7: Stellar mass density from Ilbert et al. (2013) as a function of cosmic time (redshift is given in the top label). The circles correspond to our results using UltraVISTA. The green shaded area corresponds to the cosmic SFRD compiled by Behroozi et al. (2013) and integrated over cosmic time. The dashed line corresponds to the best fit over the mass density data.

3.3.1 Stellar mass density at $0.2 < z < 4$ from UltraVISTA in DR1

We used the tool ALF (Ilbert et al. 2005) to derive the GSMF . I developed this tool with L. Tresse and E. Zucca during my PhD in order to derive the galaxy luminosity functions in the VIMOS VLT Deep Survey. This tool includes three non-parametric estimators ($1/V_{\rm max}$, SWML, C^+) and the parametric estimator STY, as detailed in Appendix A.2 of Ilbert et al. (2005). This tool has been updated to derive the GSMF (Ilbert et al. 2010). We tested this tool with a simulation and we put in evidence a bias occurring when specific galaxy populations are not detectable anymore at low masses (Ilbert et al. 2004). Therefore, we set the stellar mass limit in order to produce a complete mass selected sample and we verify that the three non-parametric estimators produce a consistent result over the considered mass range. The error budget on the GSMF includes the Poissonian errors, the photo-z redshift uncertainties, and the uncertainties in the mass estimate. We quantify the cosmic variance with the public tool `getcv` provided by Moster et al. (2011).

We fit a parametric form over the $1/V_{\rm max}$ non-parametric data. Following Pozzetti et al. (2010), we adopt a double Schechter function, defined as:

$$\phi(\mathcal{M})d\mathcal{M} = e^{-\frac{\mathcal{M}}{\mathcal{M}^*}}\left[\phi_1^*\left(\frac{\mathcal{M}}{\mathcal{M}^*}\right)^{\alpha_1} + \phi_2^*\left(\frac{\mathcal{M}}{\mathcal{M}^*}\right)^{\alpha_2}\right]\frac{d\mathcal{M}}{\mathcal{M}^*} \tag{3.2}$$

with $\mathcal{M}^*$ the characteristic stellar mass, α_1 and α_2 are the slopes which need to satisfy the following criteria $\alpha_2 < \alpha_1$, and ϕ_1^* and ϕ_2^* correspond to the normalization. While a single Schechter function was still appropriated for survey like the VVDS, the depth of UltraVISTA or recent surveys like zFourge (Tomczak et al. 2013) imposes the use of a double Schechter function. Indeed, a turn up in the low mass end of the non-parametric GSMF is clearly visible with these surveys, as well as in the local Universe (Baldry et al. 2012, see Fig.3.5).

A crucial step in our fitting procedure is to account for stellar mass uncertainties, which could bias our estimate of the high-mass end (Caputi et al. 2011). Since the galaxy density exponentially decreases towards massive galaxies, errors in the stellar mass scatters more galaxies into the massive end than the reverse (Eddington 1913). We quantify the stellar mass uncertainties as a function of redshift. Then, we convolve the double Schechter function ϕ by the stellar mass uncertainties and fit this function on the $1/V_{\rm max}$ data. Therefore, the best-fit parameters are deconvolved by the expected stellar mass uncertainties.

The GSMF of the UltraVISTA survey from $z = 0.05$ to $z = 4$, are shown with black points in Fig.3.6. We also compare our results with several GSMF published since 2008 and we find an excellent agreement. Still, the differences in normalization are as large as 0.2 dex in some bins which could be explained by cosmic variance. We also find that the extrapolation of our GSMF slope is flatter than data from Santini et al. (2012) while in good agreement with Tomczac et al. (2014).

We derived the stellar mass density by integrating the double Schechter functions over the mass range 10^8 to $10^{13}\mathcal{M}_\odot$. The results are shown in Fig.3.7 (black circles). We fit the stellar mass density by the parametric form $\rho_*(z) = a \times e^{-bz^c}$. Our best fit function is shown with a dashed line in Fig.3.7 for the best fitting parameters $a = 2.46^{+0.35}_{-0.29} \times 10^8$, $b = 0.50^{+0.19}_{-0.16}$ and $c = 1.41^{+0.40}_{-0.31}$. We find that the global stellar mass density increases by 1.1 dex between $3 < z < 4$ and $0.8 < z < 1.1$ (a factor 13 in 4.2 Gyr). The evolution is slow at $z < 1$ with an increase of 0.2 dex between $0.8 < z < 1.1$ and the local estimate (a factor 1.6 in 6 Gyr). Therefore, the stellar mass is assembled twice as fast at $1 < z < 4$ (14% of the local stellar mass density per Gyr) than at $z < 1$ (6% of the local stellar mass density per Gyr).

3.3.2 Infer the SFH from the stellar mass density

Following Wilkins et al. (2008), we can link the mass density evolution and the star formation history using

$$\rho_*(t) = \int_0^t SFRD(t')(1 - f_r[t - t'])dt' \tag{3.3}$$

with f_r being the stellar mass loss depending on the age of the stellar populations (Renzini A. & Buzzoni A., 1986). We adopt the parametrisation of the stellar mass loss provided by Conroy & Wechsler (2009) for a Chabrier (2003) IMF $f_r(t-t') = 0.05ln(1+(t-t')/0.3Myr)$.

In Fig.3.7, we compare the mass density obtained with our data (black circles) and the mass density evolution expected by integrating the SFRD compilation of Behroozi et al. (2013, green line and shaded area). We find that the expected mass density is systematically higher by 0.05-0.2 dex than our data, while still consistent with the uncertainties. The discrepancy between direct and inferred mass densities reaches 0.2 dex at $z \sim 1.5$, and decreases at lower redshift. Burgarella et al. (2013) and Madau & Dickinson (2014) reach a similar conclusions.

We also inferred the global SFH from the mass density evolution following Wilkins et al. (2008). We adopt a functional form for the SFH having three free parameters. We fit these three free parameters to reproduce the observed mass density. We fit the UltraVISTA mass density data using equation 3.3 and the parametrisation of the star formation history of Behroozi et al. (2013):

$$SFRD(z) = \frac{C}{10^{A(z-z_0)} + 10^{B(z-z_0)}}. \tag{3.4}$$

The resulting best fit parameters are $B = 0.194^{+0.128}_{-0.082}$, $C = 0.111^{+0.040}_{-0.029}$ and $z_0 = 0.950^{+0.343}_{-0.410}$. We set $A = -1$ as Behroozi et al. (2013). Our inferred SFH and the associated uncertainties are shown with the black solid line and the shaded area in Fig.3.4. The inferred SFH is compared with recent measurements of the SFRD at $0 < z < 4$ in the left panel, and with the compilations from Behroozi et al. (2013) and Madau & Dickinson (2014). Below $z < 1$, the agreement between our inferred SFH and the literature is excellent. At $1 < z < 3$, our inferred SFH has a lower value than all the data from the literature. Still, the agreement is excellent when we consider the IR data from Gruppioni et al. (2013) and the latest compilation from Madau & Dickinson (2014) within the expected uncertainties.

In Hopkins et al. (2006) and Wilkins et al. (2006), the disagreement between direct SFRD measurements and the SFH inferred from the mass density was reaching 0.6 dex. Therefore, these authors advocated a possible change of the IMF with time. Mainly because of the new SFRD measurements, this tension almost disappeared now.

3.4 Summary

The evolution of the SFRD and of the stellar mass density provide two complementary probes of the global SFH. We combine them in this chapter.

I described the results of three studies using the UV, the far-IR and the radio emissivity to characterize the SFR. Using large and complete sample of galaxies, mainly from the COSMOS and the VVDS surveys, we were able to derive the global SFH out to $z = 4$. I showed that these various measurements are in excellent agreement out to $z = 1.5$, confirming the rapid increase of the SFRD over a period of time elapsing 70% of the age of the Universe. Such a measurement is in excellent agreement with the literature and is

well characterized. But significant differences appear at $1.5 < z < 4$, at the peak of the SFRD. All the samples based on UV, far-IR, or radio present their own limits: we need to extrapolate the contribution of the faint UV and IR sources since they are not directly detected; the dust correction necessary for the UV tracer is extremely unsecure; the radio analysis is based on stacking. While I focused on few studies, the comparison between the various compilations of the literature shows also large variations (Hopkins et al. 2006, Madau & Dickinson 2014).

In this chapter, I described another method that we applied to estimate the global SFH. By measuring the stellar mass accumulated along cosmic time, one can estimate the global SFH. This method is complementary to the use of direct SFR tracers since it relies on a different observable, i.e. the stellar mass. Such a method has not been applied in the literature since the first paper of Wilkins et al. (2008). We applied it to the new GSMF and mass density measurements that we obtained in UltraVISTA (Ilbert et al. 2013). We obtained an excellent agreement with the most recent SFRD compilation by Madau & Dickinson (2014). While this agreement is encouraging, we note that the uncertainties above $z > 2$ remain quite high with both methods. The recipes to decrease the uncertainties are standard: we need to go deeper to limit the extrapolation toward faint luminosities or masses; we need to improve the accuracy of our SFR tracers; we need to extend the results at $z > 4$ with several probes.

Chapter 4

Evolution of the specific star formation rate at $0.2 < z < 4$

In the last few years (Noeske et al. 2007b, Elbaz et al. 2007), it was established that the SFR and the stellar mass $\mathcal{M}_\star$ correlates. The $\mathcal{M}_\star$ – SFR relation provides a deep insight on the galaxy stellar mass assembly processes by characterizing how the instantaneous SFR is linked to the galaxy past star formation history. The dispersion in this relation characterizes the stochasticity in the star formation history. Outliers in the relation is also a way to isolate starbursting galaxies (Sargent et al. 2012).

The evolution of this relation is extremely important since it indicates that the star formation activity increases globally shifted with redshift. It implies that the star formation activity is driven by something fundamental occurring in all galaxies simultaneously. Indeed, the baryonic gas falls continuously on the central galaxy of a DM halo at a rate driven by the hierarchical growth of the DM structures. Therefore, the material potentially converted into new stellar populations fall on the galaxies at a rate proportional to the growth of the DM halos. I will show in section 4.4 that the evolution of the specific star formation rate (hereafter *s*SFR, defined as the ratio between SFR and stellar mass) is indeed proportional to the specific mass increase rate of the dark matter halo, despite the complexity of all the physical processes impacting the star formation. Therefore, having an accurate measurement of the *s*SFR evolution with cosmic time is extremely important to relate the stellar mass assembly with the cosmological context.

Numerous measurements on the evolution of the *s*SFR with redshift exist in the literature out to $z \sim 6$ and above. They are often based on direct tracers of the SFR. Assuming that the *s*SFR is independent of the mass, Elbaz et al. (2011) estimate that $s\mathrm{SFR}[Gyr^{-1}] = 26 \times t_{cosmic}^{-2.2}$ with t_{cosmic} in Gyr from $z \sim 0.1$ out to $z \sim 2$. As we discuss in section.4.3, a lot of uncertainties exist at $z > 2$ with a possible presence of a "plateau" in the *s*SFR evolution (Weinmann et al. 2011).

In this chapter, we present our own measurements based on the COSMOS data. I will focus on two studies (Ilbert et al. 2013, Ilbert et al. 2015). These two studies are based on new methods which complement other results from the literature. In Ilbert et

al. (2015), we produce a measurement of the "sSFR functions" per stellar mass bins out to $z < 1.4$. We used those functions to estimate the median sSFR correcting for selection effects. This method was applied at $z < 1.4$ and we obtained different results from the literature. Then, we also extend the estimate of the sSFR evolution out to $z < 4$ using a new method based on the stellar mass census rather than direct SFR tracer, as described in Ilbert et al. (2013). Finally, I will discuss the evolution of the sSFR in the general framework of the cosmological accretion rate into the halos.

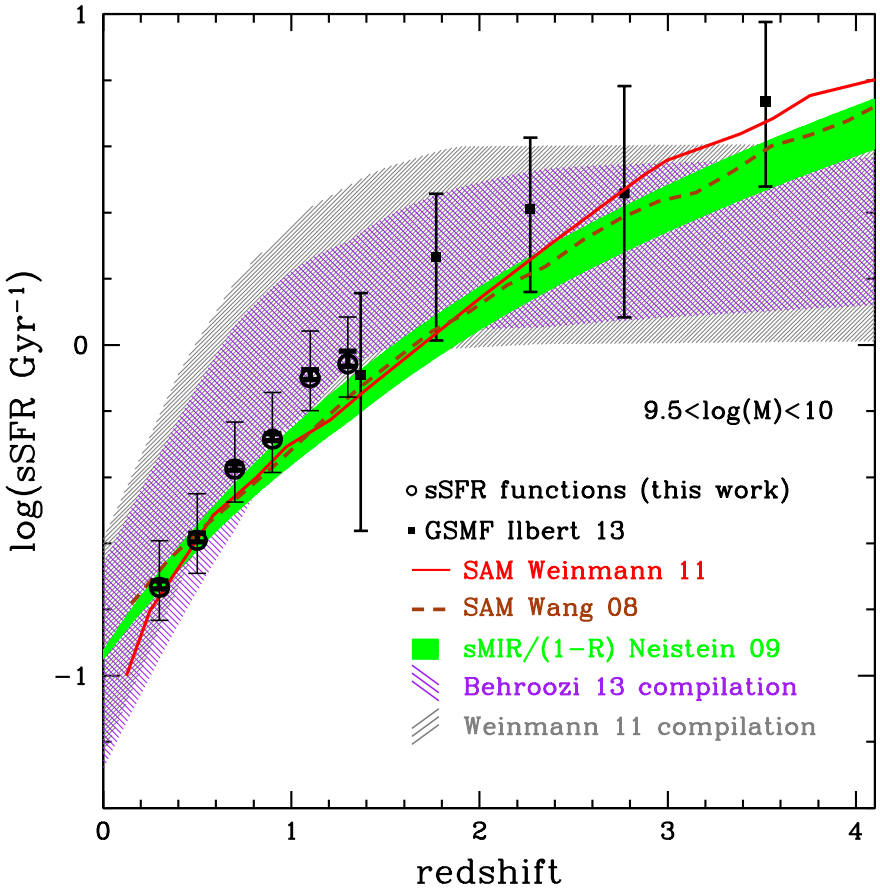

Figure 4.1: Evolution of the sSFR ($\mathrm{SFR}/\mathcal{M}_\star$) derived from the UltraVISTA mass functions (solid squares), and the sSFR functions (open circles). The gray and purple shaded areas correspond to the compilations from Weinmann et al. (2011) and Behroozi et al. (2013), respectively. The predictions of the SAM from Weinmann et al. (2011) and Wang et al. (2008) are shown with the red and brown lines. Finally, the green line corresponds to the analytical relation from Neistein et al. (2008) to describe the sMIR evolution (divided by the return fraction).

4.1 Link with the cosmological accretion rate

In simple models, the evolution of the sSFR is coupled with the evolution of the specific Dark Matter Increase Rate ($sMIR_{DM}$) defined as $\dot{M}_H/M_H$ with M_H the mass of the considered DM halo (Bouché et al. 2010, Lilly et al. 2013). The $sMIR_{DM}$ evolution characterizes at which rate a DM halo grows depending on its DM mass. In a standard ΛCDM cosmology, Neistein & Dekel (2008) proposed an analytic formula to describe the evolution of the $sMIR_{DM}$:

$$sMIR_{DM} = 0.047\left(\frac{M_H}{10^{12}}\right)^{0.15}(1+z+0.1(1+z)^{-1.25})^{2.5} \tag{4.1}$$

This equation shows that the $sMIR_{DM}$ increases with the halo mass and with the redshift. For a given halo mass, the DM halo growth rate was higher in the past, as shown in Fig.4.1 (left, green line).

When matter falls into the halo, it contains a constant fraction of baryonic matter which can be converted into stars. We obtain that the sSFR follows the $sMIR_{DM}/(1-R)$ (R is the return fraction) with the following assumptions:

- the baryonic fraction is universal;
- a constant fraction of the baryonic gas present into the halo penetrates the galaxy;
- the baryonic gas within the galaxy is instantaneously converted into stellar populations;
- only a fraction (1-R) of the stellar mass created is trapped for a long time.

In the last few years, numerous models based on these simple hypothesis have been developed (e.g. Bouché et al. 2010, Davé et al. 2012, Lilly et al. 2013). While these models are based on the same simple idea, they differ in the details. For instance, Lilly et al. (2013) include a gas reservoir in the galaxy which could evolve with time, an outflow rate directly proportional to the SFR with $\Psi = \lambda \times SFR$ and a timescale to consume the gas of the reservoir $\tau_{gas} = \varepsilon^{-1}$ with ε being the star formation efficiency in their formalism. If τ_{gas} is much shorter than the different timescales present in the system, Lilly et al. (2013) show that the galaxy is "gas-regulated". The galaxies reach an quasi-equilibrium, and the sSFR converges very quickly to the $sMIR_{DM}/(1-R)$. The conclusions are similar in Bouché et al. (2010) and Davé et al. (2012). Bouché et al. (2010) imposed a low-mass floor to start the star-formation.

Even more interestingly, the evolution of the sSFR predicted in complex semi-analytical models follow really closely the evolution of the $sMIR_{DM}/(1-R)$ as shown in Fig.4.1. The conclusion is similar for hydrodynamical simulations (Furlong et al. 2015). Despite the inclusion of SN and AGN feedback, or galaxy merging, the evolution of the sSFR is governed by the DM structure growth in cosmological simulations.

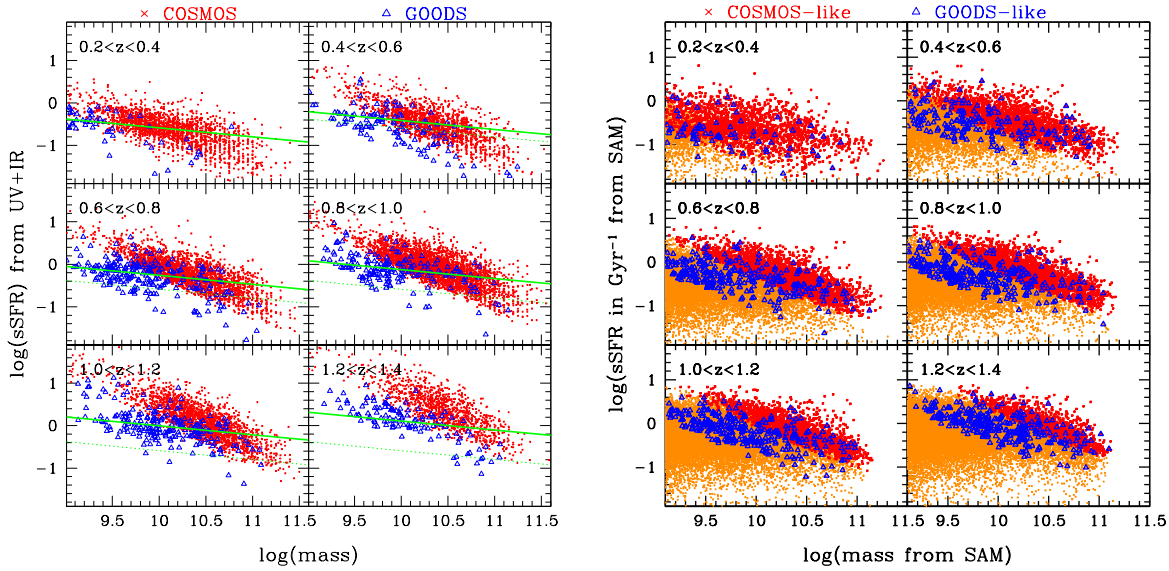

Figure 4.2: **Left:** *s*SFR as a function of the stellar mass in the GOODS (blue triangles) and COSMOS (red crosses) fields with the SFR measured from the UV and IR data. The green dashed lines are obtained using the parametrisation obtained by Rodighiero et al. (2011) and Elbaz et al. (2011). The green dashed line corresponds to the relation measured $0.2 < z < 0.4$. **Right:** *s*SFR as a function of the stellar mass using the prediction of the semi-analytical model. The orange points are the mass and the *s*SFR of the full simulated catalogue. The blue triangles and the red crosses correspond to a GOODS-like and a COSMOS-like survey, respectively.

4.2 *s*SFR functions at $z < 1.4$

In this section, I present part of the results from Ilbert et al. (2015). Using the MIPS $24\mu m$ in the COSMOS and GOODS fields, we characterized the evolution of the sSFR functions in order to better understand the evolution of the mass-SFR relation. I will demonstrate that such a method is important to avoid selection biases and I will will focus on the evolution of the sSFR with redshift.

4.2.1 $\mathcal{M}_\star$ – *s*SFR scatter plot and selection effects

Figure 4.2 shows the distribution of the *s*SFR as a function of the mass for star-forming galaxies in the COSMOS field (red crosses) and in the GOODS field (blue triangles). The two samples are MIPS 24 μm selected and the SFR is measured by summing the contribution of the IR and UV light.

Since GOODS covers a small volume with a deep NIR coverage, this sample includes preferentially low mass galaxies at $z < 1$, while COSMOS which covers an area $\times 30$ larger includes rare and massive sources. This difference explains why the GOODS and the COSMOS samples cover a different mass range in Fig.4.2. A $\times 3$ difference in sensitivity

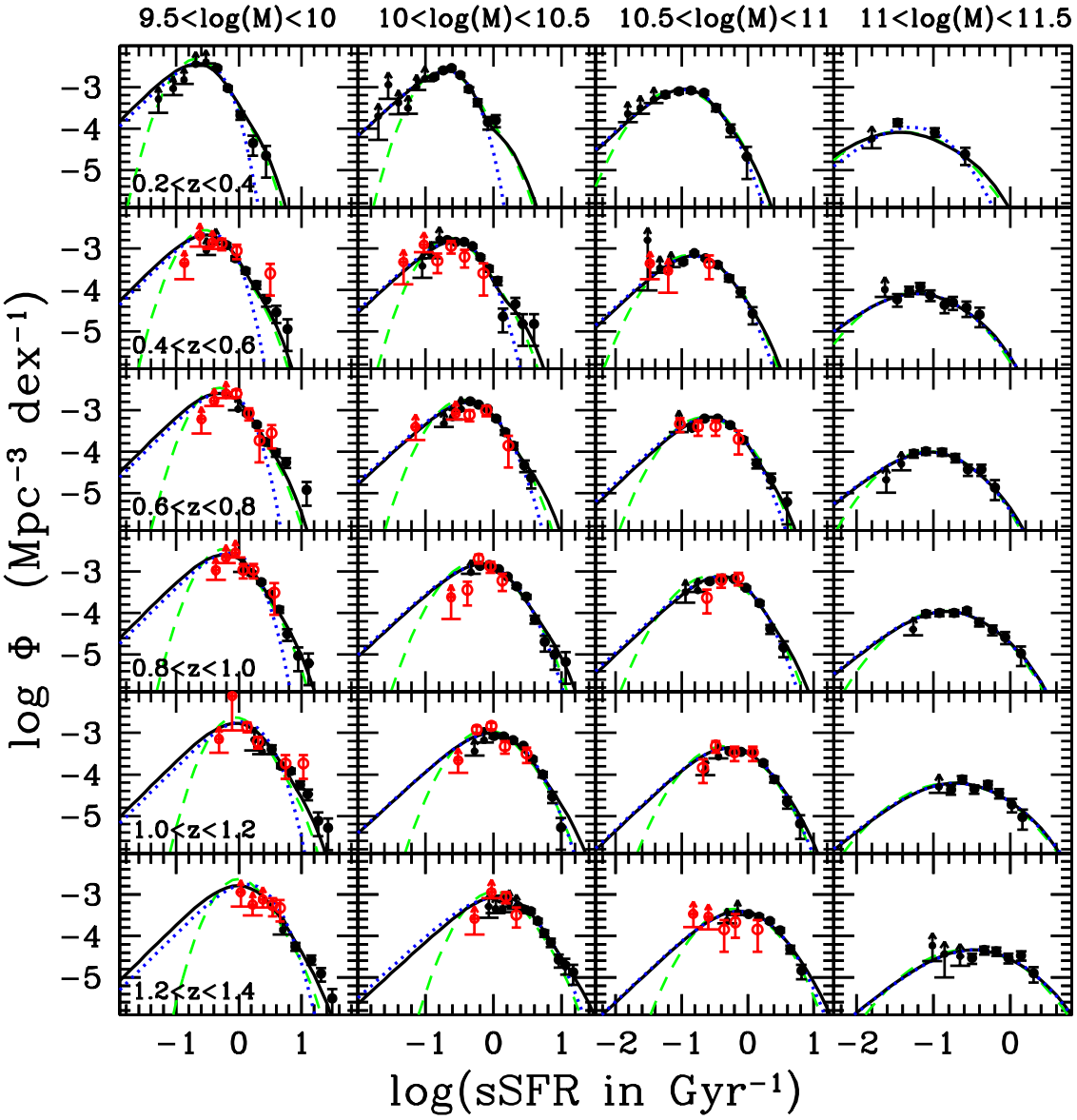

Figure 4.3: *s*SFR functions per redshift bin from $0.2 < z < 0.4$ to $1.2 < z < 1.4$ (from the top to the bottom rows) and per stellar mass bin from $9.5 < log(\mathcal{M}_\star) < 10$ to $11 < log(\mathcal{M}_\star) < 11.5$ (from the left to the right columns). The non-parametric data have been obtained using the $1/V_{max}$ estimator. The black filled and red open circles correspond to the COSMOS and GOODS fields, respectively. The arrows correspond to the lower limits obtained with the $1/V_{max}$. The black solid lines and green dashed lines correspond to the best-fit functions assuming a double-exponential and a log-normal profile, respectively. Both include a starburst component. The blue dotted lines correspond to the double-exponential fit without considering the starburst component.

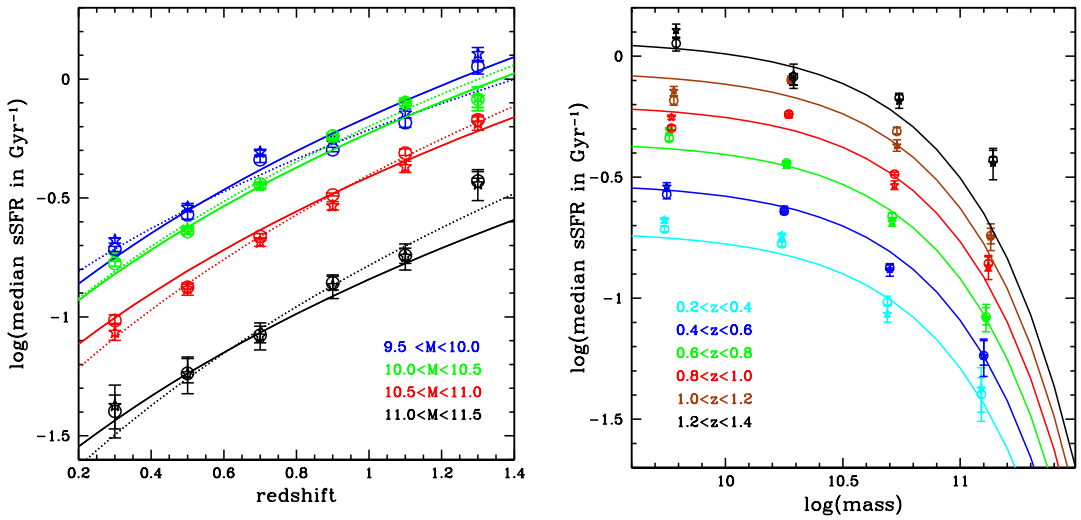

Figure 4.4: Evolution of the median sSFR as a function of redshift (left panel) and mass (right panel). Open circles and open stars correspond to the values measured assuming a log-normal and a double-exponential profile, respectively. The solid lines correspond to the fit using Eq.4.3 and b independent of $\mathcal{M}_\star$. The dotted lines are obtained with b varying in each mass bin. *Left:* each color corresponds to a stellar mass bin (blue: $9.5-10$ dex, green: 10-10.5, red: 10.5-11 and black 11-11.5). *Right:* each color corresponds to a redshift bin from $0.2-0.4$ (cyan) to $1.2-1.4$ (black).

between the two MIPS surveys explains why the sSFR values of the COSMOS survey are larger than the values found in GOODS. While the COSMOS survey includes mostly starbursting sources at low masses, the GOODS survey could reach the bulk of the star-forming population.

We apply the same selection criteria (flux selection and covered areas) to the predictions of a semi-analytical model (Wang et al. 2008). The predicted COSMOS-like and GOODS-like surveys cover a different position in the $\mathcal{M}_\star - s$SFR plan, exactly as for the observations. Even with the GOODS-like survey, the MIPS data are not sufficiently deep to get a representative sample of low mass galaxies in term of sSFR. It illustrates the necessity of taking into account selection effects in SFR limited surveys.

4.2.2 sSFR functions

As shown in section.4.2.1, a sample selected in MIPS (or any SFR tracer) introduces a selection effect in the analysis. Most of the analysis of the $\mathcal{M}_\star$-sSFR relation are based on scatter plots, which could be affected by selection effects. In order to overcome this limitation, we split the $\mathcal{M}_\star$-sSFR plane in several mass bins and characterized the sSFR distribution in each bin correcting for possible selection effects. An accurate and robust

information can be extracted from the analysis of the *s*SFR functions, i.e. number density in a comoving volume (in Mpc^{-3}) and per logarithmic bin of *s*SFR (in dex^{-1}). We derive the *s*SFR functions per stellar mass and redshift bin. We divide the star-forming sample into 6 redshift bins with $\Delta z = 0.2$ and four stellar mass bins $log(\mathcal{M}_\star) = 9.5 - 10$ dex, $10 - 10.5$, $10.5 - 11$, $11 - 11.5$.

In order to take into account the flux limit at $24\mu m$ ($F_{24\mu m} > 20\mu Jy$ in GOODS and $F_{24\mu m} > 60\mu Jy$ in COSMOS), we adopt standard estimators of the LF as the $1/V_{max}$ (Schmidt 1968), the SWML (Efstathiou 1988) and the C^+ (Lynden-Bell 1971). These estimators are included in the tool ALF used to compute the *s*SFR functions, as described in Appendix.B of Ilbert et al. (2005).

Figure 4.3 shows the non-parametric *s*SFR functions. We fit simultaneously the $1/V_{max}$ data of the COSMOS and GOODS fields. We consider a double-exponential profile (e.g. Saunders et al. 1990, Le Floc'h et al. 2005):

$$\Phi(sSFR) = \Phi^* \left(\frac{sSFR}{sSFR^*}\right)^{1-\alpha} exp(-\frac{log_{10}^2(1 + \frac{sSFR}{sSFR^*})}{2\sigma^2}) \quad (4.2)$$

with α the faint-end slope set at -0.5. We add a starburst component to the *s*SFR function following Sargent et al. (2012). We assume that the starburst galaxies are distributed with a log-normal distribution having $\sigma = 0.25$ and centered on four times the median *s*SFR of the main peak. We fit the $1/V_{max}$ data with a standard χ^2 minimization method. Still, we consider the lower limits obtained with the $1/V_{max}$ estimator below the completeness limit (arrows in Fig.4.3). We also include an additional constraint using the GSMF of the star-forming galaxies.

In Ilbert et al. (2015), we discuss in detail the method, the shape of the *s*SFR functions and the evolution of its shape with redshift and mass. In this manuscript, we focus on the *s*SFR evolution with redshift.

4.2.3 Evolution of the *s*SFR at $0.2 < z < 1.4$

Figure 4.4 shows the evolution of the median *s*SFR, extracted from the best-fit *s*SFR functions. We observe a clear increase of the *s*SFR as a function of redshift (left panel) and a decrease with $\mathcal{M}_\star$ (right panel). We adopt the following parametrisation of the *s*SFR evolution as a function of redshift and mass:

$$log(sSFR) = a + \beta \times \frac{\mathcal{M}_\star}{10^{10.5}\mathcal{M}_\odot} + b \times log_{10}(1 + z) \quad (4.3)$$

Assuming that the *s*SFR evolution does not depend on the mass, we find $a = -1.07^{\pm 0.02}$, $\beta = -0.172^{+0.007}_{-0.007}$ and $b = 3.14^{+0.07}_{-0.07}$. The result is shown with solid lines in Fig.4.4. Then, we relax the assumption that the parameter b is independent on the stellar mass and we fit independently each stellar mass bin. We obtained $b = 2.88^{+0.07}_{-0.07}$, $b = 3.31^{\pm 0.1}$, $b = 3.52^{\pm 0.15}$, $b = 3.78^{\pm 0.6}$ in the stellar mass bins $log(\mathcal{M}_\star) = 9.5 - 10$ dex, $10 - 10.5$, $10.5 - 11$ and

$11 - 11.5$, respectively. The result is shown with dotted lines in Fig.4.4. It suggests that the evolution is faster for the massive galaxies, which would imply a downsizing pattern (Cowie et al. 1996). I will discuss the evolution of the *s*SFR compared to other results from the literature in section.4.4 and I will make the link with $sMIR_{DM}$. But before that, I will establish the evolution of the *s*SFR at $1.5 < z < 4$ using the evolution of the GSMF.

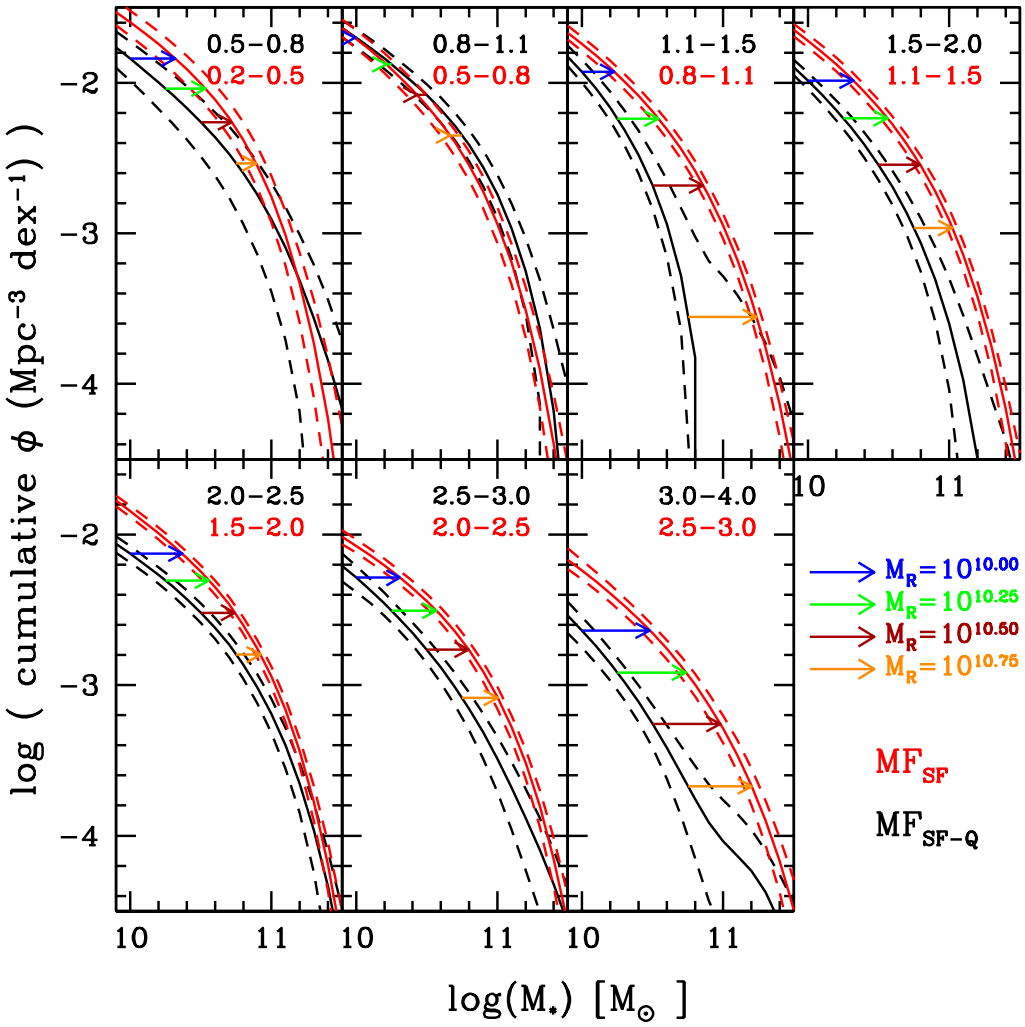

Figure 4.5: In each panel, we show the cumulative GSMF of star-forming galaxies at t_2 in red (lowest redshift bin) and at t_1 in black (highest redshift bin). The contribution of galaxies quenched between t_1 and t_2 is removed from the cumulative GSMF at t_1. The dashed lines correspond to the uncertainties. The shifts $\Delta \log \mathcal{M}$ used to estimate the *s*SFR are shown with the horizontal arrows at four reference masses: $\mathcal{M}_R = 10^{10}$, $10^{10.25}$, $10^{10.5}$, $10^{10.75} \mathcal{M}_\odot$ in blue, green, brown and orange, respectively.

4.3 An indirect method to estimate the *s*SFR at $1.5 < z < 4$

4.3.1 Description of the method

In Ilbert et al. (2013), we develop a new method to estimate the *s*SFR from the evolution of the GSMF per type. Rather than relying on a direct estimate of the SFR for each galaxy, we estimate by how much the stellar mass has grown for a given population in a considered time interval, which is directly linked to the *s*SFR of this population.

In order to apply this method, we consider an admittedly over-simplistic scenario in which evolution of star-forming GSMF is driven only by star formation (i.e. we consider that mergers do not significantly change the galaxy distribution between two redshift bins, see Section 4.3 of Boissier et al. 2010). Given this assumption, we can directly relate the *s*SFR at a given mass and the evolution of the star-forming GSMF. Indeed, the stellar masses increase by $\mathcal{M}(t_2) - \mathcal{M}(t_1) = \int_{t_1}^{t_2} SFR(t')(1 - f_r[t_2 - t'])dt'$ between t_1 and t_2 ($t_1 < t_2$), with f_r corresponding to the stellar mass loss (Conroy et al. 2009). Assuming that the SFR remains constant over the considered time interval and over the mass range $[\mathcal{M}(t_1), \mathcal{M}(t_2)]$, we obtain the specific SFR:

$$\mathrm{sSFR}(t_1) = \frac{10^{\Delta \log \mathcal{M}} - 1}{(t_2 - t_1 - \int_{t_1}^{t_2} f_r(t_2 - t')dt')} \tag{4.4}$$

with $\Delta\log\mathcal{M} = \log\mathcal{M}(t_2) - \log\mathcal{M}(t_1)$. The shift $\Delta\log\mathcal{M}$ is directly derived from the GSMF evolution of star forming galaxies between t_1 and t_2.

But an additional important ingredient needs to be taken into account: star-forming galaxies could be quenched and move to the quiescent population in the time interval $t_2 - t_1$. Since we want to compute $\Delta\log\mathcal{M}$ for the same galaxy population at t_1 and t_2, we need to remove the contribution of the galaxies quenched between t_1 and t_2.

In order to apply the method: 1) we consider two redshift bins around t_1 and t_2 and we compute the star-forming and quiescent GSMF; 2) since we know the GSMF of the quiescent galaxies at z_1 and z_2, we subtract the contribution of the galaxies which will be quenched between t_2 and t_1 (simply the difference between the GSMF of the quiescent galaxies) to the star-forming GSMF at t_2; 3) knowing how the GSMF of the star-forming galaxies evolved between z_1 and z_2, we can derive the *s*SFR at various masses in this redshift range.

4.3.2 Pros and cons of the method

One major difficulty of our method is to remove the contribution of the galaxies which will be quenched in the considered redshift range which is done statistically. At $z < 1.5$, the contribution of the quiescent galaxies to the global population reaches 80%. Therefore, the uncertainties on the quiescent GSMF generated by cosmic variance are propagated to

the sSFR. At $z > 1.5$, the global population is dominated by star-forming galaxies and the uncertainties linked to the quenching process stay limited. An interesting feature of our new method is that the sSFR estimate is more robust at high redshift than at $z < 1.5$. Therefore, the method is really complementary to the direct sSFR estimates which are robust at $z < 2$.

Another advantage is that the method is less affected by the uncertainties introduced by the SED fitting. First, because our method is based on stellar masses which are more robust than SFR (see section 3.1.1). Moreover, we are measuring a differential quantity between two redshift bins: a systematic error on the stellar mass does not affect our sSFR estimate, as long as this systematic error stays constant in the considered redshift bin (e.g. the choice of the IMF).

The main drawback of the method is the assumption that mergers do not affect the evolution of the star-forming galaxies. Including the impact of the mergers is challenging since we do not know how the merger rate depends on the stellar mass and if the end product of such a merger is quenched or not. Welker et al. (2015) show that mass assembly through gas accretion is dominant over the mergers at $z > 2$ which validates our approximation. We tested our method on a SAM (Wang et al. 2008) and we showed that we were able to retrieve the median sSFR with a slight bias of 0.05 dex (well below any bias affecting direct SFR tracer at such a redshift).

4.3.3 The sSFR derived from the UltraVISTA Mass Functions

We apply the method to the GSMF derived by Ilbert et al. (2013). We measure the shift $\Delta\log\mathcal{M}$ of Eq.4.4. These shifts are indicated with horizontal arrows in Fig.4.5. Since the sSFR could depend on the mass (e.g. Dune et al. 2009, Karim et al. 2011), we measure $\Delta\log\mathcal{M}$ at four reference masses ($\mathcal{M}_R = 10^{10}$, $10^{10.25}$, $10^{10.5}$ and $10^{10.75}\mathcal{M}_\odot$). We do not consider $\mathcal{M}_R < 10^{10}\mathcal{M}_\odot$ to limit the impact of the slope extrapolation at low masses. The top label of Fig.4.6 shows the evolution of the sSFR estimated at the four reference masses in our analysis. We find consistent sSFR for the three reference masses lower than $\mathcal{M} < 10^{10.75}\mathcal{M}_\odot$. In the bottom panel of Fig.4.6, we focus on the sSFR evolution measured for $\mathcal{M}_R = 10^{10}\mathcal{M}_\odot$, which is the less dependent on the removal of quenched galaxies. The sSFR increases from $z = 1$ to $z = 4$ (blue circles). The sSFR computed with this indirect method are compared with direct measurement of the sSFR from the literature. Given the size of the uncertainties, our inferred sSFR is in good agreement with literature measurements. We find a continuous increase of the sSFR at $z > 1$ with no "plateau" at $z > 2$.

4.4 Evolution of the sSFR

In Fig.4.1, we compare our own median sSFR measurements with two compilations from the literature. We also compare our own median sSFR measurements with the sSFR evolution expected from the $sMIR_{DM}/(1-R)$ and simulations.

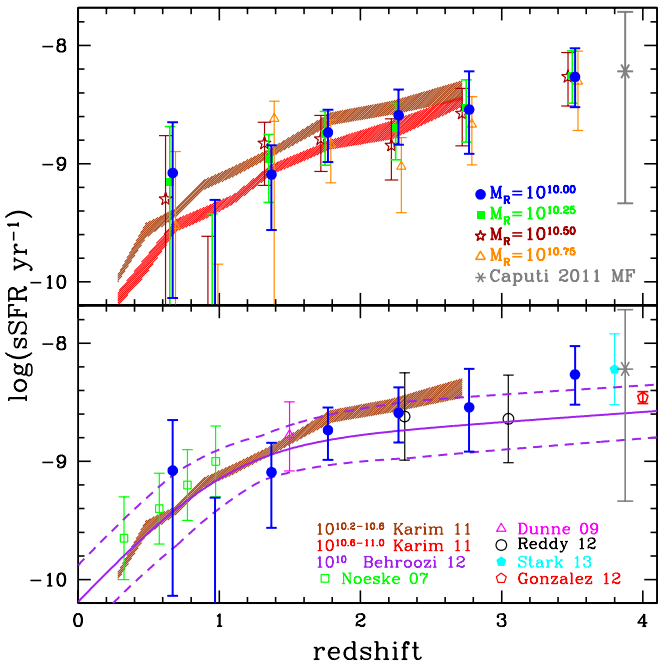

Figure 4.6: Evolution of the sSFR (SFR/$\mathcal{M}_\star$) derived from the UltraVISTA mass functions. *Top panel:* sSFR measured at different masses using the shifts $\Delta\log\mathcal{M}$ shown in Figure 4.5. The sSFR computed at four reference masses $\mathcal{M}_R$ = 10^{10}, $10^{10.25}$, $10^{10.5}$, $10^{10.75}\mathcal{M}_\odot$ are shown with blue circles, green squares, brown stars and orange triangles, respectively. The brown and red shaded areas for Karim et al. (2011) correspond to the mass bins $10^{10.2}-10^{10.6}\mathcal{M}_\odot$ and $10^{10.6}-10^{11}\mathcal{M}_\odot$, respectively. *Bottom panel:* sSFR estimated at $10^{10}\mathcal{M}_\odot$ compared with measurements from the literature. Our measurement is the only one based on the GSMF.

We focus on the sSFR evolution measured for $\mathcal{M} = 10^{10}\mathcal{M}_\odot$. We start with this mass range since the sSFR extracted from the GSMF is less sensitive to the removal of quenched galaxies. Our own estimates bring a different perspective since: 1) the evolution of the sSFR at $z < 1.4$ is based on a full analysis of the sSFR functions which is a new approach (section 4.2); 2) the evolution of the sSFR at $z > 1.5$ is based on the stellar mass census, which is complementary to direct tracers of the sSFR (section 4.3).

At $z < 1.4$, our sSFR estimates correspond to the lower part of the Weinmann et al. (2011) and Behroozi et al. (2013) compilations. At $z < 1.4$, the various estimates of the sSFR did not evolve significantly in the last few years. Still, the inter-publication scatter reaches 0.3 dex at $z \sim 1$ (Behroozi et al. 2013). Most studies based their sSFR estimates on SFR limited samples which are potentially affected by several selection biases. We interpret the difference between our results and the rest of the literature by the contribution of the low sSFR galaxies that we take into account when we derive the sSFR functions.

The gray shaded area in Fig.4.1 shows a compilation by Weinmann et al. (2011). The observed sSFR seems to increase faster than the $sMIR_{DM}$ at $z < 1.5$, then the sSFR reaches

a "plateau" while the $sMIR_{DM}$ is still increasing with redshift (Weinmann et al. 2011). Weinmann et al. (2011) conclude that they cannot reproduce the sSFR "plateau" without introducing unrealistic star formation recipes into the semi-analytical models. The reality of the sSFR "plateau" at $z > 2$ is debated and the current measurements have a large scatter at $z > 2$. In the last few years, the sSFR estimates have significantly changed at $z > 2-3$. Recent studies by de Barros et al. (2014) indicate that including emission lines into the template to estimate the sSFR could completely change its values by 1-2 dex at $3 < z < 6$. It illustrates how the sSFR based on SED-fitting procedure is sensitive to the method used for its estimation (see for instance section.3.1.1). But even using the recent compilation by Behroozi et al. (2013) (purple shaded area in Fig.4.1), the evolution of the sSFR does not follow the $sMIR$ evolution. At $z > 1.5$, we find a continuous increase of the sSFR based of the GSMF evolution. Our method is the only one which is based on the stellar masses. The advantage of this method is that it becomes more robust at higher redshift (less hypothesis on the removal of quenched galaxies, smooth accretion dominates the mass assembly). Still, we will need to confirm such an evolution with new GSMF measurement at $z > 4$.

When taken together, our observed sSFR evolution follows the $sMIR_{DM}/(1-R)$ evolution (blue points in Fig.4.1). Therefore, one could conclude that the observed evolution is well driven by the growth of large scales structures as expected, without the need of introducing important missing physical processes.

The situation is not so simple when we compare our results at higher masses. We limit ourselves to the study at $z < 1.4$ since the removal of quenched galaxies could be problematic for the high mass galaxies. Fig.4.7 shows the predicted evolution of the median sSFR with redshift compared to our measurements. The median sSFR evolves faster in the data than in the model. In the data, b varies from 2.7 to 3.8 from low mass to high mass galaxies. We find the reverse trend in the simulation. The simulation predicts that b decreases with mass: b =2.3, 2.1, 1.9, 1.5 at $log(\mathcal{M}_\star) = 9.5-10$ dex, $10-10.5$, $10.5-11$ and $11-11.5$, respectively. As discussed in Weinmann et al. (2012), the evolution of the sSFR in the semi-analytical models follow closely the $sMIR_{DM}$. Therefore, our observed evolution of the sSFR is consistent with the evolution of the $sMIR_{DM}$ for $\mathcal{M}_\star < 10^{10}\mathcal{M}_\odot$, but deviates from it at higher masses. The modelisation of complex physical processes affecting the SFH in massive galaxies, as quenching or secular evolution, still needs to be improved.

4.5 Summary

Measuring the sSFR evolution with time is a crucial tool to verify our understanding of the galaxy evolution. Most of the models which capture the cosmological context, from the simplest bathtub model (Lilly et al. 2013) to the most complex hydrodynamical simulation (Furlong et al. 2015) obtained that the sSFR follows the cosmological accretion rate. Once compiled, observations based on direct tracers of the SFR, from the UV to the radio, shows significant deviation from the expected evolution. Observations seem to show a more rapid

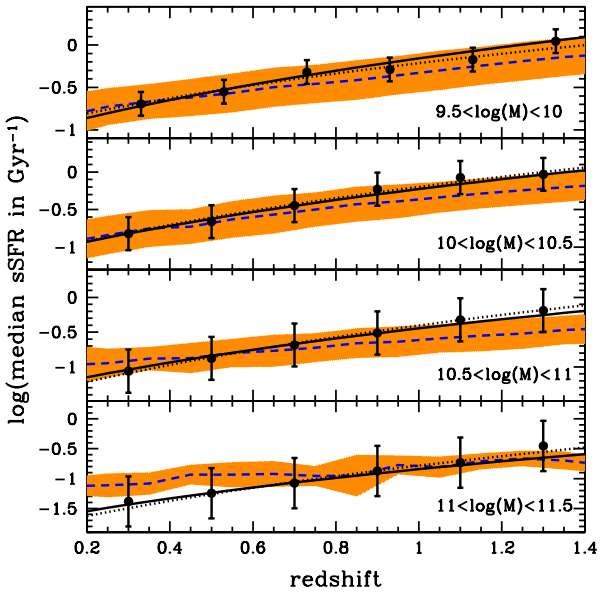

Figure 4.7: Evolution of the *s*SFR as a function of redshift. Each panel corresponds to a stellar mass bin. The solid circles correspond to the median *s*SFR measured with the *s*SFR functions. The vertical errorbars indicate the σ derived from the fit with a log-normal function (they do not correspond to real uncertainties on the median *s*SFR). The blue dashed lines correspond to the median *s*SFR measured on the semi-analytical model from Wang et al. (2008). The orange area is derived by measuring the r.m.s. of the *s*SFR in the semi-analytical model.

increase of the *s*SFR from $z = 0$ to $z = 1.5$, and then a change of regime at $z > 1.5$ leading the observed *s*SFR to be lower than the expected one. One could possibly show that we miss a crucial ingredient in our current understanding of the galaxy evolution (Tasca et al. 2015). In this chapter, we find that the *s*SFR evolution follows the cosmological accretion rate at odd with the literature. In Ilbert et al. (2015), we find an evolution of the *s*SFR following the cosmological accretion rate at $z < 1.5$ using a new method to derive the median *s*SFR and correcting for selection effects. However, an uncertainty of 0.1 dex exists in the absolute normalization of the COSMOS MIPS images that we used (H. Aussel, private communication) which could affect our conclusions. Moreover, a similar analysis should be pushed at lower masses $\mathcal{M}_\star < 10^{9.5}\mathcal{M}_\odot$. In Ilbert et al. (2013), we also find an evolution of the *s*SFR following the cosmological accretion rate at $1.5 < z < 4$, based on the analysis of the stellar mass function. However, such a method present numerous uncertainties, the main one being the approximation that major mergers are not biasing our measurements on the considered timescale. Given the importance of this scientific problem, such methods should be tested in more details through simulations and pushed at higher redshift when the expected *s*SFR falls well below the predicted one in current observations.

Chapter 5

Quenching

There is a well established bimodality in the galaxy colors out to $z \sim 2$ (e.g. Whitaker et al. 2011, Ilbert et al. 2013). This bimodal distribution is a common tool used to differentiate two populations: "blue cloud" (called here star-forming) and "red sequence" (called here quiescent) galaxies (e.g. Bell et al. 2004, Faber et al. 2007, Franzetti et al. 2007, Fritz et al. 2014). I will describe in a first section how do we discriminate observationally between star-forming and quiescent galaxies.

The presence of a color bimodality suggests that the transition from star-forming galaxies into quiescent has been fast and that the star formation was suppressed in a short timescale (less than a Gyr). This process is called "quenching". Quenching needs to be differentiated from the gradual decline of the SFR within the galaxies. If the quenching timescale was lasting for several Gyr, the transition between the star-forming and the quiescent population should be filled by transitioning galaxies, making less apparent the color bimodality. Quenching is also crucial to explain the shape of the GSMF. An efficient feedback process is absolutely necessary to suppress the star formation in the most massive halos, and to explain the difference between the DM mass function and the GSMF high mass end. Since the quiescent galaxies dominate the massive population and can not grow significantly through gas accretion, it implies a reservoir of massive star-forming galaxies in the early Universe which can be their progenitors.

Numerous processes have been introduced in galaxy formation models to explain the quenching: the energetic outflows from bright AGN, the heating of the gas within massive DM halos, the impact of the environment, etc. These processes have a different efficiency depending on the considered DM halo mass and on the considered epoch. In a second section, I will describe the various physical processes in capacity to suppress the star-formation activity.

In this manuscript, I present one of the most important observables to constrain the galaxy quenching, i.e. the GSMF evolution of the quiescent galaxies. Such an observable quantifies how fast galaxies are quenched over cosmic time and at which stellar mass. In order to understand the quenching processes, I also need to describe the evolution of the "reservoir" of the galaxies that could potentially quench. Therefore, I will discuss the

evolution of the GSMF of star-forming galaxies when useful to understand the quenching processes. I will present mostly the results of our two papers Ilbert et al. (2010) and Ilbert et al. (2013). I will interpret this evolution using the formalism of Peng et al. (2010) in term of mass quenching and environment quenching.

Finally, it is clear in the local Universe that quiescent galaxies have an elliptical morphology. We will discuss in a last section what do we learn by combining the morphology and quiescence analysis.

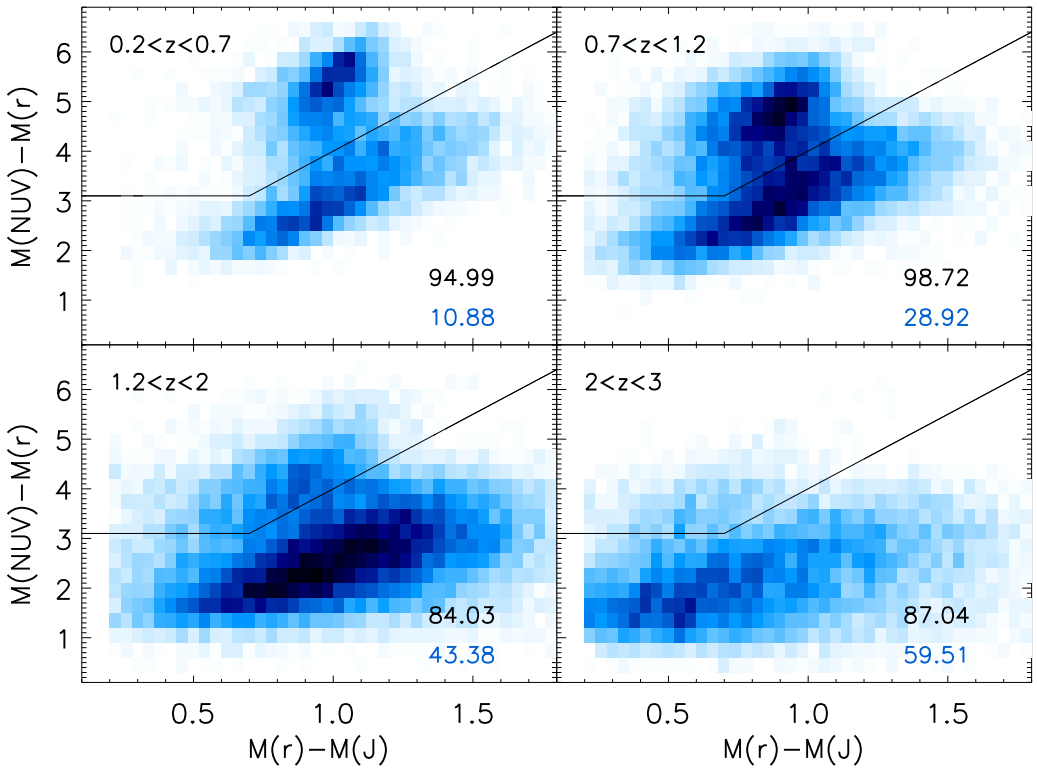

Figure 5.1: Two-color selection of the quiescent population. The galaxies above the black line in the top left are selected as quiescent. The fraction (in %) of $log(sSFR) < -11$ galaxies selected by the two-color selection box corresponds the top number in each panel. The fraction of galaxies with $log(sSFR) > -11$ within the two-color box corresponds the bottom number.

5.1 Separate star-forming and quiescent galaxies

Several methods could be used to separate star-forming and quiescent galaxies. Originally, the red sequence galaxies are defined based on the rest-frame color $U - B$ (e.g. Faber et al. 2007) or $U - V$ (e.g. Bell et al. 2004) versus an absolute magnitude. However, a

single color classification suffers from a major weakness, specially severe at $z > 1$: dust-extinguished star-forming galaxies appear as red as quiescent galaxies in $U - B$ or $U - V$, and they could be wrongly classified as quiescent. For instance, for a MIPS selected sample in COSMOS, we would wrongly classified 20% of the star-forming galaxies more massive than $\mathcal{M}_\star > 10^{10.5}\mathcal{M}_\odot$ as quiescent using only a selection $(M_{NUV} - M_R) > 3.5$.

In the last decade, numerous diagnostics have been proposed that tackle this problem. A color-color selection technique ($M_U - M_V$ versus $M_V - M_J$) has been proposed by William et al. (2008). This color-color selection breaks the degeneracies between dust-extincted star-forming galaxies and those with a quenched star-formation. The red clump is clearly isolated from the star-forming sequence by a lower density region in which galaxies transit rapidly.

In order to divide the sample into quiescent and star-forming galaxies, we use a slightly modified version of the two-color selection technique proposed by Williams et al. (2009). Following Ilbert et al. (2010), we use the rest-frame two-color selection $\mathrm{NUV} - r^+$ versus $r^+ - J$ instead of $U - V$ versus $V - J$. In fact, $\mathrm{NUV} - r^+$ is a better indicator of the current versus past star formation activity (e.g. Martin et al. 2007, Arnouts et al. 2007). Moreover, the dynamical range covered by the $\mathrm{NUV} - r^+$ rest-frame color is larger than the one covered by $U - V$, making the $\mathrm{NUV} - r^+$ rest-frame color less sensitive to uncertainties linked to observations. Finally, the NUV rest-frame is still sampled by optical data at $z > 2$ which is no longer true for the rest-frame U band. This criteria is really similar to the one studied by Arnouts et al. (2013) which combines the two rest-frame colors $M_{NUV} - M_R$ and $M_R - M_K$. As shown by Arnouts et al. (2013), the extinction moves star-forming galaxies along a diagonal axes from the bottom left to the top right.

We note that we derive the absolute magnitudes with the method of Ilbert et al. (2005) which minimizes the k-correction dependency. When the absolute magnitude is computed at $\lambda_{rest-frame}$, we base its estimate on the apparent magnitude measured at $\lambda_{rest-frame}(1 + z_{gal})$. Therefore, our color selection is the less dependent as possible on the SEDs used to derived the absolute magnitudes.

Another possibility is to use the physical parameters directly extracted from the template-fitting procedure in order to separate the quiescent and the star-forming galaxies. For instance, Peng et al. (2010) used a bimodality in the $\mathcal{M}_\star$-SFR plane. In Ilbert et al. (2010) and Domínguez Sánchez et al. (2011), we considered that a galaxy was quiescent when $log(s\mathrm{SFR}[yr^{-1}]) < -11$. The fraction of galaxies with $log(s\mathrm{SFR}[yr^{-1}]) < -11$ in the selection box is given in each panel of Fig.5.1. Over the full redshift range, ~90% of the galaxies with $log(s\mathrm{SFR}) < -11$ are in the selection box. We also indicate the fraction of galaxies with $log(s\mathrm{SFR}) > -11$ in the selection box. The fraction of galaxies with $log(s\mathrm{SFR}) > -11$ increases from 20% at $z < 1$ to 60% at $2 < z < 2.5$. Therefore, both classifications provide similar results at $z < 1$. But the classification based on the sSFR is more conservative at high redshift.

In the following, we adopt the classification based on a simple two-color selection that is less dependent on the template fitting than the $\mathcal{M}_\star$-SFR bimodality.

5.2 Physical processes involved in quenching

In this section, we describe the various physical processes included into the simulations which can explain why and when galaxies quenched.

5.2.1 The AGN bright-mode feedback and the link with gas-rich mergers

Magorrian et al. (1998) show a relation between the mass of a central black hole and the mass of a spheroid. Such a relation, confirmed by numerous studies (e.g. Ferrarese & Merritt 2000), suggests a co-evolution between the black hole and the bulge formation. In semi-analytical models (e.g. Croton et al. 2006, Bower et al. 2006) as well as hydrodynamical simulations (e.g. Dubois et al. 2012), AGN feedback is used to quench the star-formation in massive galaxies. Two different modes of AGN activity are usually considered: the "bright mode" (e.g. QSO) and the "radio mode" which radiates less energy than the "bright mode" but is a more common mechanism (e.g. Croton et al. 2006).

In this subsection, we first discuss the "bright" mode. Sanders et al. (1988) propose a scenario in which the merger between two gas rich disk galaxies triggers an intense star-formation activity as the one seen in ULIRG, followed by an AGN phase. The final product of this merger would be a classical elliptical galaxy (Toomre & Toomre 1972, Toomre 1977, Barnes 1992). Hopkins et al. (2006) investigate this scenario in detail based on isolated hydrodynamical simulations. They show that massive inflows toward the galaxy center occur during the final coalescence of two galaxies. These inflows trigger a burst of star-formation similar to the ULIRG ones, associated to the gas accretion over the black hole at the Eddington rate. The gas is quickly consumed by the starburst phase and the AGN disperses the residual gas. This decay occurs on few hundred million years timescale. This scenario explains the formation of a quiescent galaxy and the short timescale of such quenching is consistent with the presence of a bimodality in color. Interestingly, the major merger is able to quench the galaxy just by the rapid gas consumption, even in the absence of the QSO phase (Fig.19 of Hopkins et al. 2008b). But in the semi-analytical model by Cattaneo et al. (2013), it appears that the SFR is still maintained at a high value at $z > 1$ even after a major merger event (their Fig.6), because of the high gas accretion rate at such early epochs.

In Hopkins et al. (2008a, 2008b), they show that mergers could statistically explain the formation of quiescent galaxies. They first assume that a major merger between two disky galaxies leads to the formation of a quenched spheroid. In order to get a statistical view, they start with a DM halo and sub-halo mass functions that they populate with a Halo Occupation Distribution (HOD) model. Assuming a merging timescale between the galaxies within one halo, they predict a merger rate as a function of mass, cosmic time, environment. By adopting such recipes, they show that: 1) they can produce a significant fraction of quenched galaxies at $z > 3$; 2) they can quench galaxies in halos

less massive than $10^{12}\mathcal{M}_{\odot}$; 3) they can reproduce the GSMF of quenched galaxies with a roughly correct shape.

One difficulty of such "bright-quenching" mode is to keep the central galaxy in massive halos from accreting new cold gas, which could rejuvenate the star formation later. Indeed, the black hole accretes at the Eddington rate over the Salpeter timescale ($t_S \sim 10^{7.5} yr$). Since the mass accretion increases with the halo mass and the redshift, new cold gas could feed again the central galaxy, especially the most massive halos in the early Universe.

5.2.2 The hot-halo mode and radio AGN feedback

Hydrodynamical simulations predict the formation of a quasi-stable, pressure-supported hot gas halo for DM halos more massive than the critical mass $M_c = 10^{12}\mathcal{M}_{\odot}$. It happens in massive halos since the cooling-time becomes longer than the free-fall time. The new accreted gas will shock against the pressure supported structure. At $z > 2$, Cattaneo et al. (2013) assume a larger critical mass M_c since the galaxy is fed by cold gas streams (Dekel et al. 2009).

In these massive halos, the gas could be maintained hot with the energy released by a radio-AGN, which is the quenching process proposed in numerous simulations (e.g. Croton et al. 2006). Even if the "radio mode" is less energetic than the "bright" mode, the radio jet from the black hole is sufficient to prevent the gas to cool in quasi-hydrostatic shock-heated halos (Cattaneo et al. 2006, Somerville et al. 2008). These massive black holes accreting at a low-Eddington rate can maintain the gas hot over the Hubble time. Therefore, this quenching mode is extremely important to prevent the star formation of recurring in the central galaxies of the massive halos. Moreover, the star formation is shut down in the galaxy hosting the AGN, but also in all the satellite galaxies surrounding the AGN.

A first success of this hot-halo mode is to explain the presence of a color-bimodality as shown in Cattaneo et al. (2006). Indeed, the quenching occurs on a short timescale (instantaneous in the Cattaneo et al. model, less than 1Gyr in the Gabor et al. model, private communication). Therefore, galaxies are transferred sufficiently rapidly to create a bimodality in color. A second success of this method is to explain the shape the GSMF and to solve the long-standing problem of over-cooling. At high redshift $z > 3-4$, the galaxies are fed by cold gas streams and grow efficiently through star-formation. When the DM halo grows above $M_H > 10^{12}\mathcal{M}_{\odot}$, the fraction of hot gas increases rapidly and the star-formation is suppressed. While the DM halo is still growing, the galaxy is quenched and does not grow anymore through the gas accretion channel, which explains the different shape of the stellar mass galaxy GSMF and the DM halo mass function. Given a stellar mass to halo mass ratio which seems invariant along cosmic time (e.g. Coupon et al. 2015), it means that the galaxy will always be quenched around the same DM halo mass, explaining the constancy of the $\mathcal{M}_{\star}^{*}$ value for the star-forming and quiescent GSMF.

5.2.3 Mixing merger and hot-halo mode

One difficulty of the "hot-halo" mode quenching is that it does not link naturally the quenching with the morphology while data shows that the morphological transformation into spheroid is associated to the quenching (see §5.4). Moreover, Hopkins et al. (2008b) claim that a classical spheroid can not be formed without a major merger occurring. They underline that the radio-AGN mode requires first the existence of a spheroid and a massive black-hole, i.e. a merger phase. Hopkins et al. (2008b) propose a mixed scenario in which mergers create first the massive black-hole and spheroid. The star-formation can be quenched for several Gyr in halo $M_H < 10^{12}\mathcal{M}_\odot$ with the gas shock-heated by the merger dynamics and the star-formation outflows. Then, several Gyr later, the DM halo grows above $M_H > 10^{12}\mathcal{M}_\odot$ and enters in a hot-mode phase. Therefore, the product of the merger will be naturally quenched. If the merger occurs in a halo more massive than $M_H > 10^{12}\mathcal{M}_\odot$, the quenching by the hot-halo mode is also immediately efficient.

Using a SAM, Cattaneo et al. (2013) investigate the most relevant processes in the stellar mass growth of the present-day quiescent galaxies and quantify the importance of major-merger versus "hot-halo" quenching. They predict that most of the stellar mass is built through efficient star-formation at $z > 2-3$. Quenching by the hot-halo mode occurs before a major merger in most of the cases. They claim that major mergers are dominant to explain quenching only at $z < 1$ and for $\mathcal{M}_\star < 10^{10.8}\mathcal{M}_\odot$ galaxies.

5.2.4 Quenching along the galaxy secular evolution

In the last few years, the discovery that only 1/3 of the massive star-forming galaxies at $z \sim 2$ were mergers and 1/3 were rotating spirals (the other 1/3 can not be classified) shows that the really high SFR at high redshift is not powered by merger but by an extremely efficient gas accretion (Förster-Schreiber et al. 2009). Indeed, galaxies at $z > 1$ contain much more gas than the local ones (Daddi et al. 2007, Tacconi et al. 2010). The high gas fraction in these high-z galaxies has a direct implication: violent disk instabilities in an isolated gas rich galaxy could generate massive clumps and lead to the formation of a bulge (Bournaud et al. 2013). Such galaxies would appear as irregular in Hubble Space Telescope (HST) images while they could be rotating disks (Förster-Schreiber et al. 2009, Genzel et al. 2014). Genzel et al. (2015) find a central AGN in the nucleus of these $z \sim 2$ galaxies, which could quench the star-formation in the central part of the galaxy. Moreover, the disk could become stable against fragmentation as a result of the spheroid growth, even if the gas accretion continues. It could turn the galaxy into a red and dead spheroid by "morphological quenching" (Martig et al. 2009). Therefore, a second channel could possibly explain the formation of quenched and bulge dominated galaxies without involving merging. Hopkins et al. (2008b) underline that disk instabilities do not produce spheroid with the same properties as classical ellipticals (for instance in term of light profile, or rotation properties).

5.2.5 Environmental effects

Numerous processes could affect the star formation efficiency of satellite galaxies as:

- ram pressure stripping (Gunn & Gott 1972), i.e. the hot gas within the halo applies a pressure over the interstellar medium present within the satellite galaxies;
- tidal stripping (e.g. Dekel 2003) and harassment (e.g. Farouki & Shapiro 1981) where several encounters with other galaxies disrupt the satellites ;
- strangulation (e.g. Larson 1980) in which the satellite galaxy which is not anymore at the center of the DM halo is not fueled anymore by cold gas;

Using the group catalogue of the SDSS, Peng et al. (2012) show that the satellite quenching efficiency[1] does not depend on the stellar mass but strongly on the environment. They claim that the DM halo mass has little impact on the environment-quenching and the location of the satellite galaxies inferred from the density contrast is the determinant parameter. Gabor et al. (2015) reproduce the same trend with a halo quenching process in their hydrodynamical simulation, mainly driven by the starving of the galaxies falling in a halo more massive than $10^{12}\mathcal{M}_{\odot}$. In such a case, the halo mass is the determinant parameter. Satellite galaxies are often located in halos more massive than $M_H > 10^{12}\mathcal{M}_{\odot}$ and are therefore located in a hot gas environment. They could be of any stellar mass and then could be quenched.

5.3 Observational constraint from the evolution of the GSMF

The GSMF evolution of the quiescent galaxies characterizes directly at which rate these galaxies are created. Such an observable is fundamental to get a global view on how quenching operates, even if it does not allow us to differentiate between the various quenching channels. Since the quenching rate measures the fraction of star-forming galaxies which are quenched in a given timescale (e.g. Boissier et al. 2010), the study of the quiescent galaxies should go along with the study of the star-forming galaxies. We need to characterize the "reservoir " of galaxies which could potentially quench if we want to interpret the evolution of the quiescent GSMF.

Measuring the GSMF requires accurate redshifts for the quiescent galaxies which are extremely faint in optical. 50% of the $\mathcal{M}^*$ quiescent galaxies at $z > 1$ are already fainter than $i^+ > 24$, i.e. at the limit of massive spectroscopic surveys for 8m class telescopes. Indeed, not more than ten spectroscopic redshifts of quiescent galaxies have been obtained at $z > 2$ (Kronager et al. 2014). While several estimates of the quiescent GSMF based on deep spectroscopic surveys exists at $z < 1.5$ (e.g. Pozzetti et al. 2009, Davidzon et al.

[1] the fraction of red satellite minus the fraction of central red galaxies and renormalized by the galaxy which could be potentially quenched (the blue central fraction)

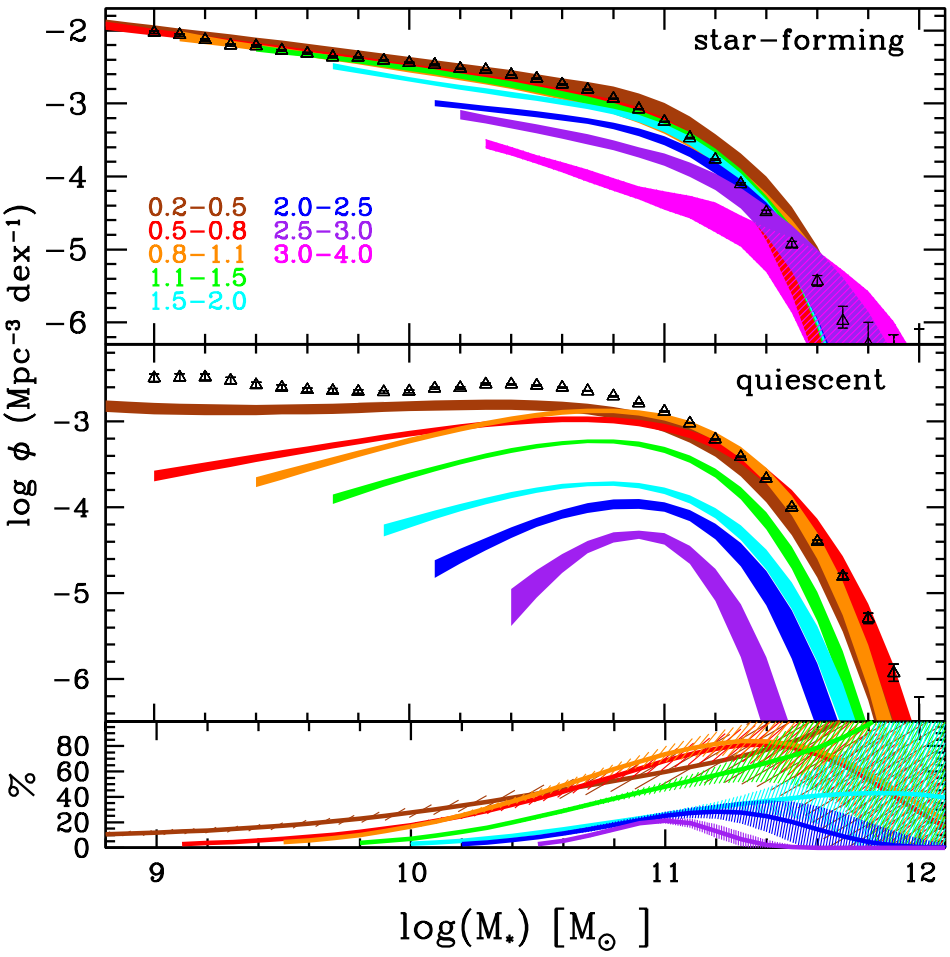

Figure 5.2: Galaxy stellar mass function up to $z = 4$ for the star-forming population (top panel) and for the quiescent population (middle panel). The bottom panel shows the percentage of quiescent galaxies as a function of stellar mass in the same redshift bins.

2013), all the measurements at $z > 1.5$ are based on photometric redshifts. Since quiescent galaxies are rare at $z > 1.5$, their study requires a large area coverage (degree scale survey) and deep NIR data.

In the last decade, several surveys have been able to push the GSMF measurement of quiescent and star-forming galaxies at $z = 2$ and above. Cirasuolo et al. (2007) and Arnouts et al. (2007) measured the evolution of the K-band luminosity function per type out to $z = 2$ using the UKIDSS Deep Survey and the VVDS-SWIRE data, respectively. Ilbert et al. (2010) measured the GSMF of the quiescent and star-forming galaxies out to $z = 2$ with the Spitzer-COSMOS data (Sanders et al. 2007) based on 200,000 galaxies selected at $3.6\mu m$. In the last five years, numerous studies of the quiescent GSMF evolution have been published: Kajisawa et al. (2011) in the MOIRCS Deep Survey out to $z = 2.5$, Brammer et al. (2011) with the NEWFIRM Medium-Band Survey out to $z = 2.2$, Ilbert

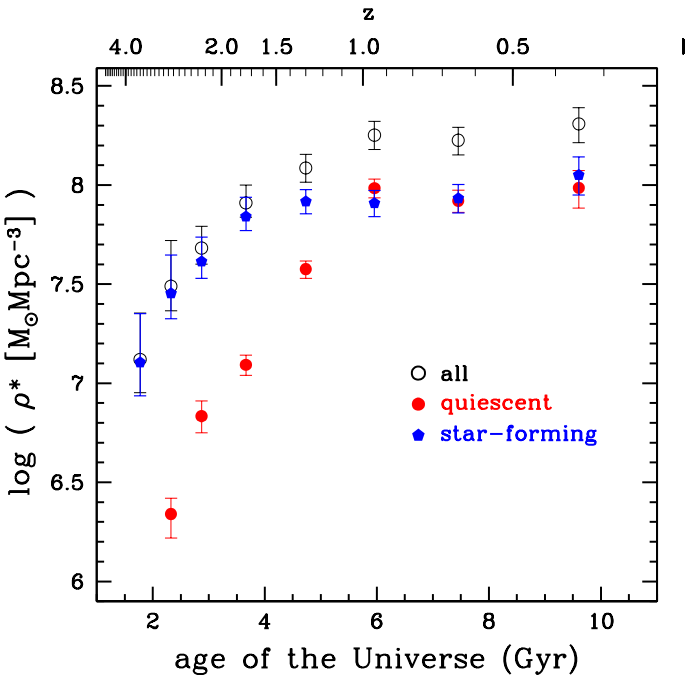

Figure 5.3: Stellar mass density as a function of cosmic time. Black open circles, red solid circles and blue pentagons correspond to the full, quiescent and star-forming galaxies, respectively.

et al. (2013) and Muzzin et al. (2013) out to $z = 4$ using UltraVISTA data, Tomczac et al. (2014) with the ZFOURGE survey out to $z = 3$. I will present our own results from Ilbert et al. (2013). It confirms and extends out to $z = 4$ our results from Ilbert et al. (2010).

5.3.1 The evolution of the quiescent and star-forming galaxies

In Ilbert et al. (2013), we present the stellar mass assembly out to $z = 4$ with a unique sample of 220,000 galaxies selected at $K_s < 24$ in the COSMOS field. Galaxies are selected using the UltraVISTA DR1 near-infrared data release over an effective area of 1.52 deg^2. The photometric redshifts associated to this catalogue are discussed in chapter 2. We isolate the quiescent population using a classification based on the rest-frame colors $NUV - r^+$ and $r^+ - J$ described in section.5.1. The GSMF is derived with our dedicated tool ALF (Ilbert et al. 2005).

Figure 5.2 shows the mass functions of the star-forming galaxies (top panel) and quiescent galaxies (middle panel). The contribution of the quiescent galaxies to the full population is indicated in the bottom panel.

Below $z < 1$, two well known trends are immediately observable:

- the quiescent galaxies are the most massive galaxies at $z < 1$. Above $10^{11}\mathcal{M}_\odot$, half of the galaxies are quiescent;

- the slope of the star-forming GSMF is steeper than the slope of the quiescent population, with $\alpha \sim -1.4$ for the star-forming galaxies while α could be positive for the quiescent population.

The GSMF evolution of the quiescent population is clearly mass dependent at $z < 1$. In this redshift range, we do not find any significant evolution of the high-mass end by more than 0.2 dex, while we observe a clear flattening of the faint-end slope. Between $0.8 < z < 1.1$ and $0.2 < z < 0.5$, the density of galaxies more massive than $10^{11.2}\mathcal{M}_{\odot}$ does not increase, while galaxies are continuously "quenched" at the low-mass end. For instance, the density of $10^{9.5}\mathcal{M}_{\odot}$ galaxies increases by a factor of > 5 between $0.8 < z < 1.1$ and $0.2 < z < 0.5$. While the same downsizing pattern is found for the quiescent galaxies in Moutard et al. (2015) over 25 deg^2, such a covered area allows to study with an unprecedent precision the most massive galaxies. Moutard et al. (2015) show a density evolution by ~ 0.25 dex of the most massive ($\mathcal{M}_{\star} > 10^{11.5}\mathcal{M}_{\odot}$) quiescent galaxies between ~ 1 and $z \sim 0.2$, allowing for additional mass assembly via dry mergers.

In contrast with the result at $z < 1$, the density of the quiescent galaxies decreases rapidly at higher redshift and the evolution is not anymore mass dependent. The density of $10^{11}\mathcal{M}_{\odot}$ quiescent galaxies increases by 1.4 dex (factor 25) between $2.5 < z < 3$ and $0.8 < z < 1.1$. The normalization parameter Φ_1^* increases continuously between $z \sim 3$ and $z \sim 1$. However, these numbers are still debated. Brammer et al. (2011) find a smooth evolution from $z \sim 2$ to $z \sim 0.1$ with an increase of 0.5 dex/Gyr. The situation at $z > 2$ is even worse since the capacity to select the quiescent galaxies is degraded by the quality of the photo-z and the noise in the rest-frame colors. At $z > 3$, no robust quiescent galaxy sample has been built yet. Figure 5.3 shows the evolution of the stellar mass density for the quiescent population. The stellar mass density increases by 1.6 dex between $2.5 < z < 3$ and $0.8 < z < 1.1$. Again, we find a change of regime around $z \sim 1$ with the mass assembly slowing down. We find that the stellar mass assembly is faster at $1 < z < 3$ for the quiescent population than for the global population which evolves by 0.8 dex in the same redshift range.

The top panel of Fig.5.2 shows the GSMF of the star-forming galaxies. This GSMF is almost not evolving at $z < 1$. Such a result has been already discussed in the literature (e.g. Arnouts et al. 2007). It has been also confirmed on much larger fields exceeding 10 deg^2 (Davidzon et al. 2013, Moustakas et al. 2013, Moutard et al. 2015). By definition, the star-forming galaxies are forming new stars and should grow in mass. Moreover, we do not detect an evolution of the density of the most massive galaxies $10^{11.6-11.8}\mathcal{M}_{\odot}$ from $z = 0.2$ out to $z = 4$. Therefore, these massive star-forming galaxies are necessarily quenched along cosmic time.

5.3.2 Mass quenching and environment quenching

One of the striking results from several analyses is that the star-forming GSMF does not evolve below $z < 1$ and that the characteristic M^* stays almost constant, at least at $z < 2$. Therefore, star-forming galaxies are quenched continuously along cosmic time at a rate

which compensates their growth in mass (Arnouts et al. 2007). Boissier et al. (2010) and Peng et al. (2010) use this result to constrain the quenching rate.

Peng et al. (2010) show that the differential evolution of the quenched fraction is separable in stellar mass and environment, suggesting two different processes: "mass quenching" and "environment quenching". A major point of the paper from Peng et al. is to show that the environmental quenching efficiency[2] does not depend on the mass and that the mass quenching efficiency does not depend on the environment. These results are based on the SDSS and the zCOSMOS spectroscopic samples. While the "purely empirical analytical model" from Peng et al. (2010) does not allow to determine the physical processes acting in the quenching, such a model is extremely useful to understand at which rate galaxies are transferred from the star-forming to the quiescent population at a given mass and in a given environment. Hereafter, we explain in more detail how the mass quenching and the environment quenching were used by Peng et al. (2010) to interpret the evolution of our GSMF.

Mass quenching

If the quenching process was acting with the same efficiency at all masses, the GSMF of the quiescent population should have the same slope as the star-forming GSMF. We conclude that the physical process that quenches the star formation is mass dependent and necessarily more efficient above $\mathcal{M}_\star \gtrsim 10^{10.7-10.9}\mathcal{M}_\odot$, i.e. the maximum in density of the quiescent GSMF. The mass quenching of Peng et al. (2010) could occur for an isolated galaxy without any merger. In their model, the mass quenching rate (fraction of galaxies which are quenched per unit of time) is found to be directly proportional to the SFR, $\lambda_m = \mu \times \mathrm{SFR}$. They obtained this result by starting with the very simple case in which the GSMF of the star-forming galaxies is not evolving. In such a case, the number of blue galaxies per unit logarithmic mass does not change with time:

$$\frac{dN_B}{dt} = -N_B\lambda_m - N_B(\alpha+\beta)s\mathrm{SFR} = 0 \tag{5.1}$$

with $\alpha = \frac{logN_B}{log\mathcal{M}_\star}$ and β is the slope of the sSFR versus mass relation. λ_m is the death function, .i.e. the probability that the galaxy quenches whatever the reason (mass quenching, merger, ...). In the case of a Schechter function with a slope α_S, $\alpha = 1 + \alpha_S - \frac{\mathcal{M}_\star}{\mathcal{M}_\star{}^*}$ with $\mathcal{M}_\star{}^*$ being the characteristic mass of the GSMF. It means that the quenching rate λ_m is

$$\lambda_m = -(1 + \alpha_S - \frac{\mathcal{M}_\star}{\mathcal{M}_\star{}^*})s\mathrm{SFR} \tag{5.2}$$

[2]The difference between the red fraction in the considered environment and in the lowest density environment, renormalized by the fraction of blue in this lowest density environment. The measurement is done at a given mass. With such a definition, if the evolution of the red fraction in dense environment is small, but that the fraction of blue in underdense environment is also small, the efficiency could stay high.

At high masses ($\mathcal{M}_\star > \mathcal{M}_\star{}^*$), $\lambda = \frac{\mathcal{M}_\star}{\mathcal{M}_\star{}^*}$sSFR $= \frac{SFR}{\mathcal{M}_\star{}^*}$. So, to maintain the same $\mathcal{M}_\star{}^*$ at all redshifts for the star-forming GSMF, we need to quench proportionally to the SFR. Using the value of $\mathcal{M}_\star{}^*$ around $10^{10.6}\mathcal{M}_\odot$, Peng et al. obtained $\lambda_m = \frac{SFR}{40\mathcal{M}_\odot yr^{-1}} Gyr^{-1}$. So, if any mechanism is creating a mass quenching rate directly proportional to the SFR, it will generate a Schechter function with a constant characteristic stellar mass. Since $\lambda_m \propto$ SFR and that the SFR $\propto \mathcal{M}_\star{}^{\beta+1}$, we have $\lambda_m \propto \mathcal{M}_\star{}^{\beta+1}$. By taking the Schechter function of the blue galaxies and applying a quenching rate proportional to $\mathcal{M}_\star{}^{\beta+1}$, they obtain a difference of slopes between the star-forming and quiescent population which is $\alpha_{star-forming} + 1 = \alpha_{quiescent}$. So, this formalism explains also the difference in slope between the two populations.

Environment quenching

Peng et al. (2010) propose the "environment quenching" process which mainly affects the satellite galaxies as large-scale structure develops. They showed that the environment quenching efficiency remains the same in all the redshift bins defined in zCosmos: the capacity to quench a galaxy in a given environment remains the same, independently of the galaxy mass or the considered epoch. But since the structures develop along cosmic time, the galaxies migrate toward an environment which become denser and denser. Therefore, while the environment quenching efficiency remains the same along cosmic time, the fraction of galaxies quenched through "environment quenching" increases with time. By considering that this quenching affects the satellites, Peng et al. showed that they expect between 40% to 75% (in the highest density environment) to be quenched when they fall into larger DM halos. Ram pressure and strangulation are possible mechanisms for satellite quenching.

By taking into account the environment quenching, which does not depend on the mass, we would naturally create a second component to the Schechter function of the quiescent galaxies with a slope similar to the slope of the star-forming galaxies. The combination of mass and environment quenching explains the two Schechter components of the quiescent GSMF.

Schematic view

In Ilbert et al. (2013), we summarized our interpretation of the building of the quiescent population with Fig.5.4. The GSMF shown in this figure correspond to our best-fit Schechter functions with the UltraVISTA data. As shown in the left panel of Fig.5.4, the star-forming population dominates the galaxy population at high redshift. Therefore, a mass quenching process could rapidly build the quiescent population. Because of the really high value of the sSFR at $z > 1$, the "reservoir" of massive star-forming galaxies will be replenished rapidly. If the quenching process depletes more rapidly the reservoir of massive star-forming galaxies than new star formation is able to replenish it, we reach an epoch where the quenching is no longer a channel to create new massive quiescent

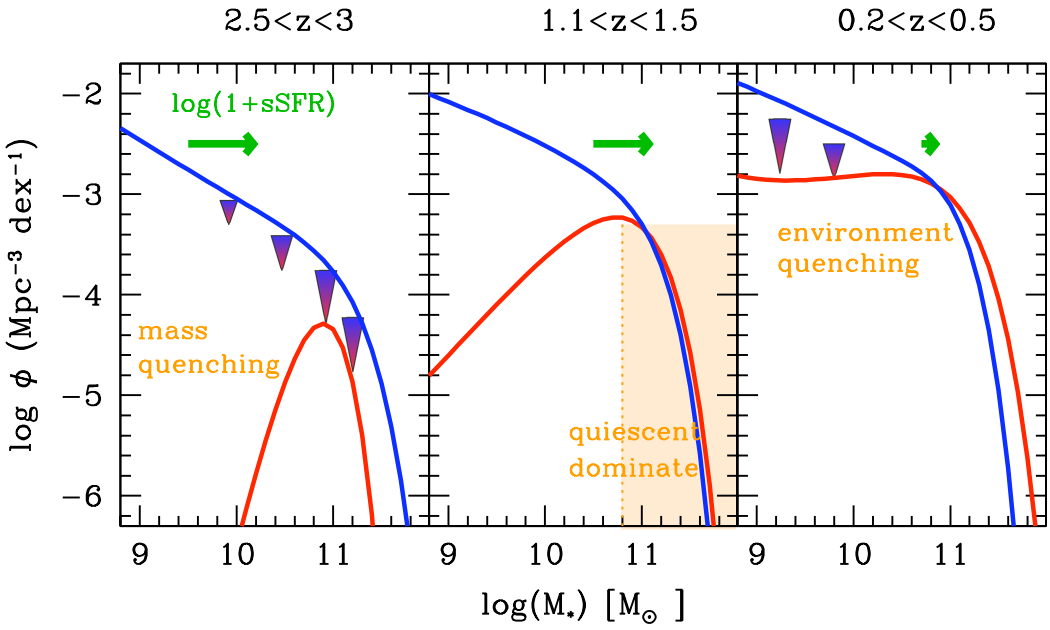

Figure 5.4: A possible scenario showing how *s*SFR and quenching impact the star-forming GSMF (blue lines) and quiescent GSMF (red lines), similar to Peng et al. (2010). The large arrows represent quenching. The green arrows correspond to the mass increase expected in 2 Gyr, by taking the *s*SFR values compiled by Stark et al. (2013). The left panel corresponds to the high redshift bin $2.5 < z < 3$, where we show the mass quenching process which is more efficient at high mass. The middle panel corresponds to the redshift bin $1.1 < z < 1.5$ when the quiescent galaxies starts to dominate the high-mass end. The right panel corresponds to the redshift bin $0.2 < z < 0.5$, when environment quenching generates new low mass quiescent galaxies.

galaxies. The *s*SFR estimated from the literature decreases by a factor 15 between $z \sim 1.5$ and $z \sim 0.6$ as shown by the green arrows in Fig.5.4 (see chapter 3). Therefore, it becomes much more difficult to replenish the reservoir of massive star-forming galaxies at $z < 1$. By $z \sim 1$ the supply of massive star forming galaxies has dwindled to the point that few new galaxies can be quenched. Figure 5.2 shows that $> 70\%$ of the galaxies more massive than $\mathcal{M}_\star > 10^{11}\mathcal{M}_\odot$ are quiescent at $z < 1.1$. Since the massive galaxy population is already dominated by quiescent galaxies at $z < 1$ and since the growth rate of star-forming galaxies is no longer sufficiently efficient to generate numerous massive star-forming galaxies (middle panel of Fig.5.4), the quenching of massive star-forming galaxies can not modify significantly the high-mass end of the quiescent GSMF at $z < 1$. Most of the evolution at

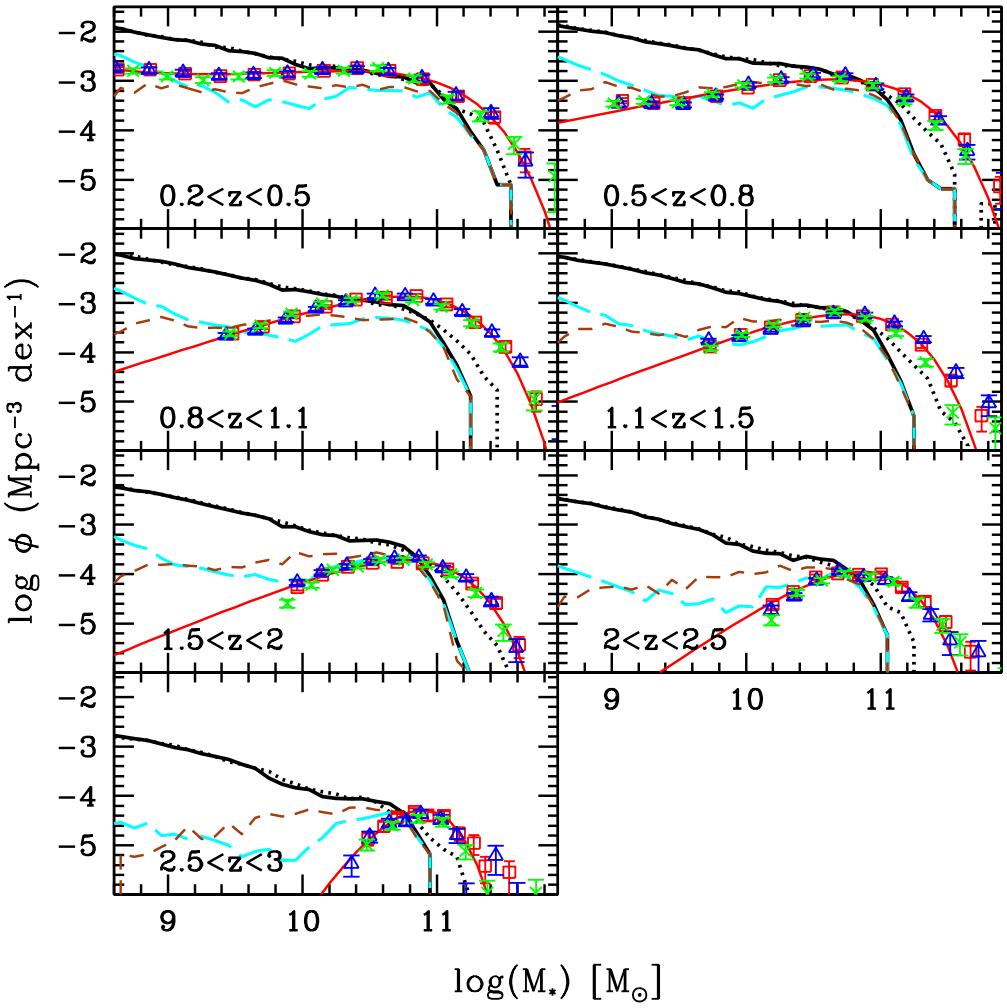

Figure 5.5: Galaxy stellar mass functions of the quiescent sample for selected using a two-color technique for different assumptions in the SEDs (points). The black solid lines correspond to the prediction of the SAM. The long dashed cyan lines correspond to the central galaxies in the models.

$z < 1$ is now driven by the mass quenching for intermediate mass galaxies and environment quenching for the low mass ones (right panel). As shown by Bezanson et al. (2012), such a flattening of the slope is easily obtained by quenching a small fraction (between 1 and 10%) of the star-forming galaxies. Still, an evolution of the most massive quiescent galaxies is still possible by the dry-merging channel (Faber et al. 2007, Moutard et al. 2015).

5.3.3 Comparison with galaxy formation models

We compared our GSMF measurements with the predictions of semi-analytical models for the quiescent galaxies. The mock catalogs are based on ΛCDM simulations from Wang et al. (2008) with the cosmological parameters derived from the third-year WMAP data (H_0 = 74.3 km/s, Ω_M = 0.226 and Ω_Λ = 0.774). The light cone survey covers an area of 1.4×1.4 deg^2 similar to COSMOS. Galaxy properties were generated using the galaxy formation model, as detailed in De Lucia & Blaizot (2007) and Wang & White (2008). Since the redshift and the galaxy stellar masses are available for all galaxies in the simulation, we can directly compute the predicted GSMFs. We used our standard cosmology (H_0 = 70 km/s, Ω_M = 0.3 and Ω_Λ = 0.7) to renormalise the predicted stellar mass counts by the comoving volume. We isolated the quiescent population in the simulations. Figure 5.5 shows the comparison between observed and predicted GSMFs for the quiescent population. The mismatch between the observed and predicted faint end slopes is dramatic. At $9.5 < log(\mathcal{M}) < 10$ and $0.5 < z < 0.8$, the model overestimates the low-mass end by a factor 10. Such an effect has been already noticed by Cucciati et al. (2012b) in the VVDS field based on the B-band luminosity function. Wang & White (2008), Bielby et al. (2012), Bower et al. (2012), Guo et al. (2011) showed that the models overproduce the density of low-mass galaxies for the full population. Information such as the host halo mass, the galaxy location in the halo (central or satellite) and the galaxy morphology are kept in the simulation. It appears that the low-mass quiescent simulated galaxies are mostly dominated by satellite/orphans galaxies. One possible interpretation of the mismatch between the faint-end slopes is an over-quenching of the star-formation in satellite galaxies and/or an over-quenching of the star-formation in disk galaxies.

In the last few years, this problem has been investigated in several SAMs. Henriques et al. (2015) obtain better results in reproducing the low-mass end slope of the quiescent GSMF, by adding a delay in the reincorporation of supernovae wind ejecta, by keeping ram-pressure stripping only in the most massive halos ($> 10^{14}\mathcal{M}_\odot$), and by modifying the radio-mode feedback. Their predictions improve the situation but the number of low-mass quiescent galaxies is still overpredicted, as shown in Fig.7 of Henriques et al. (2015).

5.4 Link with the morphology

Since decades, we know that the massive elliptical galaxies are also quiescent in the local Universe, which is true even at intermediate redshift (e.g. Cassata et al. 2007, Bell et al. 2008). Therefore, the process of quenching affects the same population as the one enduring a morphological transformation. But what is the physical property acquired first: elliptical morphology or quiescence? Such an information could inform us on the process responsible of the formation of red elliptical galaxies (e.g. Abraham et al. 2007). Depending on the processes which are the most relevant, or the ones occurring first, we do not expect the same evolution of the quiescent and/or elliptical galaxies. For instance, we could quantify what is coming first between mergers and hot-halo quenching. In Ilbert

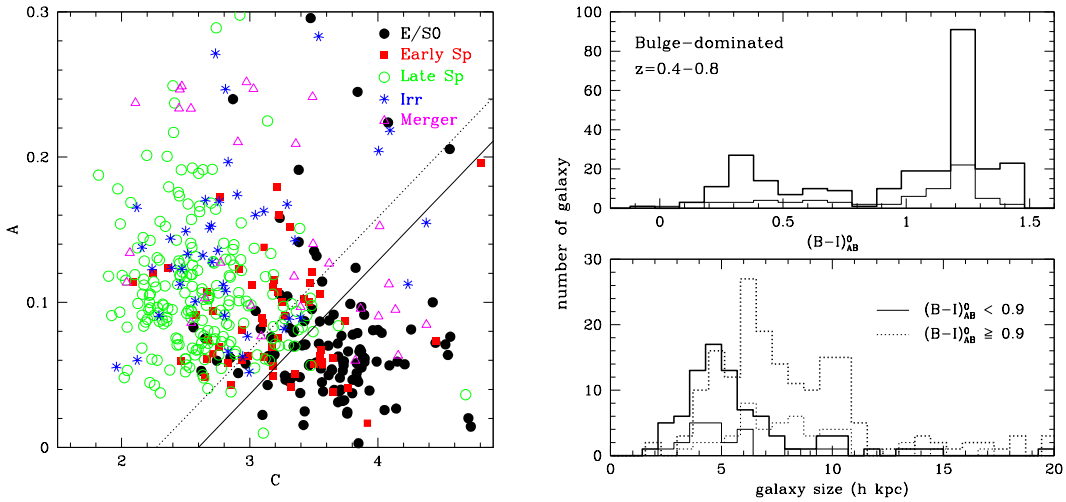

Figure 5.6: Left: distribution in the A-C diagram of visually classified galaxies in GOODS-S. The solid circles correspond to galaxies visually classified as elliptical-S0, the solid squares to early spirals, the open circles to late spirals, the star to irregulars and open triangles to mergers. The solid line is the empirical criterion A = 0.0917 C-0.2383 we have adopted in Ilbert et al. (2006) to separate bulge- and disk-dominated populations. Right top panel: the distribution of the $(B-I)^0_{\rm AB}$ rest-frame colors for the bulge-dominated population. Right bottom panel: galaxy size distribution for the red bulge-dominated population (dotted line) and for the blue bulge-dominated population (solid line). For both panels, the thick lines correspond to the photometric redshift sample and the thin lines to the spectroscopic redshift sample.

et al. (2006) and Ilbert et al. (2010), we combine the morphology and the star formation indicators to study this problem. These two studies were based on ACS/HST images. We restricted our analysis to $z < 1.4$ since we were not able quantify the impact of the morphological k-correction[3] on our classification.

The morphological classification

Such a work relies on our ability to separate high redshift galaxies into different morphological classes. Automatic morphological classifications (e.g. Abraham et al. 1996) performed on high resolution images are efficient for discriminating at least two robust classes: E/S0 and Spi/Irr galaxies (e.g. Lauger et al. 2005, Menanteau et al. 2006, Lotz et al. 2008, Capak et al. 2007). Several methods have been developed to automatically classify galaxies according to their concentration, asymmetry or gini parameters (e.g. Abraham et al. 1996, Conselice et al. 2000, Lotz et al. 2008). The concentration of light

[3]the reddest ACS band is sampling the UV rest-frame at $z > 1.4$ while it samples the optical rest-frame at lower redshift.

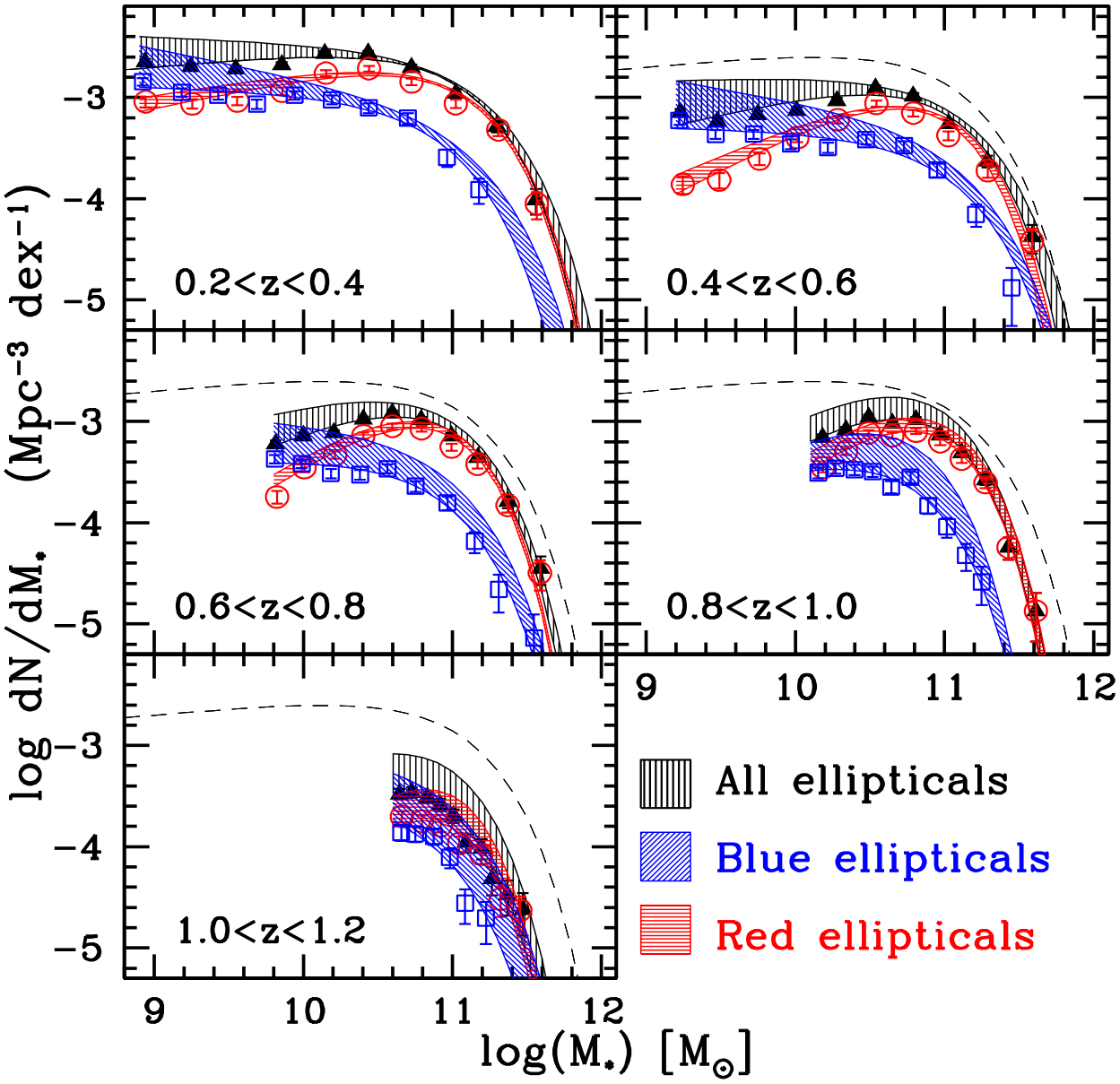

Figure 5.7: GSMF of elliptical galaxies selected in morphology without any cut in color (black vertical shaded area). The blue oblique shaded areas and the horizontal red shaded areas are the GSMFs of the blue and red elliptical galaxies, respectively. The upper and lower envelope GSMFs are obtained using two different morphological classifications, respectively. For clarity in the figure, the non-parametric estimates are shown only for one classification. The dashed line is the GSMF of elliptical galaxies derived at $z = 0.2 - 0.4$, which is shown in each redshift bin to serve as a reference.

is defined as the ratio between the radii which contain 80 % and 20 % of the total flux of the galaxy, respectively. The asymmetry is obtained by computing the difference pixel per pixel of the original image and of its 180° rotation. The gini parameter measures the inequality with which the light of a galaxy is distributed among its constituent pixels.

The advantage of an automatic classification is that it is quantitative and reproducible. In Ilbert et al. (2006), we used a galaxy sample that we visually classified to establish a limit in the asymmetry-concentration plane to split the sample into bulge and disk dominated galaxies (see Fig.5.6) based on the ACS data in the GOODS-S field (Giavalisco et al. 2004). In Ilbert et al. (2010), we used the high resolution HST/ACS images over 1.4 deg^2 (Koekemoer et al. 2007) to perform a morphological classification of our COSMOS sample. We used two automatic classifications in order to obtain an estimate of the systematic uncertainties associated to our classification. Having now classifications in hand, we compute the GSMF by combining several combinations between star-forming/quiescent galaxies and bulge-/disk-dominated galaxies. The results are shown in Fig.5.7 and Fig.5.8. In the following, we discuss the evolution of each combination.

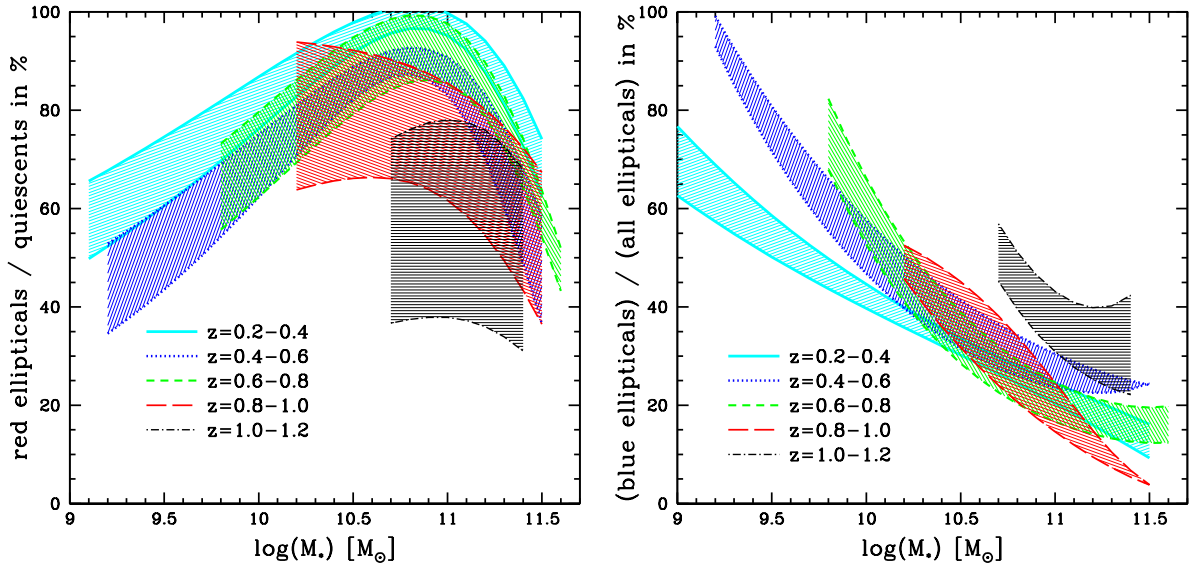

Figure 5.8: **Left:** Fraction (in %) of "quiescent" galaxies with a bulge-dominated morphology. The fraction is obtained by dividing the GSMF of the red ellipticals by the GSMF of the quiescent galaxies. The upper and lower limits are obtained using two different morphological classifications, respectively. **Right:** Fraction (in %) of blue galaxies in the elliptical sample (morphologically selected).

The red and dead elliptical galaxies

The fraction of elliptical galaxies among the quiescent population is shown in Fig.5.8. At high mass, $log(M) \sim 11$ and $z < 0.8$, the fraction of quiescent galaxies with an elliptical morphology is greater than 80-90% depending on the classification. The fraction of massive quiescent galaxies with an elliptical morphology decreases at $z > 0.8$. For both classifications, we conclude that the majority of the red and dead massive elliptical galaxies were already assembled at $z = 0.8$.

The massive quenched disk-dominated galaxies at $z > 0.8$

Fig.5.8 shows also that the fraction of massive quenched galaxies which has not yet acquired an elliptical morphology increases at $z > 0.8$. At high mass, these galaxies could be central galaxies within a hot-gas halo, not fed anymore by cold gas and without having undergone a major merger that could modify their morphology, as expected by Cattaneo et al. (2013). Therefore, there is an hint that the morphological transformation occurs after the quenching, which needs to be better constrained by improving the reliability of the morphological classification at high redshift.

The quenched disk-dominated galaxies at low mass

As shown in Fig.5.8, the fraction of quenched disk/irregular increases continuously toward low masses reaching 40-60% at $log(M) \sim 9.5$. The radio mode prevents star formation from recurring in all the galaxies of massive DM halos. Therefore, the star formation is shut down in the galaxy hosting the AGN, but also in all the galaxies surrounding the AGN, i.e. the satellite galaxies. The shutdown of the star formation in the satellite galaxies does not modify their morphology. As their original morphology can be any, we then expect a dominant population of disk/irregular morphology. The mass distribution of these satellite galaxies follow the ones of the star-forming galaxies (Peng et al. 2010). Therefore, it could explain why we see such an increase of the fraction of quenched galaxies with a disk/irregular morphology at lower masses.

The star-forming bulge-dominated galaxies

Numerical simulations have shown that the final product of a merger between two spiral galaxies leads to the formation of a spheroid (e.g. Barnes 1992). The "blue elliptical" galaxies could be newly formed elliptical galaxies still consuming the gas of their progenitors (e.g. Van Dokkum & Franx 2001). The combination of morphological and spectral classifications allow us to isolate the "blue elliptical" galaxies (e.g. Cross et al. 2004, Menanteau et al. 2006, Ilbert et al. 2006, Ilbert et al. 2010). Figure 5.7 shows the blue elliptical GSMF. Its shape differs from those of the red elliptical galaxies: the slope is steeper and the exponential cutoff is shifted to lower mass. As a consequence of

this different shape, the contribution of the blue elliptical galaxies to the total elliptical population depends strongly on stellar mass. Regardless of redshift, the fraction of blue ellipticals decreases toward high mass systems. The blue elliptical galaxies represent less than 20 % of the massive elliptical galaxies (at $log(M) > 11$ and $z < 1$), but their contribution reaches 40-60 % at $log(M) \sim 10$. Figure 5.6 shows the galaxy size distribution for blue and red bulge-dominated galaxies measured in Ilbert et al. (2006). The blue population, with an average size of $5.8h$kpc is more compact than the red population with an average size of $8.2h$kpc.

The nature of this population remains unclear. Mergers expected in the hierarchical scenario could create a burst of star formation explaining the blue color of these galaxies. We observed some signs of disruption for a significant fraction of these galaxies. If major mergers explain the presence of this population, they occur more often at low mass at $z < 1$ given the mass distribution of this population. These galaxies could be also a dwarf population undergoing a strong burst of star formation in the galaxy core, which could be interpreted as a bulge component (Im et al. 2001).

5.5 Summary

The quenching of the star formation is a crucial event in galaxy evolution: 1) it suppresses the star formation in the most massive galaxies which is necessary to conciliate the DM mass function and stellar mass function; 2) it explains the bimodality in color observed over most of the cosmic time. Most of the massive star-forming galaxies will endure a quenching phase along their history. By knowing in which environment and at which redshift the quenching acts, we bring some constraints on the co-evolution of the galaxies, AGN and their dark matter halos.

This chapter presents one of the most basic constraint on the quenching processes, i.e. the evolution in density of the quiescent galaxies over time. We analyzed the evolution of the quiescent population in two papers (Ilbert et al. 2010, Ilbert et al. 2013), both based on the COSMOS 2-deg^2 field. From $z \sim 3$ to $z \sim 1$ we find a rapid increase in the stellar mass density of all quiescent galaxies, independently of their mass. At such a redshift, a large reservoir of massive galaxies is present and this reservoir is replenished because of the rapid gas accretion rate. Massive quiescent galaxies can be created efficiently. Because of the different faint-end slopes of the GSMF between the quiescent and star-forming populations at $z < 3$, we infer that the physical processes which quench the star formation are more efficient above $\mathcal{M} \gtrsim 10^{10.7-10.9}\mathcal{M}_{\odot}$. This scenario is consistent with the model proposed by Peng et al. (2010) who introduce a "mass quenching" process. The high-mass end of the quiescent GSMF does not evolve by more than 0.2 dex at $z < 1$ according to the COSMOS data, ~ 0.25 dex for the most massive galaxies according to Moutard et al. (2015). A possible interpretation is that: 1) star formation is not efficient enough at $z < 1$ to produce new massive star-forming galaxies, which could be quenched later; 2) major mergers between massive galaxies are not sufficiently frequent at $z < 1$ to increase significantly the density of massive quiescent galaxies. At $z < 1$, we observe a

clear flattening of the low mass-end slope of the quiescent GSMF. Following Peng et al. (2010), we interpret this flattening as an "environment" quenching which impacts satellite galaxies independently of their mass.

Finally, we discuss the importance of combining the quiescent and morphological information. We find that 80-90% of the massive quiescent galaxies ($log(\mathcal{M}) \sim 11$) have an elliptical morphology at $z < 0.8$. Therefore, a dominant mechanism links the shutdown of star formation and the acquisition of an elliptical morphology in massive galaxies. Still, a significant fraction of quiescent galaxies present a Spi/Irr morphology at low mass (40-60% at $log(\mathcal{M}) \sim 9.5$) and at $z > 1$. Such galaxies could be quenched by processes like the "hot halo mode". Morphology could help us to isolate which physical processes are relevant in the quenching.

Chapter 6

Conclusions and perspectives

6.1 Building of the stellar populations across cosmic time

The increase of the SFRD and *s*SFR from the local Universe out to $z \sim 1.5$ is a very well established feature in cosmology. There is a growing idea that such an evolution is driven by an higher cosmological accretion rate at earlier time. Indeed, the baryonic gas falls continuously on the central galaxy at a rate driven by the hierarchical growth of the dark matter structures. As discussed in chapter 4, simple models assuming that the galaxy is in a quasi-equilibrium as well as more complex models (SAM or hydrodynamical simulations) predict that the *s*SFR follows the evolution of the specific mass increase rate of the dark matter halo. But most of the observations are at odd with this prediction (e.g. Weinmann et al. 2011, Tasca et al. 2015). As emphasized in Furlong et al. (2015) using the EAGLE hydrodynamical simulation, one of the most difficult challenge is to conciliate the evolution of the observed *s*SFR and the predicted one. Using a semi-analytical model, Weinmann et al. (2011) concluded that non standard physical recipes need to be included to move away the *s*SFR from the cosmological accretion rate. Therefore, a possibility to explain the mismatch between the observed and predicted *s*SFR evolution is that some important physical processes have been neglected. Therefore, progressing on this topic could potentially bring a crucial information on the galaxy formation processes. But another possibility is that some observational biases are present in the current observations. As observers, we must insure that it is not the case. Indeed, measuring accurate stellar masses and SFR, for complete galaxy samples is not an easy task. In this manuscript, we have use new methods which are complementary to what has been done before and we find that the *s*SFR evolution follows the cosmological accretion rate at odd with the literature.

In a short term, we can progress on the use of the stellar mass functions to trace the *s*SFR evolution, as well as the global SFH following the method described in Chapter 3 (Wilkins et al. 2008, Ilbert et al. 2013). Such a work is the goal of the ANR SAGACE (Pi: O. Ilbert, starting date: September 2014). The difficulty for us is to produce an accurate

census of the GSMF at $z > 3$, which is possible thanks to the ongoing program Spiter-SPLASH (Capak et al. 2015, in prep.). This survey totalizes 3400h with the IRAC camera on-board of the Spitzer telescope, the only instrument that probes the rest frame optical fluxes needed to measure the galaxy stellar masses at $z > 3$. We cover two large fields of 2 deg^2 to get tens of rare and massive galaxies at $z \sim 7-8$, a mass-selected sample of more than a hundred thousand of galaxies at $z > 3$ and exquisite data to secure their distances (Hyper Suprime-Cam in optical and UltraVISTA in near-infrared). In the long term, this method will be amplified at even higher redshift and lower stellar masses with the Near Infrared Camera (NIRCam) on board of the James Web Space Telescope (JWST). The JWST is a 6.5m telescope which should be launched in October 2018. NIRCam is a powerful instrument to acquire deep NIR images (reaching a mag of 28.8 at $2\mu m$ in 10000s exposure over a $2.2' \times 2.2'$ field of view). It will revolutionize our capacity to acquire faint galaxy samples and measure the galaxy physical properties at $z > 6$.

Tremendous progresses can also be done in the next decade using direct SFR tracers to measure the global SFH and the *s*SFR evolution. Stacking analysis are possibly a solution to extend such studies at $z > 3$. In particular, the stacking of 1.4 GHz radio data by Karim et al. (2011) has proved to be extremely efficient to obtain the evolution of the SFRD at $z < 4$ with VLA data. A new program on COSMOS will produce even deeper radio data, the JVLA-COSMOS survey (PI: V. Smolcic) with 0.7" resolution and $2\mu Jy/beam$ sensitivity. The excellent resolution of the radio data compared to the IR data is a key advantage for stacking analysis. In a long term, the Square Kilometer Array (SKA) radio telescope located in South-Africa and Australia will be extremely powerful for this kind of analysis. The star formation will be traced by the radio continuum emission around 1GHz, with the possibility to detect directly main sequence galaxies at $z \sim 3$ over 10 deg^2 and actively star-forming galaxies ($L_{IR} > 10^{12}\mathcal{L}_{\odot}$) at $z > 3$ over 30000 deg^2 (Jarvis et al. 2015). This telescope should be ready for a first phase in 2020 and should be 10 times more sensitive for a second phase in 2025.

In the future, the JWST will be perfect to extend our direct SFR measurement at much lower masses and higher redshift. Indeed, the Mid-Infrared Instrument (MIRI) is as sensitive at $24\mu m$ as is the MIPS/Spitzer camera. Combining MIRI and NIRCam is a key to measure the *s*SFR function at lower masses. But MIRI will not help to go beyond $z > 1.4$ since the $24\mu m$ is a poor tracer of the SFR at higher redshift. The Near-Infrared Spectrograph (NIRSpec) on-board of JWST will be able to get simultaneously 100 spectra covering the wavelength range 0.6 to $5\mu m$. With such an instrument, we will catch Hα out to $z \sim 6$ which will revolutionize our capacity to measure the SFR and *s*SFR at $z > 3-4$. The IFU of MIRI should even be able to catch Hα at $z > 6$. In addition to allow the possibility to establish $H\alpha$ limited samples, such observations will allow to establish how to convert UV into SFR at $z > 4$.

We discussed the perspective for a better characterization of the star formation activity over cosmic time. However, an extremely important piece of the puzzle relies on the characterization of the gas content and on how cold gas feeds galaxies. A huge amount of effort is dedicated to measure the amount of molecular gas in high redshift galaxies using

the rotational transitions of CO (e.g. Tacconi et al. 2013) or using the dust continuum (e.g. Scoville 2012). Such an activity has a bright future with the Atacama Large Millimeter/submillimeter Array (ALMA) observatory. It will be extremely useful to characterize at high redshift the fraction of cold gas present in the galaxies as well as the time depletion timescale (M_{H_2}/SFR) to understand the mechanism triggering the star formation activity. Such studies should be done as a function of galaxy morphology, and position within the cosmic web. We will characterize which mechanisms trigger the star formation activity, e.g. by rapidly filling the gas reservoir at the node of the cosmic web, or by depleting it more efficiently during specific event like a merger.

Finally, mergers between two galaxies represent a crucial piece of information that we did not consider sufficiently in this manuscript, while extremely important when we study the galaxy stellar mass assembly. Mergers contribute significantly to the stellar mass assembly. According to the AGN-horizon hydrodynamical simulation, half of the galaxies are supposed to endure a major merger between $z = 5.2$ and $z = 1.2$, and 45% of the stellar mass has been assembled through major mergers by $z = 1.2$ (Welker et al. 2015). On the observational side, it is difficult to isolate mergers based on high-resolution images at $z > 1$ since they could be easily confused with turbulent disks. Integral Field Units (IFU) are now combined with high resolution images to identify mergers at $z > 1$ (Förster-Schreiber et al. 2009, Contini et al. 2012, Lopez-Sanjuan et al. 2013). The K-band Multi-Object Spectrograph (KMOS) facility at the VLT provides 24 IFUs sensitive in NIR that we can use to establish dynamical maps at $z > 1$ for significantly large mass selected samples. Such data will be extremely useful to quantify the fraction of merger at the peak of the star-formation activity. Another method is based on the fraction of galaxy pairs. Based on simulations, we estimate the fraction of pairs ending into a major merger (Lopez-Sanjuan et al. 2012, 2014). Such a method could be used to characterize how the merger rate depends on the stellar mass (de Ravel et al. 2009) or to study minor mergers (Lopez-Sanjuan et al. 2012). Major mergers are usually supposed to produce elliptical and quenched galaxies, which would moved them into the quiescent population discussed below. Still, it has been shown that a gas rich merger could produce a star-forming disk galaxy (Hopkins et al. 2009), what complexes even more our capacity to describe quantitatively how mergers participate to the building of the Hubble sequence.

6.2 Characterize the processes responsible for the quenching

While the dark matter structures are continuously growing, bringing continuously baryonic matter into the halo, the star formation is halted in the galaxies above $10^{11}\mathcal{M}_{\odot}$ (see chapter 5). This quenching of the star formation is a crucial aspect in the stellar mass assembly. Given that quenched galaxies in the local galaxies have an elliptical morphology, this problem of quenching is linked to one of the most important and long-standing questions of modern cosmology: why and when did the massive elliptical galaxies form and quench.

Based on deep multi-color surveys, we show that massive quiescent galaxies are assembled really efficiently at $1 < z < 3$. Most of the massive star-forming galaxies present at $z \sim 3$ should have quenched 1.5Gyr later ($z \sim 1$). Therefore, the redshift range $1 < z < 3$ is an interesting epoch to study the quenching processes occurring in massive galaxies. Above $z > 3$, the quiescent samples are questionable since the capacity to select the quiescent galaxies is degraded by the low quality of the photometric redshifts and the noise in the rest-frame colors (see Fig.5.1). No spectroscopic redshift of quiescent galaxies at $z > 3$ has yet been obtained (Kronager et al. 2014). We do not know when the first galaxies start to be quenched. Therefore, important progresses will be done when we will be able to confirm the redshifts and the quiescence nature of the $z > 3$ quiescent candidates. With a mirror of 6.5m and cameras and spectrographs operating at NIR wavelengths, the JWST observatory will be ideal to follow the massive and quiescent candidates at $z > 3$. Massive quiescent galaxies with $K \sim 24-25$ are reachable with the NIRSpec spectrograph. JWST should be available in 2019 and it will be possible to obtain such spectroscopic redshifts with the NIRSpec spectrograph and images with the NIRCam camera. In an even longer term, the E-ELT will also be able to reach such sources. Still, we will need to find the quiescent candidates which are rare at $z > 3$. The future cosmological multi-color surveys described in the next section (e.g. EUCLID, LSST) will cover unprecedent volumes and should be ideal to provide large samples of candidates.

When we study the processes responsible for the quenching, a crucial aspect to be considered is that the massive quiescent galaxies have also an elliptical morphology in the local Universe. We showed that it is the case at least at $z < 0.8$. Therefore, we must understand and explain why these two properties are linked. Numerous theoretical studies have isolated the physical processes relevant in the differentiation of the elliptical population from the other galaxies and quantify their importance along cosmic time. A first possibility is that a single process induces both quenching and morphological transformation, which could be major merging according to Hopkins et al. (2006). While extremely appealing, such a scenario does not provide a mechanism to prevent new cold gas from accreting on the central galaxy in massive halos, which could rejuvenate its star formation later. In DM halos above a critical mass of $10^{12}\mathcal{M}_{\odot}$, the gas could be maintained hot with the energy released by a radio-AGN over the Hubble time (e.g. Croton et al. 2006, Gabor & Davé 2015). Therefore, galaxies in these massive halos cannot form new stellar populations and quench. We compared the observed density of quiescent galaxies and the one predicted by a cosmological model based on this prescription (Wang et al. 2008). The mismatch between the observed and predicted density is dramatic at all masses in Wang et al. (2008) and still quite discrepant in the most recent SAM (Hendriques et al. 2015). Despite the profuse observations and physical processes that we have in hand, the theory is not able to fully describe the processes at work in the formation of massive and red elliptical galaxies. Since mergers are expected to play a crucial role in the formation of this population, a possible interesting analysis would be to compare the fraction of galaxy pairs within the simulation with the observed one, by applying exactly the same

selection criteria to both. By allowing the identification of radio-AGN, SKA will also provide extremely useful constraint on the impact of the radio mode.

An analysis that could point us out toward the relevant processes is to establish what is coming first, quenching or morphological transformation. In Ilbert et al. (2010), we found massive quiescent galaxies which are not elliptical, i.e. galaxies which have already quenched without experiencing a morphological transformation. Their fraction appears to increase at $z > 0.8$, but our classification was not sufficiently well constrained to be explored at $z > 1$ in the most interesting redshift range. Using a reference sample over 0.05 deg^2 with deep NIR HST/WFC3 images (CANDELS, Grogin et al. 2011), we could assess the redshift/mass range in which an automatic ACS classification could be trusted. In the next decade, we will gather incredibly large samples of massive galaxies at $1 < z < 2$, combining space quality data and spectra over tens of square degrees. After 2020, The Euclid mission will produce space quality images over 15000 deg^2. With a telescope of 1.2m and an excellent image resolution in visible, Euclid should allow us to isolate the galaxies by morphological type, a crucial aspect of its legacy science. Such a morphological information will be cross-matched with the NIR spectra of the next generation of MOS spectrographs operating in the NIR (e.g. MOONS, 4MOST at ESO). In particular, the Prime Focus Spectrograph (PFS) at Subaru will be commissioned on Subaru in 2018 and the survey will be running in 2019. This spectrograph operates in three channels from 0.4 to 1.3μm and 2400 fibers are placed simultaneously over galaxies. The PFS galaxy evolution survey has the objective to reconstruct the galaxy environment at $1 < z < 3$ using 800,000 spectroscopic redshifts over 25 deg^2. The goal is to acquire a survey like SDSS, but at $z \sim 1.5$. This survey should be able to detect the continuum for the massive quiescent galaxies $z < 2$. Therefore, we should be able to assess in detail how fast the red elliptical galaxies are assembled, how long elliptical galaxies can stay star-forming without being quenched, and how many galaxies are quenched without being transformed into an elliptical. And we will be able to produce such an analysis as a function of the cosmic web. These measurements are fundamental to understand the processes responsible of the differentiation of the red elliptical population over time.

6.3 Photometric redshifts for precision cosmology

In this manuscript, we used the photometric redshifts to study the galaxy evolution with a 2 deg^2 survey. However, the photometric redshifts are becoming a major tool to study the dark energy. In the next decade, numerous surveys are planned to perform weak lensing analysis and they all rely on massive photometric redshift surveys over thousands of square degrees. We describe here the bright future that we expect for the photometric redshifts in these massive survey era. While this section is not directly related to the main scientific driver in this manuscript (and could be almost considered as an annex), all these surveys will be also a treasure to study galaxy formation and evolution because of the volume covered.

6.3.1 Photometric redshifts for weak lensing tomography

The nature of the dark energy is one of the biggest mystery of modern physic. The dark energy is often presented as vacuum energy which would behave as the Einstein cosmological constant. In the so called "concordance ΛCDM" model, the dark energy is effectively considered as a constant over space and time. However, theory expects the vacuum energy to produce an energy 120 order of magnitude larger than the one we observe. This difference is often presented as the largest discrepancy between theory and observations. Some alternative theories to the cosmological constant exist. The most famous one is a form of matter called quintessence, which would evolve with time, by contrast with the cosmological constant. Therefore, one of the main goal of current cosmological experiments is to constrain the nature of the dark energy by measuring the evolution with time of the dark energy equation of state $w = P_{DE}/\rho_{DE}$, with P_{DE} the pressure and ρ_{DE} the energy density associated to the dark energy. For a cosmological constant, we would find $w = -1$. Other models like "quintessence" predict an evolution of w which is parametrized for simplicity as $w = w_0 + w_a(1 - a)$ with a the scale factor of the Universe. Therefore, dark energy experiments aim to constrain w_0 and w_a with a sufficient precision to detect any deviation of w_a from a null value. Alternatively, the acceleration of the Universe may even signified the breakdown of Einstein's Theory of General Relativity which could be tested by measuring the structure growth over large scales (e.g. Guzzo et al. 2008, de La Torre et al. 2013).

In the last decade, weak lensing tomography has emerged has one powerful tool to study the dark energy equation of state, but this new technique could be badly degraded by systematic errors (Peacock et al. 2006, Albrecht et al. 2006). The evolution of the mass distribution probes the influence of dark energy on the growth of structures. Measuring the evolution of the mass power spectrum could potentially provide one of the strongest constrain on w_0 and w_a. The basic principle of the weak lensing method is that the mass present into a foreground structure will deflect the light of a population of background galaxies. Therefore, the shapes of these background galaxies will be deformed by the potential well of the foreground structures. By measuring the shape deformation of the background galaxies (the shear signal), we study the mass present on the line of sight. Since galaxies do not have round shape and since this shape modification is at the order of the percent, one need to average over large sample of galaxies (typical more than 10-30 gal/arcmin^2). In the lensing tomography approach (Hu, 1999), galaxies are split into several redshift bins. The shape measurements are cross-correlated between two redshift bins. The shear signal extracted from these cross-correlations indicates how the mass power spectrum evolves. Therefore, weak lensing tomography probe the expansion history of the universe which is a valuable probe of dark energy. The advantage of weak lensing over other probes is that it directly probes the mass distribution, which is dominated by dark matter and we do not need to understand how galaxy traces the dark matter (the bias).

An observational challenge for weak lensing tomography is to derive photometric redshifts for hundred millions of sources. Indeed, weak lensing tomography requires a large

number of sources to average the shear signal. Since the galaxy are split by redshift bins, the method required to have their distances. In order to reach the required surface density of sources, survey depth of $I_{AB} < 24.5$ are typically required. Such samples have a median redshift above $z \sim 0.8$ (Le Fèvre et al. 2013, Ilbert et al. 2009). Since we want the weak lensing power spectrum, we also need to survey large scales, which means a considerable number of faint sources (future surveys could contain a billion of sources). It becomes impractical to obtain spectroscopic redshifts for more than few percents of these faint sources, even using future instrumentation like PFS. Therefore, photometric redshifts are the only alternative.

6.3.2 Future wide field imaging surveys

Numerous Dark Energy projects aim to put constrains on the nature of the dark energy using weak lensing tomography. Indeed, catalogues containing hundred millions of galaxies will be collected within the next 5 years, and billions of galaxies in the next 15 years. With such samples, photometric redshifts become a central tool in cosmology.

2013-2018: The Dark Energy Survey (DES)
The Dark Energy Survey (DES) started in August 2013 and use the DECam camera on the Blanco 4m telescope at CTIO. The DECam camera has a 2.2 deg^2 field-of-view which will allow to cover 5000 deg^2 of the Southern sky in 5 years. Observations will be carry on in 5 bands g, r, i, z and Y and should reach the 10σ magnitudes limits for a galaxy of 25.2, 24.8, 24, 23.4 and 21.7, respectively. Their goal is to observe 300 million galaxies (200 million suitable for weak lensing). DES combines four probes of the dark energy (supernovae, galaxy cluster, weak lensing and Baryonic Acoustic Oscillations). They should obtain an effective background density of 10 galaxies/arcmin^2 for weak lensing analysis. They will use photometric redshifts with an expected precision of $0.05(1+z)$ to split their sample in several tomographic bins, but also to compute large scale clustering of galaxies in bins of photometric redshift to enable Baryon acoustic oscillations (BAO) measurements.

2014-2024: The SuMIRe project
The Hyper Suprime-Cam (HSC) camera is installed on the Subaru telescope (Hawaii). This camera has a field-of-view of 1.7deg^2. The HSC survey started in 2014. The goal is to cover 1500 deg^2 in *grizy* filter with a magnitude limit of 26 in i and 24 in y (5 σ for a point like source). This imaging will be complemented with spectroscopy using the Prime Focus Spectrograph (PFS) instrument. The PFS multi-object spectrograph will have a multiplex of 2400 in a 1.3 deg^2 field-of-view. The spectra will cover a wavelength range from 3800Å to 13000Å. PFS targets will be selected with the HSC images. The union of the HSC and PFS surveys corresponds to the Subaru Measurement of Images and Redshifts (SuMIRe) project.

2016-2020: The J-PAS survey
This survey will be carry on with the new 2.5m Jalambra Telescope. The specific advantage of this survey is to cover 8500 deg^2 with 54 narrow band filters. They should observe 300 millions of galaxies with a photo-z precision of 0.3%. One of the main objectives of this survey is the measure the BAO.

2016-2020: The PAU survey
The Physics of the Accelerating Universe survey (PAU) will be conducted on the 4.2m William Herschel Telescope. They plan to obtain 100 nights over 4 years to survey 100 deg^2 in 40 narrow-band and 6 broad-band filters. They plan to observe several millions of galaxies with a photo-z precision of 0.35% (Martí et al. 2014). With such an accuracy, they want to study the redshift space distortion and the weak lensing magnification, with the objective of constraining the nature of the dark energy.

2020-2025: The EUCLID mission
Euclid is European Space Agency (ESA) Medium Class mission with a launch scheduled in 2020. The mission duration should be of 6 years. The telescope has a 1.2m mirror and VIS and NISP are the two main instruments.

The VIS camera of Euclid will be dedicated to imaging. This optical camera will contain only one broad band filter (called *RIZ*) covering the wavelength range 550-900 nm. With its large field-of-view ($0.5 deg^2$), the goal of this camera is to provide exquisite images in order to measure the galaxy shapes of 1.5 billion of galaxies. Since this camera is operating from space, no competing project will be able to provide a such quality of images for weak lensing in this same timescale. This step is crucial to reduce systematics in weak lensing tomography. The survey is designed to cover 15000 deg^2 and to gather more than > 30 galaxies per arcmin^2 with a median redshift of $z \sim 0.9$ and a magnitude limit at $m(RIZ) < 24.5$.

The NISP instrument is dedicated to the measure of the galaxy distances:

- using NIR spectroscopy (11000Å-20000Å). We will use slitless grism to detect the H_α emission for more than 50 millions of galaxies at $0.7 < z < 2$. The spectroscopic survey is designed to measure galaxy clustering and in particular to extract the BAO and Redshift-space distortions (RSD) signals.

- using NIR imaging in three filters Y, J and H. These filters will cover the full wavelength (9200Å-20000Å) without any gap, which is not possible from the ground. The goal of these filters is to insure precise photometric redshifts at $z > 1.3$ which is not possible without NIR.

Photometric redshifts are necessary for the weak lensing tomography. However, Euclid alone can not provide accurate photometric redshifts. Indeed, we need a good optical coverage to obtain precise photometric redshifts at $z < 1.3$. Therefore, the optical colors need to be taken using ground-based observations. The Euclid photometry needs to be complemented with at least g, r, i, z band data with an estimated depth at 24.4, 24.1, 24.1

and 23.7 (10 σ limit for an extended sources). Such a sensitivity is currently reached by surveys covering hundred of deg^2 (e.g. CFHTLS Wide). Current instruments should be able to cover the thousands of deg^2 required for Euclid in several hundred of nights, like the Pan-STARRS camera, the Dark Energy Camera (DECam) or the Hyper-SuprimeCamera on the Subaru telescope. The requirements on the fidelity of photometric redshifts are the following:

- *precision* $\sigma_{z/(1+z)} < 0.05$;
- *catastrophic failures* $\eta < 10\%$;
- *Knowledge of the mean redshift* $\sigma(< z >) < 0.002(1 + z)$;

While the two first requirements are routinely satisfied with surveys having a similar depth than Euclid, the most challenging problem is to determine the mean redshift with a precision better than $0.002(1 + z)$. However, the characterization of the redshift distribution moments (average and sigma) could be possible using a large calibration sample of 100000 spec-z or alternative methods of cross-correlation (e.g. Newman et al. 2013).

2021-2031: The Large Synoptic Survey Telescope (LSST)
In the next decade, the Large Synoptic Survey Telescope (LSST) will start to cover 18000 deg^2 of the sky. This telescope of 8.4m will operate in Chile. The camera field-of-view will reach 9.6 deg^2 (effective 8.5 deg^2). The survey will operate for 10 years. The images will be obtained in 6 bands *ugrizy* from 3200 to 10500Å. In total, the survey will gather 10 billions of galaxies and 10 billions of stars with a survey reaching $r_{AB} = 27.5$ (5σ, point-like sources). Each location of the sky will be visited about 1000 times over 10 years, which means that LSST will be extremely powerful to extract variable sources, but also to insure a stable photometry. One requirement of the survey is to get band-to-band calibration errors not larger than 0.005 mag and no more than 0.01 mag variation across the sky. Four billion sources (40 galaxies/arcmin^2) should be suitable for weak lensing analysis. LSST should deliver photo-z with a precision between 1-2% and a median redshift of $z \sim 1.2$ for the weak lensing sample selected at $r_{AB} = 25.3$. The requirements on the fidelity of photometric redshifts are similar to the one expected for EUCLID (a precision of $\sigma_{z/(1+z)} < 0.05$, catastrophic failures below $\eta < 10\%$ and the bias must be known at $\sigma(< z >) < 0.003(1 + z)$. With such an amount of data, tomographic measurements of weak lensing will provide percent-level constraints on cosmological parameters.

2023-2029: WFIRST-AFTA
The recent version of this satellite use a 2.4m telescope offered to NASA after the discontinuation of the national security program. This mission would use a 0.3 deg^2 camera and measure the weak lensing signal in NIR for 500 million galaxies. This satellite has a supernovae component which is not present in the Euclid mission using an IFU.

This mission will cover 2000 deg^2.

As a conclusion, the need for photo-z will explode in the next decade with all these future surveys and missions. We will face incredible challenge in term of maintaining an homogeneous quality of the data over such a wide area, the quality control and the methods themselves. New directions are investigated using the large scale structures traced with spec-z as an additional information (Menard et al. 2014). They could revolutionize this research field. A crucial step will be to develop the right synergy between these photo-z surveys and the required spec-z follow-ups. Given the scale of such surveys, such spectroscopic follow-up needs to be started years in advance. Since these surveys are designed to study dark energy, some requirements for galaxy evolution studies will not enter in the survey planning (e.g. the need for completeness). Therefore, we will need to handle with extreme care those enormous datasets. Still, these surveys with billions of galaxies will be an enormous source of information to study galaxy formation and evolution in the next decade.

Bibliography

Abraham R. G., Tanvir N. R., Santiago B. X., Ellis R. S., Glazebrook K. & van den Bergh S., 1996, MNRAS, 279, L47

Abraham et al. 2007, ApJ, 669, 184

Albrecht A., Bernstein G., Cahn R. et al., 2006, astro-ph/0609591

Arnouts S. et al., 1999, MNRAS, 310, 540

Arnouts S., Moscardini L., Vanzella E. et al., 2002, MNRAS, 329, 355

Arnouts S., Walcher C.J., Le Fèvre O. et al., 2007, A&A, 476, 137

Arnouts S., Le Floc'h E., Chevallard J. et al., 2013, A&A, 558, A67

Babbedge T.S.R., Rowan-Robinson M., Gonzalez-Solares E. et al. 2004, MNRAS, 353, 654

Baldry I.K., Driver S.P., Loveday J. et al., 2012, MNRAS, 421, 621

Barnes,1992, ApJ, 393

Barro G., Perez-Gonzalez P.G., Gallego J. et al., 2011, ApJS, 193, 30

Baum, W.A. 1962, Problems of Extra-Galactic Research, 15, 390

Bell E. F., McIntosh D. H., Katz N., & Weinberg M. D., 2003, ApJS, 149, 289

Bell E.F., Wolf C., Meisenheimer K. et al., 2004, ApJ, 608, 752

Behroozi P.S., Wechsler R.H. & Conroy C., 2013, ApJ, 770, 57

Benítez N., 2000, ApJ, 536, 571

Benítez N., Ford H., Bouwens R. et al. 2004, ApJS, 150, 1

Bertin E. & Arnouts S., 1996, A&AS, 117, 393

Béthermin M., Le Floc'h E., Ilbert O. et al., 2012, A&A, 542, A58

Bezanson R., van Dokkum P. & Franx M., 2012, ApJ, 760, 62

Bielby R., Hudelot P., McCracken, H.J. et al., 2012, A&A, 545, A23

Boissier S., Buat V., Ilbert O., 2010, A&A, 522, A18

Bolzonella M., Miralles J.-M., Pelló R., 2000, A&A, 363, 476

Bordoloi R., Lilly S.J. & Amara A., 2010, MNRAS, 406, 881

Boulade O., et al., 2000, proc. SPIE, 4008, 657

Bouché N., Dekel A., Genzel R. et al., 2010, ApJ, 718, 1001

Bournaud F., Elmegreen B.G., Elmegreen D.M., 2007, ApJ, 670, 237

Bournaud F., Chapon D., Teyssier R. et al., 2011, ApJ, 730, 4

Bouwens R.J., Illingworth G.D., Oesch P.A. et al., 2012, ApJ, 754, 83

Bower R.G., Benson A.J., Malbon R. et al., 2006, MNRAS, 370, 645

Bower R.G., Benson A.J. & Crain A., 2012, MNRAS, 422, 2816

Brammer G.B., van Dokkum P.G. & Coppi P., 2008, ApJ, 686, 1503

Brammer G.B., Whitaker K.E., van Dokkum P.G. et al., 2009, ApJL, 706, L173

Brammer G.B., Whitaker K.E., van Dokkum P.G. et al., 2011, ApJ, 739, 24

Brodwin M., Lilly S.J., Porciani C. et al., 2006, ApJ, 162, 20

Bromm V. & Yoshida N., 2011, ARA&A, 49, 373

Brusa M., Zamorani G., Comastri A. et al., 2007, ApJS, 172, 353

Bruzual G. & Charlot S., 2003, MNRAS, 344, 1000

Bruzual A.G., 2007, arXiv:0702091v1

Buat V., Giovannoli E., Heinis S. et al., 2011, A&A, 533, AA93

Budavári T., Szalay A. S., Connolly A. J., Csabai I. & Dickinson M., 2000, AJ, 120, 1588

Bundy et al., 2010, ApJ, 719, 1969

Calzetti D., Armus L., Bohlin R.C. et al., 2000, ApJ, 533, 682

Capak P., Cowie L.L., Hu E.M. et al., 2004, AJ, 127, 180

Capak, P., Aussel, H., Ajiki, M. et al. 2007, ApJS, 172 , 99

Capak P., Abraham R.G., Ellis R.S. et al., 2007, ApJS, 172, 284

Capak P.L., Riechers D., Scoville N.Z. et al., 2011, Nature, 470, 233

Caputi K.I., Lagache G., Yan L. et al., 2007, ApJ, 660, 97

Caputi K.I., Cirasuolo M., Dunlop J.S. et al., 2011, MNRAS, 413, 162

Cardamone C. N., van Dokkum P. G., Urry C. M. et al., 2010, ApJS, 189, 270

Carliles, S., Budavári, T., Heinis, S., Priebe, C., & Szalay, A. S. 2010, ApJ, 712, 511

Cattaneo et al., 2006, MNRAS, 370, 1651

Cattaneo et al., 2013, MNRAS, 430, 686

Chabrier G., 2003, PASP, 115, 763

Charlot S. & Fall S.M., 2000, ApJ, 539, 718

Chary R. & Elbaz D., 2001, ApJ, 556, 562

Cirasuolo M., McLure R.J., Dunlop J.S. et al., 2007, MNRAS, 380, 585

Coleman G. D., Wu C.-C. & Weedman D. W., 1980, ApJS, 43, 393

Collister A. A. & Lahav O., 2004, PASP, 116, 345

Comparat J., Richard J., Kneib J.P. et al., 2015, A&A, 575, AA40

Connolly A.J., Csabai I., Szalay A.S., Koo D.C., Kron R.G. & Munn J.A. 1995, AJ, 110, 2655

Conroy C., Gunn J. E. & White M., 2009, ApJ, 699, 486

Conroy C. & Wechsler R. H., 2009, ApJ, 696, 620

Conroy C., 2013, ARAA, 51, 393

Contini T., Garilli B., Le Fèvre O. et al., 2012, A&A, 539, A91

Conselice et al., 2000, AJ, 126, 1183

Coupon J., Ilbert O., Kilbinger M., et al., 2009, A&A, 500, 981

Coupon J., Kilbinger M., McCracken H.J. et al., 2012, A&A, 542, A5

Coupon J., Arnouts S., van Waerbeke L. et al., 2015, MNRAS,449,1352

Cowie L.L., Songaila A., Hu E.M. & Cohen J.G., 1996, AJ, 112, 839

Cresci G., Mannucci F., Maiolino R. et al., 2010, Nature, 467, 811

Cross, N.J.G. et al. 2004, AJ, 128, 1990

Croton D.J., Springel V., White S.D.M. et al., 2006, MNRAS, 365, 11

Cucciati O., Tresse L., Ilbert O. et al., 2012, A&A, 539, A31

Cucciati O., De Lucia G., Zucca E. et al., 2012b, A&A, 548, 108

Curtis H.D. 1917, PASP, 29, 206

Csabai I., Connolly A. J., Szalay A. S. & Budavári T., 2000, AJ, 119, 69

Daddi E. et al., 2000, A&A, 361, 535

Daddi, E., Cimatti, A., Renzini, A. et al. 2004, ApJL, 600, 127

Daddi E., Dickinson M., Morrison G. et al., 2007, ApJ, 670, 156

Dahlen T., Mobasher B., Faber S.M. et al., 2013, ApJ, 775, 93

Dale D.A. & Helou G. 2002, ApJ, 576, 159

Davidzon I., Bolzonella M., Coupon J. et al., 2013, A&A, 558, A23

Davis M., Faber S.M., Newman J. et al., 2003, SPIE, 4834, 161

Dayal P., Mesinger A., Pacucci F., 2015, ApJ, 806, 67

de Barros S., Schaerer D. & Stark D.P., 2014, A&A, 563, A81

Dekel A., Birnboim Y., Engel G. et al., 2009, Nature, 457, 451

de la Torre S., Guzzo L., Peacock J.A. et al., 2013, A&A, 557, AA54

De Lucia G., Springel V., White S.D.M., Croton D. & Kauffmann G., 2006, MNRAS, 366, 499

De Lucia G. & Blaizot J., 2007, MNRAS, 375, 2

de Ravel L., Le Fèvre O., Tresse L. et al., 2009, A&A, 498, 379

Domínguez A., Siana B., Brooks A.M. et al., 2014, astro-ph/1408.5788

Domínguez Sánchez H., Pozzi F., Gruppioni C. et al., 2011, MNRAS, 417, 900

Donley J.L., Koekemoer A. M., Brusa M. et al., 2012, ApJ, 748, 142

Drory N., Bundy K., Leauthaud A. et al., 2009, ApJ, 707, 1595

Dunne L., Ivison R.J., Maddox S. et al., 2009, MNRAS, 394, 3

Eddington A. S., 1913, MNRAS, 73, 359

Efstathiou G., Ellis R.S., Peterson B.A., 1988, MNRAS, 232, 431

Elbaz D., Daddi E., Le Borgne D. et al., 2007, A&A, 468, 33

Elbaz D., Hwang H.S., Magnelli B. et al., 2010, A&A, 518, L29

Elbaz D., Dickinson M., Hwang H.S. et al., 2011, A&A, 533, A119

Ellis R. S., Colless M., Broadhurst T., Heyl J., & Glazebrook K., 1996, MNRAS, 280, 235

Emerson et al., 2010, VISTA: status and performance (Proceedings of SPIE)

Emerson J.P. & Sutherland W.J., 2010, in Proc. SPIE (SPIE), 773306-773306-12

Erben T., Hildebrandt H., Miller L. et al., 2013, MNRAS, 433, 2545

Faber S.M., Willmer C.N.A., Wolf C. et al., 2007, ApJ, 665, 265

Feldmann, R., Carollo, C. M., Porciani, C. et al. 2006, MNRAS, 372, 565

Fernández-Soto A., Lanzetta K. M. & Yahil A., 1999, ApJ, 513, 34

Fioc M. & Rocca-Volmerange B., 1997, A&A, 326, 950

Firth, A. E., Lahav, O., & Somerville, R. S. 2003, MNRAS, 339, 1195

Fischera, J., Dopita, M. A., & Sutherland, R. S. 2003, ApJL, 599, L21

Fontana, A., D'Odorico, S., Poli, F. et al. 2000, AJ, 120, 2206

Fontana A., Pozzetti L., Donnarumma I. et al., 2004, A&A, 424, 23

Förster-Schreiber N.M., Genzel R., Newman S.F. et al., 2009, ApJ, 706, 1364

Förster-Schreiber N.M., Genzel R., Newman S.F. et al., 2014, ApJ, 787, 38

Franzetti P., Scodeggio M., Garilli B. et al., 2007, A&A, 465, 711

Fritz A., Scodeggio M., Ilbert O. et al., 2014, A&A, 563, A92

Furlong M., Bower R. G., Theuns T. et al., 2015, MNRAS, 450, 4486

Gabasch A. et al., 2004, A&A, 421, 41

Gabor J.M. & Davé R., 2015, MNRAS, 447, 374

Genzel R., Burkert A., Bouché, N. et al., 2008, ApJ, 687, 59

Genzel R., Förster Schreiber N.M., Lang P. et al., 2014, ApJ, 785, 75

Genzel R., Tacconi L.J., Lutz D. et al., 2015, ApJ, 800, 20

George M.R., Leauthaud A., Bundy K. et al., 2011, ApJ, 742, 125

Giallongo E., D'Odorico S., Fontana A., et al., 1998, ApJ, 115, 2169

Giavalisco M., Ferguson H.C., Koekemoer A.M. et al., 2004, ApJL, 600, L93

Grogin N.A., Kocevski D.D., Faber S.M. et al., 2011, ApJS, 197, 35

Gruppioni C., Pozzi F., Rodighiero, G. et al., 2013, MNRAS, 432, 23

Guo Q., White S., Boylan-Kolchin M. et al., 2011, MNRAS, 413, 101

Guo K., Zheng X.Z., & Fu H., 2013, ApJ, 778, 23

Guzzo L., Pierleoni M., Meneux B. et al., 2008, Nature, 451, 541

Guzzo et al., 2014, A&A, 566, 108

Hatton S., Devriendt J. E. G., Ninin S., Bouchet F. R., Guiderdoni B., & Vibert D. 2003, MNRAS, 343, 75

Heinis S., Milliard B., Arnouts S. et al., 2007, ApJS, 173, 503

Heinis S., Buat V., Béthermin M. et al., 2013, MNRAS, 429, 1113

Henriques B.M.B., White S.D.M., Thomas P.A. et al., 2015, MNRAS, 451, 2663

Heymans C., Van Waerbeke L., Miller L. et al., 2012, MNRAS, 427, 146

Hildebrandt H., Arnouts S., Capak P. et al., 2010, A&A, 523, AA31

Hildebrandt H., Erben T., Kuijken K. et al., 2012, MNRAS, 421, 2355

Hoaglin, D. C., Mosteller, F., & Tukey, J. W 1983, Understanding Robust and Exploratory Data Analysis. John Wiley & Sons, 404-414.

Hopkins A.M. & Beacom J.F., 2006, ApJ, 651, 142

Hopkins P.F., Hernquist L., Cox T.J., Di Matteo T., Robertson B. & Springel V., 2006, ApJS, 163, 1

Hopkins P.F., Hernquist L., Cox T.J., & Kereš D., 2008, ApJS, 175, 356

Hopkins P.F., Cox T.J., Younger J.D. & Hernquist L., 2009, ApJ, 691, 1168

Hopkins P.F., Keres D., Onorbe J. et al., 2014, MNRAS, 445, 581

Hubble 1929, PNAS, Volume 15, Issue 3, pp. 168-173

Ilbert O., Tresse L., Arnouts S. et al., 2004, MNRAS, 351, 541

Ilbert O., Tresse L., Zucca E. et al., 2005, A&A, 439, 863

Ilbert O., Arnouts S., McCracken H.J. et al., 2006, A&A, 457, 841

Ilbert O., Capak P., Salvato M. et al., 2009, ApJ, 690, 1236

Ilbert O., Salvato M., Le Floc'h E. et al., 2010, ApJ, 709, 644

Ilbert O., McCracken H., Le Fèvre O. et al., 2013, A&A, 556, 55

Ilbert O., Arnouts S., Le Floc'h E. et al., 2015, A&A, 579, A2

Im M., Faber S. M., Gebhardt K. et al., 2001, AJ, 122, 750

Ivezic, Z., Tyson, J. A., Acosta, E., et al. 2008, arXiv:0805.2366

Jarvis M., Seymour N., Afonso J. et al., 2015, Advancing Astrophysics with the Square Kilometre Array (AASKA14), 68

Jouvel S., Kneib J.-P., Ilbert O. et al., 2009, A&A, 504, 359

Jouvel S., Kneib J.-P., Bernstein G. et al., 2011, A&A, 532, AA25

Kajisawa M., Ichikawa T., Yamada T. et al., 2010, ApJ, 723, 129

Kajisawa M., Ichikawa T., Yoshikawa T. et al., 2011, PASJ, 63, 403

Karim A., Schinnerer E., Martínez-Sansigre A. et al., 2011, ApJ, 730, 61

Kartaltepe, J. S., Sanders, D. B., Le Floc'h, E., et al. 2010, ApJ, 721, 98

Kartaltepe et al. 2015, ApJ, submitted, 1401.2455

Kauffmann G., White S. D. M. & Guiderdoni B., 1993, MNRAS, 264, 201

Kauffmann G. & Haehnelt M., 2000, MNRAS, 311, 576

Kelson D.D., submitted to ApJ, astro-ph/1406.5191

Kennicutt R.C., 1998, ARA&A, 36, 189

Kinney A. L., Calzetti D., Bohlin R. C., McQuade K., Storchi-Bergmann T. & Schmitt H. R., 1996, ApJ, 467, 38

Koekemoer et al. 2007, ApJS 172, 196

Krogager et al., 2014, ApJ, 797, 17

Laidler V. G., Papovich C., Grogin N. A. et al. 2007, PASP, 119, 1325

Lagache G., Dole H., Puget J.-L. et al., 2004, ApJS, 154, 112

Lamareille F., Brinchmann J., Contini, T. et al., 2009, A&A, 495, 53

Lauger S., Burgarella D. & Buat V., 2005, A&A, 434, 77

Lawrence et al., 2007, MNRAS, 379, 1599

Lee N., et al., 2015, ApJ, 801, 80

Le Fèvre O., Vettolani G., Paltani S. et al., 2004, A&A, 428, 1043

Le Fèvre, O., Vettolani, G., Garilli, B. et al. 2005, A&A, 439, 845

Le Fèvre O., Cassata P., Cucciati O. et al., 2013, a&A, 559, AA14

Le Fèvre O., Amorin R., Bardelli S. et al., 2014, The Messenger, 155, 38

Le Fèvre O., Tasca L.A.M., Cassata P. et al., 2015, A&A, astro-h/1403.3938

Le Floc'h E., Papovich C., Dole H. et al., 2005, ApJ, 632, 169

Le Floc'h E., Aussel H., Ilbert O. et al., 2009, ApJ, 703, 222

Lehnert M.D. & Heckman T.M., 1996, ApJ, 462, 651

Lilly S. J., Le Fevre O., Hammer F. & Crampton D., 1996, ApJL, 460, L1

Lilly S.J., Le Fèvre O., Renzini A. et al., 2007, ApJS, 172, 70

Lilly S.J., Le Brun V., Maier C. et al., 2009, ApJS, 184, 218

Lilly S.J., Carollo C.M., Pipino A., Renzini A. & Peng Y., 2013, ApJ, 772, 119

Lonsdale C.J., Smith H.E., Rowan-Robinson M. et al., 2003, PASP, 115, 897

López-Sanjuan C., Le Fèvre O., Ilbert O. et al., 2012,A&A, 548, A7

López-Sanjuan C., Le Fèvre O., Tasca L.A.M. et al., 2013, A&A, 553, A78

López-Sanjuan C., Cenarro, A.J., Varela J., et al., 2015, A&A, 576, A53

Lotz et al. 2008, ApJ, 672, 177

Lu Y., Mo H.J., Weinberg M.D. & Katz N., 2011, MNRAS, 416, 1949

Lu Y., Mo H.J., Lu Z., Katz N. & Weinberg M.D., 2014, MNRAS, 443, 1252

Lutz D., Poglitsch A., Altieri B. et al., 2011, A&A, 532, A90

Lynden-Bell D., 1971, MNRAS, 155, 95

Madau P., 1995, ApJ, 441, 18

Madau, P., Ferguson, H. C., Dickinson, M. E. et al. 1996, MNRAS, 283, 1388

Maddox S. J., Efstathiou G., Sutherland W. J. & Loveday J., 1990, MNRAS, 243, 692

Magdis G.E., Daddi E., Béthermin M. et al., 2012, ApJ, 760, 6

Magnelli B., Elbaz D., Chary R.R. et al. 2009, A&A, 496, 57

Magnelli B., Elbaz D., Chary R.R. et al. 2011, A&A, 528, A35

Magnelli B., Popesso P., Berta S. et al. 2013, A&A, 553, A132

Magorrian J., Tremaine S., Richstone D. et al., 1998, ApJ, 115, 2285

Maraston C., 2005, MNRAS, 362, 799

Maraston C., Daddi E., Renzini A. et al., 2006, ApJ, 652, 85

Maraston C., Pforr J., Renzini A. et al., 2010, MNRAS, 407, 830

Marchesini D., van Dokkum P.G., Förster Schreiber N. M., et al., 2009, ApJ, 701, 1765

Martí P., Miquel R., Castander F. J. et al., 2014, MNRAS, 442, 92

Marchesini D., van Dokkum P.G., Förster Schreiber N.M. et al., 2009, ApJ, 701, 1765

Martig M., Bournaud F., Teyssier R. & Dekel A., 2009, ApJ, 707, 250

Martin D.C., Wyder T.K., Schiminovich D. et al., 2007, ApJS, 173, 342

Martin C.L., Shapley A.E., Coil A.L. et al., 2012, ApJ, 760, 127

Massey R., Rhodes J., Leauthaud A. et al., 2007, ApJS, 172, 239

Mauduit J.-C., Lacy M., Farrah D. et al., 2012, PASP, 124, 714

Mazure, A., Adami, C., Pierre, M., et al., 2007, A&A, 467, 49

McCall, M. L., Rybski, P. M., & Shields, G. A. 1985, ApJS, 57, 1

McCracken H.J., Ilbert O., Mellier Y. et al., 2008, A&A, 479, 321

McCracken H.J., Capak P., Salvato M., et al., 2010, ApJ, 708, 202

McCracken H.J., Milvang-Jensen B., Dunlop J., et al., 2012, A&A, 544, A156

McCracken H.J., Wolk M., Colombi S., et al., 2015, MNRAS, 449, 901

Menanteau F., Ford H.C., Motta V. et al., 2006, ApJ, 131, 215

Ménard B., Scranton R., Schmidt S., et al., 2013, submitted, astroph/1303.4722

Meurer G.R., Heckman T.M. & Calzetti D., 1999, ApJ, 521, 64

Mignoli M., Cimatti A., Zamorani G. et al., 2005, A&A, 437, 883

Mitchell P.D., Lacey C.G., Baugh C.M., & Cole S., 2013, MNRAS, 435, 87

Mobasher, B., Capak, P., Scoville, N. Z. et al. 2007, ApJS, 172, 117

Moresco et al., 2012, JCAP, 8, 006

Mortlock A., Conselice C.J., Bluck A.F.L. et al., 2011, MNRAS, 413, 2845

Moster B.P., Somerville R.S., Newman J.A., and Rix H., 2011, ApJ, 731, 113

Mouhcine, M., Lewis, I., Jones, B., Lamareille, F., Maddox, S. J. & Contini, T. 2005, MNRAS, 362, 1143

Moustakas, J., Kennicutt, R. C. & Tremonti, C. A. 2006, ApJ, 642, 775

Moustakas J., Coil A., Aird J. et al., 2013, ApJ, 767, 50

Moutard T., Arnouts S., Ilbert O. et al., 2015, A&A, submitted

Muzzin A., Marchesini D., Stefanon M. et al., 2013a, ApJS, 206, 8

Neistein E., & Dekel A., 2008, MNRAS, 388, 1792

Newman J. A., 2008, ApJ, 684, 88

Newman, J. A., Cooper, M. C., Davis, M., et al., 2013, ApJS, 208, 5

Noeske K.G., Weiner B.J., Faber S.M. et al., 2007a, ApJL, 660, L43

Noeske K.G., Faber S.M., Weiner B.J. et al., 2007b, ApJL, 660, L47

Noll, S., Pierini, D., Pannella, M. & Savaglio, S. 2007, A&A, 472, 455

Oke J.B., 1974, ApJS, 27, 21

Oliver S.J., Bock J., Altieri B. et al., 2012, MNRAS, 424, 1614

Onodera M., Renzini A., Carollo M. et al., 2012, ApJ, 755, 26

Pacifici C., da Cunha E., Charlot S., et al., 2015, MNRAS, 447, 786

Pannella M., Carilli C.L., Daddi E. et al., 2009, ApJL, 698, L116

Peacock, J. A., Schneider, P., Efstathiou, G. et al. 2006, ESA-ESO Working Group on "Fundamental Cosmology", arXiv:astro-ph/0610906

Peng Y.J., Lilly S.J., Kovač K. et al., 2010, ApJ, 721, 193

Peng Y.-j., Lilly S. J., Renzini A. & Carollo M., 2012, ApJ, 757, 4

Peng Y.J., Lilly S.J., Renzini A., Carollo M., 2014, ApJ, 790, 95

Pérez-González P.G., Rieke G.H., Villar V. et al., 2008, ApJ, 675, 234

Perlmutter S., Aldering G., Goldhaber G. et al., 1999, ApJ, 517, 565

Planck collaboration, 2015, submitted to A&A, astro/ph:1502.01582

Polletta M., Tajer M., Maraschi L. et al., 2007, ApJ, 663, 81

Pozzetti L., Bolzonella M., Lamareille F. et al., 2007, A&A, 474, 443

Pozzetti L., Bolzonella M., Zucca E. et al., 2010, A&A, 523, 13

Press W. H. & Schechter P., 1974, ApJ, 187, 425

Prevot M. L., Lequeux J., Prevot L., Maurice E. & Rocca-Volmerange B., 1984, A&A, 132, 389

Puschell J.J., Owen F.N., & Laing R.A., 1982, ApJL, 257, L57

Rieke G.H., Alonso-Herrero A., Weiner B.J. et al., 2009, ApJ, 692, 556

Regnault N., Conley A., Guy J., et al., 2009, A&A, 506, 999

Renzini A. & Buzzoni A., 1986, Spectral Evolution of Galaxies, 122, 195

Riess A.G., Filippenko A.V., Challis P. et al., 1998, AJ, 116, 1009

Riguccini L., Le Floc'h E., Ilbert O. et al., 2011, A&A, 534, AA81

Robertson B.E., & Ellis R.S., 2012, ApJ, 744, 95

Robitaille T.P. & Whitney B.A., 2010, ApJL, 710, L11

Rodighiero G., Vaccari M., Franceschini A. et al., 2010, A&A, 515, A8

Rodighiero G., Daddi E., Baronchelli I. et al., 2011, ApJL, 739, L40

Rodighiero G., Renzini A., Daddi E. et al., 2014, MNRAS, 443, 19

Saintonge A., Tacconi L.J., Fabello S. et al., 2012, ApJ, 758, 73

Salim S., Rich R.M., Charlot S. et al., 2007, ApJS, 173, 267

Salim S., & Lee J.C., 2012, ApJ, 758, 134

Salpeter E.E., 1955, ApJ, 121, 61

Salvato et al. 2009, ApJ, 690, 1250

Salvato et al. 2011, ApJ, 742, 61

Sánchez C., Carrasco Kind M., Lin H. et al., 2014, MNRAS, 445, 1482

Sandage A., Tammann G.A., Yahil A., 1979, ApJ, 232, 352

Sanders et al., 1988, ApJ, 325, 74

Sanders et al. 2007, ApJS, 172, 86

Santini P., Fontana A., Grazian A. et al., 2012, A&A, 538, A33

Sargent M.T., Béthermin M., Daddi E. & Elbaz D., 2012, ApJL, 747, L31

Saunders W., Rowan-Robinson M., Lawrence A. et al., 1990, MNRAS, 242, 318

Scarlata et al. 2007, ApJS, 172, 406

Schaerer D. & de Barros S., 2012, IAU Symposium, 284, 20

Schechter P., 1976, ApJ, 203, 297

Schiminovich D., Ilbert O., Arnouts S. et al., 2005, ApJL, 619, L47

Schlegel D. J., Finkbeiner D. P. & Davis M., 1998, ApJ, 500, 525

Schlegel, Abdallaz, Ahn et al. 2011, astro-ph/1106.1706S

Scoville N., Aussel H., Brusa M. et al. 2007, ApJS, 172, 1

Scoville N.Z., 2012, ArXiv:1210.6990

Scoville N., Arnouts S., Aussel H. et al. 2013, ApJS, 172, 1

Sheth K., Elmegreen D.M., Elmegreen M. et al., 2008, ApJ, 675, 1141

Silva, L., Granato, G. L., Bressan, A. et al. 1998, ApJ, 509, 103

Silverman et al., 2015, ApJ, arXiv:1409.0447

Slipher 1913, Popular Astronomy, Vol. 21, p.186

Smolčić V., Schinnerer E., Scodeggio M. et al., 2008, ApJS, 177, 14

Somerville et al. 2008, MNRAS, 391, 481

Speagle J.S., Steinhardt C., Capak P., Silverman J.D., 2014, ApJS, 214, 15

Springel V., Frenk C.S., & White S.D.M.m 2006, Nature, 440, 1137

Stark D., Schenker M.A., Ellis R. et al., 2013, ApJ, 763, 129

Steidel C. C., Giavalisco M., Pettini M., Dickinson M. & Adelberger K. L., 1996, ApJL, 462, L17

Szalay A. S., Connolly A. J. & Szokoly G. P., 1999, AJ, 117, 68

Tacconi et al., 2010, Nature, 463, 781

Tanaka M., 2015, ApJ, 801, 20

Taniguchi et al., 2015, PASP, submitted

Tasca L.A.M., Le Fèvre O., López-Sanjuan C., et al., 2014, A&A, 565, AA10

Tasca L.A.M., Le Fèvre O., Hathi N.P. et al., 2015, A&A, 581, A54

Tomczak A.R., Quadri R.F., Tran K.-V.H. et al., 2014, ApJ, 783, 85

Toomre A., 1974, IAU Symposium, The Formation and Dynamics of Galaxies

Torrey P., Vogelsberger M., Genel S. et al., 2014, MNRAS, 438, 1985

Toft S., Smolčić V., Magnelli B. et al., 2014, ApJ, 782, 68

Tresse L., Maddox S.J., Le Fèvre O., & Cuby J.-G., 2002, MNRAS, 337, 369

van Dokkum P.G., Leja J., Nelson E.J. et al., 2013, ApJL, 771, L35

Wadadekar Y., 2005, PASP, 117, 79

Walcher J., Groves B., Budavari T., Dale D., 2011, ApSS, 331,1

Wang J., De Lucia G., Kitzbichler M.G. and White S.D.M., 2008, MNRAS, 384, 1301

Weinmann S.M., Neistein E. & Dekel A., 2011, MNRAS, 417, 2737

Weinmann S.M., Pasquali A., Oppenheimer B.D. et al., 2012, MNRAS, 426, 2797

Welker C., Dubois Y., Devriendt J. et al., 2015, arXiv:1502.05053

Whitaker K.E., Labbé I., van Dokkum P.G., et al., 2011, ApJ, 735, 86

Whitaker K.E., van Dokkum P.G., Brammer G. & Franx M., 2012, ApJL, 754, L29

Whitaker K.E., Franx M., Leja J. et al., 2014, 795, 104

White S. D. M. & Rees M. J., 1978, MNRAS, 183, 341

Williams R.J., Quadri R.F., Franx M. et al., 2009, ApJ, 691, 1879

Wilkins S.M., Trentham N. & Hopkins A.M., 2008, MNRAS, 385, 687

Wolf C., Meisenheimer K., Rix H.-W., Borch A., Dye S., & Kleinheinrich M. 2003, A&A, 401, 73

Wuyts S., Labbé I., Schreiber N. M. F. et al., 2008, ApJ, 682, 985

Wolk M., McCracken H.J., Colombi S. et al., 2013, MNRAS, 435, 2

Zamojski M.A., Schiminovich D., Rich R.M. et al., 2007, ApJS, 172, 468

Zucca, E., Ilbert, O., Bardelli, S. et al. 2006, A&A, 455, 879